Feasibility Study for a Spacecraft Navigation System relying on Pulsar Timing Information

Final Report

Authors: Josep Sala[1], Andreu Urruela[1], Xavier Villares[1], Robert Estalella[2], Josep M. Paredes[2]

Affiliation: [1]Dpt. of Signal Theory and communications, Universitat Politecnica de Catalunya, [2]Dpt. of Astronomy and Metereology, Universitat de Barcelona

ACT Researcher(s): Torsten Bondo, Andreas Rathke

Contacts:

Josep Sala
Tel: +34-93-4015894
Fax: +34-93-4016447
e-mail: alvarez@gps.tsc.upc.es

Leopold Summerer
Tel: +31(0)71565 – 5174
Fax: +31(0)71565 – 8018
e-mail: act@esa.int

Available on the ACT website
http://www.esa.int/act

Ariadna ID: 03/4202
Study Duration: 2 months
Contract Number: 18148/04/NL/MV

Feasibility Study for a Spacecraft Navigation System relying on Pulsar Timing Information

ARIADNA Study 03/4202

(Final Report)

Josep Sala, Andreu Urruela, Xavier Villares
Dpt. of Signal Theory and Communications, Universitat Politècnica de Catalunya
c/Jordi Girona 1-3, Campus Nord UPC, D5-114b, 08034 Barcelona, SPAIN
Phone:+34-93-4015894, Fax:+34-93-4016447
E-mail: {alvarez,andreu}@gps.tsc.upc.es

Robert Estalella, Josep M. Paredes
Dpt. of Astronomy and Metereology, Universitat de Barcelona
Av. Diagonal 647, Barcelona, SPAIN
E-mail: robert@am.ub.es, jmparedes@ub.edu

June 23, 2004

Contents

Chapter 1

Introduction

This document addresses a feasibility study of a deep space navigation system based on pulsar timing information. The extreme frequency stability of radio and X-ray pulsars and their ubiquity have been considered in the past for positioning purposes. Although many different aspects need be addressed in the design of a system capable of self-positioning in volumes at Solar System scale, the emphasis in this study is placed upon the signal processing issues. In particular, the following points are addressed:

- Physical aspects related with the characterization of signals received from radio and X-ray pulsars.
- Signal processing for Time of Arrival and drift estimation.
- Signal processing for positioning estimation.
- Impact of location accuracy on instruments.

Our main objective has been to perform a high-level analysis of the signal model to determine the accuracy/complexity trade-offs attainable from pulsar signals. Although sometimes more advanced signal processing than that exposed in this study would be required for enhanced accuracy, reasonable simplifications have been performed to obtain meaningful trade-off curves as far as feasibility is concerned.

1.1 Navigation System Structure

This feasibility study considers a special structure for the navigation system, where processing is carried out in a hierarchy of levels, not necessarily presented in the same order in the document:

- instrumental stage: antennas or X-ray detectors.
- timing estimation stage: estimation of pulsar timing parameters.
- position estimation stage: determination of position.
- navigation stage: higher levels of navigational information.

A depiction is provided in figure (1.1). In this way, closed form expressions have been obtained for the parameters of interest. The signal model is characterized in the leading chapters, where a radio and X-ray pulsar database is presented. A chapter on stochastic models for the pulsar signal has been introduced for statistical characterization of the pulsar and noise signals. The position estimation stage, which utilizes timing estimates from the next lower level of processing, is introduced first in the document, followed by the chapters on timing estimation for radio and X-ray pulsars. In the last chapters, feasibility results are obtained and the corresponding conclusions are drawn. A technological overview of instruments is also included.

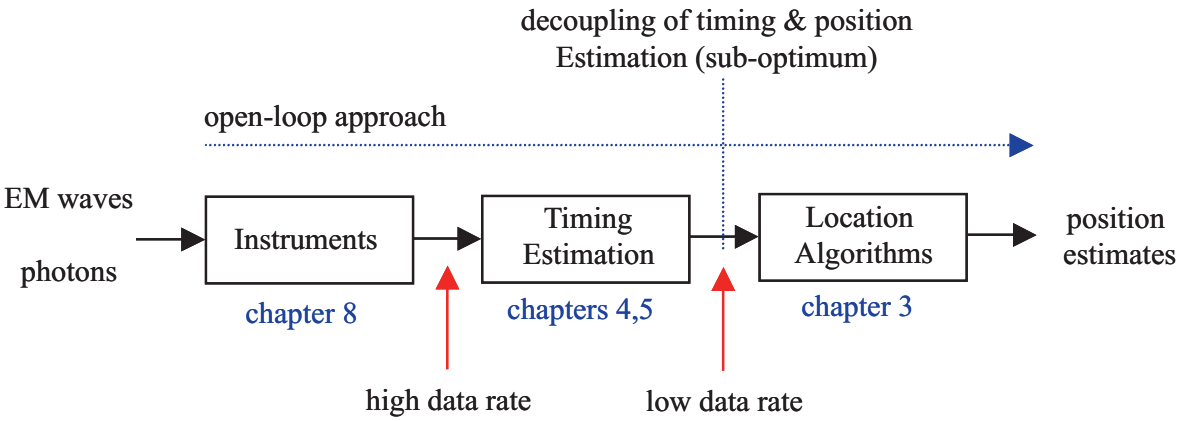

Figure 1.1: Depiction of the navigation system structure assumed for this study. The first stage (instruments) converts EM waves/photons to raw input signals to the digital signal processing stages. Decoupling of timing (second stage) and location (third stage) parameter estimation has been considered for ease of implementation and obtention of closed-form expressions of performance measures. Timing estimation uses information from a pulsar database to compare measured pulse arrival times with expected pulse arrival times. The location stage uses this differential information to derive a position estimate. All processing is carried out by an open-loop architecture, except at the location processor where timing estimates from previous data blocks are used in obtaining the current position estimate.

Chapter 2

Pulsar Database

This section provides a compilation of all pulsar features and parameters of import to the design of a pulsar navigation system.

2.1 Pulsar properties

2.1.1 Distribution

Radio pulsars are powered by the rotation of a neutron star, implying a great stability of the pulsar period, steadily increasing as the pulsar releases its rotational energy. Some 1300 pulsars are known at present (PSRCAT 2004), and more are discovered in every new survey (see, for instance, Hobbs et al. 2004). The great majority of pulsars are galactic objects, with a distribution concentrated along the galactic plane. In Figs. 2.1 and 2.2 we show the distribution a pulsar selection in galactic coordinates —coordinate system where the fundamental plane ($b = 0$) is the galactic plane and the origin of longitude ($l = 0$) is toward the galactic center. In Figs. 2.3 and 2.4 we show the distribution of the same pulsars in ecliptic coordinates —coordinate system where the fundamental plane ($b_{\mathrm{E}} = 0$) is the ecliptic, the plane of the orbit of the Earth around the Sun, and the origin of longitude ($l_{\mathrm{E}} = 0$) is toward the Aries point (the intersection of the ecliptic and the equatorial plane of the Earth). Pulsars usually show high proper motions, of several tens of mas yr^{-1}.

2.1.2 Period and pulse

Pulsar periods range from a millisecond to a few seconds. Most of millisecond pulsars belong to binary systems, their pulse arrival time being affected by the system orbital motion.

In some pulsars irregularities in their rotation speed have been observed every few years. These irregularities are known as 'glitches'. For the Vela pulsar, the fractional changes in rotational speed can be of the order of 10^{-6}, while for the Crab pulsar, they are only of 10^{-8}.

Pulsars emit only a pulse of radiation during a small fraction of the rotation period. Although individual pulses vary in strength and shape, the average pulse shape is stable and characteristic of each pulsar. In Figs. 2.5 and 2.6 we show the pulse profile of a selection of pulsars.

2.1.3 Flux density

Pulsars have in general steep power-law spectra, with spectral indices α ($S_\nu \propto \nu^\alpha$) ranging from -3.0 to -0.1, with a median value of ~ -1.7. The strongest pulsar at 1 GHz has a flux density of 1.7 Jy (1 Jy = 10^{-26} W m^{-2} Hz^{-1}). In Fig. 2.7 we show the spectra of a selection of pulsars between 0.1 and 10 GHz.

2.2 Pulsars selection

2.2.1 Signal-to-noise ratio

We can express the signal-to-noise ratio of a pulsar observation as the ratio of the average spectral power $w_{\mathrm{p,T}}$ (W Hz^{-1}) received by the antenna from the pulsar (averaged over the pulsar period T), $w_{\mathrm{p,T}} \equiv \sigma^2_{\mathrm{p,T}}$, and the equivalent noise spectral power w_{n} at the antenna terminals, $w_{\mathrm{n}} \equiv \sigma^2_{\mathrm{n}}$,

$$\mathrm{SNR} = \frac{\sigma^2_{\mathrm{p,T}}}{\sigma^2_{\mathrm{n}}} = \frac{w_{\mathrm{p,T}}}{w_{\mathrm{n}}}. \tag{2.1}$$

As we will see in sections 2.3 and 2.4, the SNR can be given as

$$\mathrm{SNR} = \frac{1}{2k}\, A_{\mathrm{e}}\, S_{\nu,\mathrm{T}}\, T^{-1}_{\mathrm{sys}}, \tag{2.2}$$

where k is the Boltzmann constant ($k = 1.38 \times 10^{-23}$ W Hz^{-1} K^{-1}), A_{e} (m^2) is the effective aperture area of the antenna, $S_{\nu,\mathrm{T}}$ is the pulsar flux density average over the pulsar period, and T_{sys} (K) is the system temperature, which takes into account the receiver noise and the radiation picked up by the antenna and not coming from the pulsar (see section 2.4). In practical units, the last equation becomes

$$\mathrm{SNR} = 3.6 \times 10^{-4} \left[\frac{A_{\mathrm{e}}}{\mathrm{m}^2}\right] \left[\frac{S_{\nu,\mathrm{T}}}{\mathrm{Jy}}\right] \left[\frac{T_{\mathrm{sys}}}{\mathrm{K}}\right]^{-1}. \tag{2.3}$$

For an antenna with an effective aperture of 10 m^2, a pulsar flux density of 100 mJy, and a system temperature of 40 K, the resulting SNR is 9.0×10^{-6}, or -50 dB.

2.2.2 Pulsar quality factor

The pulsar quality factor, Q, defined as the inverse of the expected error in position (m) per sample, is proportional to the SNR, the square root of the pulsar period, and approximately to the $-3/2$ power of the pulse width. For a practical use, we calculated the quality factor referred to an accuracy of $\sigma_{\mathrm{x}} = 10^6$ m, per $L = 10^9$ samples, which is given by

$$Q = \frac{\sigma_{\mathrm{x}}}{c \cdot \sigma_{\tau,L}} = 754.8\,\mathrm{SNR}\,\sqrt{T}\,\frac{1}{5T_{10} + 7T_{50}}\sqrt{\frac{5T_{10} - T_{50}}{T_{50}(T_{10} - T_{50})}}, \tag{2.4}$$

where $\sigma_{\tau,L}$ is the standard deviation of the synchronization error for the given L[1], c the speed of light, T is the pulsar rotational period, and T_{50} and T_{10} are the pulse widths at 50% and 10% of peak intensity. We used this expression of the quality factor to select the best pulsars. The list of selected pulsars is given in Tables 2.1 and 2.2. The first 15 pulsars of the list comprise 5 pulsars with period under 100 ms. No binary pulsar has been considered, since there are enough high quality millisecond non-binary pulsars. The pulsars that present glitches (including the Vela and Crab pulsars) have not been included in the selection. In Fig. 2.13 we show the dependence of the quality factor of these pulsars with frequency.

The rest of the list, up to a total of 50 pulsars, show the best quality factor pulsars. In Table 2.1 we give the pulsar coordinates, spectral index and flux density at 1 GHz. The last columns give the system temperature T_{sys} at 1 GHz, estimated from Eqs. 2.7, 2.9, and 2.16, for a beam efficiency $\eta_{\mathrm{M}} = 0.9$, the resulting SNR at 1 GHz for an effective aperture area of 10 m^2, and the quality factor at 1 GHz per 10^9 samples, referred to an accuracy of 10^6 m. In Table 2.2 we show the pulse properties of the selected pulsars.

2.3 Signal from the pulsar

The spectral power average over the pulsar period, $w_{\mathrm{p,T}}$, received by the antenna from the pulsar is given by

$$w_{\mathrm{p,T}} = \frac{1}{2}\, A_{\mathrm{e}}\, S_{\nu,T}. \tag{2.5}$$

[1] It is shown in the Timing Estimation chapter that $\sigma_{\tau,L}$ is proportional to $L^{-1/2}$.

The factor 1/2 in the last equation is exact for non polarized emission. Taking into account the degree of polarization of the pulsar radiation, $\Pi = \sqrt{Q^2 + U^2 + V^2}/I$ (in terms of the Stokes parameters), the correct factor ranges from $(1 - \Pi)/2$ to $(1 + \Pi)/2$, depending on the coupling of the polarization of the pulsar radiation and the polarization of the antenna.

2.4 System noise

The equivalent noise spectral power $w_{\rm n}$ at the antenna terminals can be given in terms of the system noise temperature, $T_{\rm sys}$ (K),

$$w_{\rm n} = k\, T_{\rm sys}. \tag{2.6}$$

The two contributions to the system temperature are the receiver noise temperature, $T_{\rm rx}$, and the sky temperature, $T_{\rm sky}$,

$$T_{\rm sys} = T_{\rm rx} + T_{\rm sky}. \tag{2.7}$$

The sky temperature accounts for the radiation arriving at the antenna and not coming from the pulsar. It has two main constant contributions, the isotropic cosmic background radiation, $T_{\rm cbg} = 2.7\,{\rm K}$ (independent on frequency), and the background radiation from the Galaxy, $T_{\rm gal}$, plus a time-variable contribution from Solar System objects, $T_{\rm sso}$,

$$T_{\rm sky} = T_{\rm cbg} + T_{\rm gal} + T_{\rm sso}. \tag{2.8}$$

The brightest Solar System objects are the Sun and Jupiter, which emit variable non-thermal radiation and can be very bright at radio frequencies.

2.4.1 Receiver temperature

The receiver temperature depends on the observing frequency. At low frequencies the limit is due to the physical temperature at which the front end is cooled (4 K using liquid He). However, helium cooling is difficult to use in a long duration spacecraft, and we will adopt a more conservative low-frequency receiver temperature limit of 30 K. At high frequencies the quantum noise limit, $h\nu/k$ is relevant. Current technology can reach about six times the quantum limit. Thus, we can consider a receiver noise temperature given by

$$\left[\frac{T_{\rm rx}}{\rm K}\right] = 30 + 6\,\frac{h\nu}{k} = 30 + 0.29\,\left[\frac{\nu}{\rm GHz}\right]. \tag{2.9}$$

2.4.2 Galactic background radiation

The galactic background radiation can be described by a brightness temperature $T_{\rm G}$, function of the galactic coordinates (l, b), which peaks at the galactic equator ($b = 0$), with a maximum at the galactic center $(l, b) = (0, 0)$ (See Fig. 2.9).

The contribution of the galactic radiation to the sky temperature can be evaluated as

$$T_{\rm gal} = \frac{1}{\Omega_{\rm A}} \int_{4\pi} P_{\rm n}(l, b)\, T_{\rm G}(l, b)\, d\Omega, \tag{2.10}$$

where $P_{\rm n}(l, b)$ is the antenna power radiation pattern, normalized so that $\max(P_{\rm n}) = 1$, and $\Omega_{\rm A}$ is the antenna solid angle,

$$\Omega_{\rm A} = \int_{4\pi} P_{\rm n}(\theta, \phi)\, d\Omega. \tag{2.11}$$

The integral over 4π sr can be decomposed into two contributions, one coming from the main beam (a small solid angle, with a high value of the antenna power pattern) and another from the rest of the beam (outside the main beam), where the antenna power pattern is low, but the solid angle is large. The contribution from the main beam can be approximated by

$$\int_{\rm MB} P_{\rm n}(l, b)\, T_{\rm G}(l, b)\, d\Omega \simeq \Omega_{\rm M}\, T_{\rm G}(l_{\rm p}, b_{\rm p}), \tag{2.12}$$

where $(l_{\rm p}, b_{\rm p})$ are the galactic coordinates of the pulsar, and $\Omega_{\rm M}$ is the main beam solid angle,

$$\Omega_{\rm M} = \int_{\rm MB} P_{\rm n}(\theta, \phi)\, d\Omega. \tag{2.13}$$

This approximation is valid for a highly directive antenna. The other contribution can estimated as

$$\int_{4\pi-{\rm MB}} P_{\rm n}(l, b)\, T_{\rm G}(l, b)\, d\Omega \simeq (\Omega_{\rm A} - \Omega_{\rm M})\, \langle T_{\rm G} \rangle, \tag{2.14}$$

$\langle T_{\rm G} \rangle$ being the average galactic temperature,

$$\langle T_{\rm G} \rangle = \frac{1}{4\pi} \int_{4\pi} T_{\rm G}(l, b)\, d\Omega. \tag{2.15}$$

Thus, by substitution into Eq. 2.10, we obtain

$$T_{\rm gal} = \eta_{\rm M}\, T_{\rm G}(l_{\rm p}, b_{\rm p}) + (1 - \eta_{\rm M})\, \langle T_{\rm G} \rangle, \tag{2.16}$$

where $\eta_{\rm M}$ is the beam efficiency, defined as $\eta_{\rm M} = \Omega_{\rm M}/\Omega_{\rm A}$. If the pulsar is far from the galactic plane ($|b| > 20^\circ$ approx.), $T_{\rm G}(l_{\rm p}, b_{\rm p})$ will be of the same order as $\langle T_{\rm G} \rangle$, and $T_{\rm gal} \simeq \langle T_{\rm G} \rangle$.

Since the galactic background radiation is non-thermal, its brightness temperature depends strongly on the frequency of observation. For frequencies above 0.1 GHz, the brightness temperature is a power law of frequency with a spectral index ~ -2.2 ($T_{\rm G} \propto \nu^{-2.2}$) (Brown 1974). In the direction of the Galactic center (GC), the Galactic temperature can be roughly estimated to be 40 K at 1 GHz, while in the anticenter direction (AC) and in the galactic poles (GP), the temperature is roughly ten times lower ($T_{\rm G}({\rm AC}) \simeq 5$ K and $T_{\rm G}({\rm GP}) \simeq 3$ K at 1 GHz). ¿From the map of galactic background radiation at 150 MHz (Landecker & Wielebinsky 1970) (see Fig. 2.9), the average galactic temperature at 150 MHz is 385 K, corresponding to

$$\left[\frac{\langle T_{\rm G} \rangle}{\rm K}\right] \simeq 6 \left[\frac{\nu}{\rm GHz}\right]^{-2.2}. \tag{2.17}$$

2.4.3 Emission from the Sun

The radio emission from the Sun consists of a steady component (the quiet Sun), a slowly varying component linked to the solar activity (sunspots) with a 11 year cycle of minimum and maximum activity, and finally, a rapidly varying component consisting of bursts linked to solar flares, especially important at frequencies of tens of MHz. In Fig. 2.10 we show the minimum and maximum flux density of the solar emission between 0.1 and 10 GHz, at a distance of 1 AU from the Sun. At 1 GHz the minimum and maximum flux densities are 2×10^5 and 5×10^7 Jy. Flux density scales as the inverse of the square of the distance. For frequencies between 0.1 and 10 GHz the Sun flux density at a distance of 1 AU, S^1_ν, can be roughly approximated by the expressions

$$\left[\frac{S^1_\nu}{\rm Jy}\right] \simeq \begin{cases} 2 \times 10^5\, [\nu/{\rm GHz}] & ({\rm quiet\ Sun}), \\ 5 \times 10^7\, [\nu/{\rm GHz}]^{-0.7} & ({\rm active\ Sun}). \end{cases} \tag{2.18}$$

The Sun emission is strong enough to make impossible the observation of any pulsar when the antenna main lobe points to the Sun. This can occur occasionally for pulsars located in the ecliptic plane (see Fig. 2.1). But even when the antenna is pointing away from the Sun direction, solar radiation can be picked up by the sidelobes of the antenna radiation pattern. The contribution to the sky temperature of the Sun radiation picked up by a sidelobe with level $d_{\rm sl}$ relative to the main lobe, is given by

$$\left[\frac{T_{\rm sun}}{\rm K}\right] = 3.6 \times 10^{-4}\, d_{\rm sl} \left[\frac{A_{\rm e}}{\rm m^2}\right] \left[\frac{S^1_\nu}{\rm Jy}\right] \left[\frac{d}{\rm AU}\right]^{-2}, \tag{2.19}$$

where d is the distance to the Sun. For a sidelobe level of -30 dB, an effective area of 10 m^2, a distance of 1 AU, and the flux density of the quiet Sun at 1 GHz, the Sun antenna temperature is $T_{\rm sun}({\rm quiet}) = 1$ K. However, with the same conditions for the maximum flux density of the active Sun, the Sun temperature is

$T_{\rm sun}$(active) = 180 K. Thus, for distances from the Sun $d \lesssim 10$ AU, the active Sun can increase significantly the system temperature and degrade the SNR. In Figs. 2.11 we show the SNR as a function of frequency for the observation of the 15 best Q pulsars, assuming an effective area $A_{\rm e} = 10$ m^2, a beam efficiency $\eta_{\rm M} = 0.9$, and no contribution from the Sun emission. As a comparison, in Fig. 2.12 we show the SNR for the same pulsars in the same conditions, but for the maximum active Sun flux density at 1 AU as it enters the antenna through a sidelobe of -30 dB.

2.4.4 Emission from Jupiter and other planets

Jupiter is a sporadic very strong source at decameter wavelengths. However, at frequencies around 1 GHz, Jupiter is much fainter and its flux density is not extremely dependent on frequency (see Fig. 2.10). Jupiter intensity as observed from the Earth is ~ 6 Jy. This means a flux density at 1 GHz as a function of distance,

$$\left[\frac{S_\nu(\text{Jupiter})}{\text{Jy}}\right] \simeq 160 \left[\frac{d}{\text{AU}}\right]^{-2}. \tag{2.20}$$

This is about 3 orders of magnitude less than the Sun and thus, with a negligible effect on the SNR. The rest of planets are even fainter than Jupiter.

2.5 X-ray pulsars

X-ray pulsars can be grouped in two different families according to the powering source: accretion-powered pulsars and rotation-powered pulsars.

The accretion-powered pulsars are found in X-ray binary systems, which constitute the brightest class of X-ray sources in the sky. An X-ray binary contains either a neutron star or a black hole accreting material from a companion star. A neutron star with a strong magnetic field ($\sim 10^{12}$ G) will disrupt the accretion flow at several hundred neutron star radii and funnel material onto the magnetic poles. If the magnetic and rotation axes are misaligned, X-ray pulsations will be observed if the beamed emission from the magnetic poles rotates through the line of sight. There are 32 accretion-powered X-ray pulsars discovered (White et al. 1995), with pulse periods distributed between 0.069 s and 835 s. Long term monitoring of the pulse periods of these X-ray pulsars has revealed that the pulse period shows different types of behaviour: a) linear decrease with time (spin-up) with erratic variations around the trend, b) no long term trend and only a random walk in the period, c) a steady increase in the period (spin-down). Some examples of these fluctuations in pulse period are illustrated in Fig. 2.14. The pulse period fluctuations reflect inhomogeneities in the accretion flow. This type of pulsars are not suitable candidates for the project.

The rotation-powered pulsars are rapidly spinning and strongly magnetized neutron stars which are radiating at expense of rotational energy. For a long time the most luminous of all rotation-powered pulsars, the Crab pulsar, had been the only radio pulsar detected at X-ray energies. Today, as a result of observations with ROSAT and ASCA, 27 pulsars have been detected (Becker & Trumper 1997), with a range of spin periods between 1.6 ms and 530 ms. However, some of them have shown lack of pulsed emission at X-rays and/or the presence of glitches. These facts precluded them to be included in our list of suitable candidates. Finally, ten X-ray pulsars have been selected and are shown in Table 2.3.

2.5.1 Millisecond pulsars

Millisecond pulsars are distinguished by their small spin periods (P$\leq$ 20ms) and high rotational stability ($dP/dt \simeq 10^{-18} - 10^{-21}$). Among the rotation-powered pulsars with pulsed X-ray emission listed in Table 2.3 , there are four millisecond pulsars (PSR J0437$-$47, PSR B1821$-$24, PSR J2124$-$33 and PSR J0030+0451). PSR J0030+0451 was recently discovered, presenting a period of 4.8 ms and gross similarity between the radio and the X-ray pulse profile (Fig. 2.15)(Becker et al. 2001). In the case of PSR B1821$-$24, the pulse profile has narrow peaks (Fig. 2.16) while for PSR J0437$-$47 and PSR J2124$-$33 (Fig. 2.17) the pulse profiles are broad.

2.5.2 X-ray background

Maps of the soft X-ray diffuse background in the 0.1–2.0 keV band from the ROSAT all-sky survey are available in digital format in the World Wide Web through ROSAT home pages (Snowden et al. 1997). We show these maps in Fig. 2.18. The galactic center direction at energies above 0.5 keV is about 6 times brighter than the typical high-latitude flux and shows considerable structure.

We present in Table 2.4 the background values in counts per second and squared arcmin for each of the selected X-ray pulsar direction of the sky. The hydrogen column density is also presented in Table 2.4. These values have been calculated as the background that would be received per squared arcmin and have been obtained from the web page: http://heasarc.gsfc.nasa.gov/cgi-bin/Tools/xraybg/xraybg.pl

2.5.3 Detectability

To detect the X-ray pulses from a pulsar it is necessary to take into account the technical capabilities of the instrument, the background levels and the hydrogen column density at a given position on the sky, and the exposure time of the observation. We have explored how pulsed emission can be detected through the use of a proportional sensitive position counter like the PSPC detector onboard the satellite ROSAT. A first approach to determine the detectability of a source, taking into account the employed instrument, can be done through a formula that is useful to estimate the exposure time of an observation: $t > 25(B/A^2)$ (for at least 5σ detection), where A and B are the source and the background counts per second respectively (detector dependent).

ROSAT was an X-ray satellite that detected all the pulsars presented in Table 2.3. The mission on flight started in 1990 and was turned off in 1999. On September 11, 1994, after four years of successful operation, the PSPC was shut down to conserve the remaining detector gas. This remaining gas was used during 1997 in series of pointings to complete the all-sky survey coverage. PSPC detector had a field of view of two degrees, with a mean sensitivity in latitude of about 0.1 mCrab (0.015 ct/s) in the ROSAT XRT all sky survey. The temporal resolution of the PSPC detector was about 100 μs, sufficient to resolve X-ray pulses from millisecond pulsars. During the ROSAT all sky survey, the exposure times were different depending on the direction of the pointing, although being around 1000 seconds. About the location of the source, it could be estimated with 10-30". The effective area of the instrument was from 500–1000 cm^2 at 0.1 keV to 200–400 at 2 keV. There are value ranges because the off-set that goes from 1° to 0°. We will consider that we want to detect the pulsation with the PSPC camera of ROSAT in the XRT all sky survey mode. The mission imformation has been obtained from the ROSAT home page: http://heasarc.gsfc.nasa.gov/docs/rosat/appf/appf.html

As an example of the ROSAT XRT all sky survey detection capabilites, we have explored the possibility to detect the pulsations of a source located a 1 kpc of distance from us at galactic or mid-latitudes. We have taken a hydrogen column density of about 10^{21} cm^{-2}. In order to be detected, considering time exposures similar to those of XRT all sky survey observations (about 1000 s), the object should have a pulsed luminosity of about 5×10^{31} erg s^{-1}. Moreover, for each selected pulsar, we have estimated the number of counts per second expected for a ROSAT(PSPC)-like instrument in three energy bands (R12=0.12–0.284 keV, R45=0.47–1.21 keV, R67=0.76-2.04 keV). The obtained results can be seen in Table 2.4. These calculations have been performed with the HEASARC tools of the web page: http://heasarc.gsfc.nasa.gov/Tools/w3pimms.html

Regarding the observation of the X-ray pulsars on-flight, a moderate number of detectors of relatively small field of view can be used if those pulsars can be roughly tracked through the attitude control of the spacecraft. In such a case, fixed pointings to selected pulsars could be carried out, allowing the permanent observation of their pulsed emission.

2.5.4 X-ray pulse profile

In order to determine the shape of the pulsation, it is necessary to split the X-ray pulse in several bins. The bin duration is constrained by both the timing resolution of the instrument and the total integration time. The second constraint comes from the fact that each bin should have counts enough for being significantly above the background, which implies that smaller bins require longer exposure times.

For instance, the ROSAT detector PSPC, with its 100 μs timing resolution, was able to resolve the X-ray pulse of a millisecond pulsar. Otherwise, from the sensitivity point of view, if the pulse is splitted

in 10 bins, the averaged number of counts per bin will be ten times smaller than for the whole pulse. It would imply that roughly the exposure time will be increased by a factor of one hundred. Therefore, for the ten bins case, the thousand of seconds of exposure mentioned above for the XRT all sky survey will turn to 10^5 s if we want to know the profile of the pulsation for an important fraction of the selected pulsars. Roughly speaking, if we want to split the pulse duration in n bins, the exposure will increase n^2 (see subsect. 2.5.3).

References

Becker, W., & Trumper, J. 1997, A&A 326, 682
Becker, W., Trumper, J., Lommen, A.N., Backer, D.C. 2001, ApJ, 545, 1015
Brown, R. L. 1974, in Galactic and Extra-Galactic Radio Astronomy, Springer-Verlag, p. 1
EPN 2004, The European Pulsar Network Data Archive, http://www.mpifr-bonn.mpg.de/div/pulsar/data/
Hobbs, G., Faulkner, A., Stairs, I. H. et al. 2004, MNRAS in press
Kraus, J. D. 1966, Radio Astronomy, McGraw-Hill, New York
Landecker, T. L., & Wielebinsky, R. 1970, Aust. J. Phys. astrophys. Suppl., 16, 1
PSRCAT 2004, ATNF Pulsar Catalogue, http://www.atnf.csiro.au/research/pulsar
Roberts & Stanley 1959, PASP, 71, 485
Snowden, S.L. et al. 1997, ApJ 485, 125
White, N.E. et al. 1995, in X-ray binaries, Cambridge Astrophysics Series, p.1

Table 2.1: 50 best Q pulsars: coordinates, flux density, SNR, Q

Name	l_{E}[a] (deg)	b_{E}[a] (deg)	l[b] (deg)	b[b] (deg)	α[c] (h)	δ[c] (deg)	DM[d] (cm^{-3} pc)	Spectral[e] Index	$S_{\nu,\mathrm{T}}$[f] (mJy)	T_{gal}[g] (K)	T_{sys}[h] (K)	SNR[i] (dB)	Q[j] (dB)
B1937+21	301.82	42.30	57.51	−0.29	19.661	21.58	71.04	−2.2	33.1	10.8	43.3	−55.6	11.8
B0329+54	65.19	34.26	145.00	−1.22	3.550	54.58	26.83	−1.6	347.4	9.2	41.9	−45.2	4.5
B1642−03	250.19	18.86	14.11	26.06	16.751	−3.30	35.73	−2.3	46.1	6.4	39.4	−53.7	1.3
B0950+08	147.71	−4.62	228.91	43.70	9.886	7.93	2.96	−1.2	127.7	2.6	35.9	−48.9	−0.7
B0740−28	125.33	−48.71	243.77	−2.44	7.714	−28.38	73.76	−2.4	33.4	5.2	38.3	−55.0	−2.3
B1929+10	297.05	32.29	47.38	−3.88	19.537	10.99	3.18	−1.7	63.8	15.0	47.1	−53.1	−2.9
B1556−44	246.80	−23.57	334.54	6.37	15.995	−44.65	56.10	−0.8	52.5	24.9	56.0	−54.7	−3.8
B1451−68	246.26	−49.00	313.87	−8.54	14.933	−68.73	8.60	−1.2	118.9	10.7	43.2	−50.0	−3.8
B1449−64	243.26	−45.02	315.73	−4.43	14.892	−64.22	71.07	−2.2	29.7	16.0	48.0	−56.5	−4.1
B0835−41	150.63	−57.04	260.90	−0.34	8.623	−41.59	147.29	−2.0	31.4	6.7	39.6	−55.4	−4.1
B2020+28	317.95	46.59	68.86	−4.67	20.377	28.91	24.64	−0.5	44.9	11.7	44.1	−54.4	−4.2
J1617−5055	251.79	−29.09	332.50	−0.28	16.291	−50.92	467.00	−1.7	65.6	37.1	67.0	−54.5	−5.3
J1730−2304	263.14	0.19	3.14	6.02	17.506	−23.08	9.61	−2.0	7.2	23.2	54.5	−63.3	−6.4
B1821−24	275.57	−1.55	7.80	−5.58	18.409	−24.87	119.86	−4.3	0.8	34.8	64.9	−73.7	−7.7
J2322+2057	0.04	22.88	96.52	−37.31	23.373	20.95	13.37	−1.7	0.6	3.5	36.7	−72.4	−8.5
B2016+28	316.46	46.69	68.10	−3.98	20.301	28.67	14.17	−1.9	56.4	11.3	43.8	−53.3	−4.4
B1749−28	268.45	−4.68	1.54	−0.96	17.883	−28.11	50.37	−3.3	54.3	49.6	78.2	−56.0	−4.5
B0823+26	122.60	7.24	196.96	31.74	8.448	26.62	19.45	−1.6	17.1	2.8	36.1	−57.7	−4.6
B1240−64	225.40	−52.66	302.05	−1.53	12.721	−64.39	297.25	−1.7	23.1	13.2	45.5	−57.4	−4.6
B1933+16	299.33	37.31	52.44	−2.09	19.597	16.28	158.52	−1.4	67.2	13.2	45.5	−52.7	−4.7
B2310+42	10.60	43.12	104.41	−16.42	23.219	42.89	17.28	−1.4	24.2	5.6	38.6	−56.5	−5.8
B1133+16	168.15	12.16	241.90	69.20	11.601	15.85	4.86	−1.7	56.0	2.9	36.2	−52.5	−6.0
B2021+51	337.86	67.13	87.86	8.38	20.381	51.91	22.65	−0.8	35.8	10.1	42.7	−55.2	−6.1
B1557−50	248.66	−29.46	330.69	1.63	16.015	−50.74	260.56	−1.7	30.1	35.0	65.1	−57.8	−6.2
B1821−19	275.66	3.56	12.28	−3.11	18.400	−19.76	224.65	−2.1	10.0	31.7	62.1	−62.3	−6.4
B1356−60	233.08	−44.59	311.24	1.13	14.000	−60.64	293.71	−2.1	15.4	20.9	52.4	−59.8	−6.6
B1323−62	229.57	−48.10	307.07	0.21	13.455	−62.38	318.80	−1.7	28.4	19.5	51.1	−57.0	−7.1
B0736−40	130.28	−60.75	254.19	−9.19	7.642	−40.71	160.80	−0.7	100.9	5.2	38.3	−50.2	−7.5
B1713−40	261.42	−17.78	346.82	−1.73	17.289	−40.91	308.50	1.0	38.3	32.2	62.6	−56.6	−8.2
B1804−08	271.95	14.63	20.06	5.59	18.127	−8.80	112.38	−1.2	22.2	22.2	53.6	−58.3	−8.5
B1323−58	227.02	−45.27	307.50	3.57	13.450	−58.99	287.30	−2.0	19.3	16.2	48.2	−58.4	−8.7
B1508+55	188.03	67.22	91.33	52.29	15.157	55.53	19.61	−2.1	16.3	3.3	36.6	−57.9	−8.7
B1911−04	289.34	17.53	31.31	−7.12	19.232	−4.68	89.39	−2.6	10.6	22.2	53.6	−61.5	−8.7
B0136+57	48.56	43.80	129.22	−4.04	1.655	58.24	73.78	−1.4	7.5	9.5	42.1	−61.9	−8.9
B2217+47	3.29	52.54	98.39	−7.60	22.330	47.91	43.52	−2.9	7.9	7.4	40.3	−61.5	−9.1
B1046−58	201.08	−57.84	287.43	0.58	10.803	−58.53	129.10	−1.7	11.5	12.5	44.8	−60.3	−9.2
B1055−52	195.47	−52.39	285.98	6.65	10.966	−52.45	30.10	−1.7	16.8	6.2	39.2	−58.1	−9.3
B1221−63	222.53	−53.82	299.98	−1.42	12.406	−64.13	97.47	−2.0	7.7	11.6	44.0	−62.0	−9.4
B1702−19	257.14	3.72	3.19	13.03	17.093	−19.11	22.91	−1.0	11.3	9.9	42.5	−60.2	−9.5
B1953+50	327.05	68.80	84.79	11.55	19.922	51.00	31.97	6.6	8.6	41.3	41.3	−62.4	−9.7
B0450+55	79.04	32.91	152.62	7.55	4.902	55.73	14.49	19.5	8	40.8	40.8	−57.6	−9.7
B1727−47	264.76	−24.43	342.57	−7.67	17.528	−47.74	123.33	−2.2	25.2	17.7	49.5	−57.4	−9.9
B0540+23	86.14	0.10	184.36	−3.32	5.719	23.48	77.71	12.3	7.5	40.3	40.3	−59.6	−10.0
B1600−49	248.77	−27.80	332.15	2.44	16.073	−49.17	140.80	−1.7	9.6	34.0	64.2	−62.7	−10.1
B1818−04	275.50	18.88	25.46	4.73	18.348	−4.46	84.44	−2.6	14.6	25.3	56.4	−60.3	−10.4
B1358−63	235.86	−47.38	310.57	−2.14	14.031	−63.96	98.00	−1.4	9.8	19.5	51.1	−61.6	−10.5
B1426−66	241.53	−48.01	312.65	−5.40	14.511	−66.38	65.30	16.9	14.8	46.9	46.9	−58.9	−10.7
B1742−30	266.95	−7.27	358.55	−0.96	17.766	−30.67	88.37	−1.3	20.1	47.9	76.7	−60.3	−11.2
B1607−52	250.86	−30.50	330.92	−0.48	16.184	−52.16	127.57	2.1	36.5	66.4	66.4	−69.4	−11.6
B1719−37	262.29	−14.00	350.49	−0.51	17.383	−37.20	99.50	−1.6	5.6	37.2	67.1	−65.3	−11.7

[a] Ecliptic longitude and latitude.
[b] Galactic longitude and latitude.
[c] Right ascension and declination $J2000$.
[d] Dispersion measure.
[e] Between 0.4 and 1.4 GHz.
[f] At 1 GHz, average over the pulsar period
[g] Assuming $\eta_{\mathrm{M}} = 0.9$.
[h] Assuming no contribution from the Sun.
[i] Assuming $A_{\mathrm{e}} = 10\ \mathrm{m}^2$.
[j] Quality factor per 10^9 samples, referred to an accuracy of 10^6 m.

Table 2.2: 50 best Q pulsars: rotational period and pulse properties

Name	T^a (s)	$f_0{}^a$ (Hz)	$f_1{}^b$ (s^{-2})	$f_2{}^b$ (s^{-3})	Epoch^c (MJD)	$T_{50}{}^d$ (ms)	$T_{10}{}^d$ (ms)
B1937+21	0.001558	641.928261	-4.332×10^{-14}	4.00×10^{-26}	47899.5	0.10	0.199
B0329+54	0.714520	1.399542	-4.012×10^{-15}	5.30×10^{-28}	46473.0	6.60	31.400
B1642−03	0.387690	2.579382	-1.185×10^{-14}	6.60×10^{-27}	46515.0	4.20	8.000
B0950+08	0.253065	3.951551	-3.588×10^{-15}	-7.60×10^{-27}	46375.0	9.50	20.600
B0740−28	0.166762	5.996559	-6.049×10^{-13}	-1.32×10^{-24}	49326.0	5.40	8.300
B1929+10	0.226518	4.414667	-2.256×10^{-14}	1.50×10^{-26}	46523.0	7.40	14.000
B1556−44	0.257056	3.890201	-1.542×10^{-14}	...	46800.0	6.00	14.00a
B1451−68	0.263377	3.796841	-1.417×10^{-15}	...	46800.0	12.50	29.000
B1449−64	0.179485	5.571504	-8.524×10^{-14}	...	46800.0	4.40	9.700
B0835−41	0.751624	1.330453	-6.265×10^{-15}	...	51700.0	8.90	18.000
B2020+28	0.343402	2.912038	-1.606×10^{-14}	2.40×10^{-26}	49692.0	12.00	15.800
J1617−5055	0.069357	14.418187	-2.809×10^{-11}	...	50829.7	5.80	11.000
J1730−2304	0.008123	123.110289	-3.063×10^{-16}	...	50320.0	1.10	1.600
B1821−24	0.003054	327.405665	-1.735×10^{-13}	-3.30×10^{-26}	49858.0	0.15	0.300
J2322+2057	0.004808	207.968167	-4.195×10^{-16}	...	48900.0	0.17	0.600
B2016+28	0.557953	1.792264	-4.757×10^{-16}	4.86×10^{-27}	46384.0	14.90	22.200
B1749−28	0.562558	1.777596	-2.569×10^{-14}	1.30×10^{-26}	46483.0	9.10	15.000
B0823+26	0.530661	1.884444	-6.070×10^{-15}	1.50×10^{-26}	46450.0	5.80	12.400
B1240−64	0.388481	2.574129	-2.982×10^{-14}	...	46800.0	6.60	11.000
B1933+16	0.358738	2.787546	-4.664×10^{-14}	1.45×10^{-26}	46434.0	9.00	17.700
B2310+42	0.349434	2.861773	-9.203×10^{-16}	5.80×10^{-27}	48241.0	8.80	14.600
B1133+16	1.187913	0.841812	-2.646×10^{-15}	8.70×10^{-28}	46407.0	31.70	41.800
B2021+51	0.529197	1.889656	-1.094×10^{-14}	-2.27×10^{-26}	46640.0	7.40	29.400
B1557−50	0.192601	5.192075	-1.365×10^{-13}	...	49215.5	5.40	11.000
B1821−19	0.189335	5.281644	-1.459×10^{-13}	5.20×10^{-26}	49877.0	2.90	5.500
B1356−60	0.127501	7.843089	-3.899×10^{-13}	...	43555.7	3.90	7.400
B1323−62	0.529906	1.887126	-6.727×10^{-14}	...	43555.7	11.00	19.000
B0736−40	0.374920	2.667236	-1.150×10^{-14}	...	51700.0	29.00	52.000
B1713−40	0.887710	1.126494	$\times 10^{*}$	...	48013.8	15.00	30.000
B1804−08	0.163727	6.107714	-1.074×10^{-15}	-4.79×10^{-27}	48244.0	8.90	13.000
B1323−58	0.477991	2.092090	-1.417×10^{-14}	...	47781.8	7.60	23.000
B1508+55	0.739682	1.351932	-9.135×10^{-15}	5.16×10^{-26}	49904.0	10.90	26.300
B1911−04	0.825936	1.210748	-5.963×10^{-15}	1.61×10^{-26}	46634.0	7.50	14.900
B0136+57	0.272451	3.670390	$-1.443 \ldots$	1.60×10^{-26}	49289.0	5.20	9.600
B2217+47	0.538469	1.857118	-9.537×10^{-15}	-3.18×10^{-27}	46599.0	7.50	13.100
B1046−58	0.123671	8.085992	-6.298×10^{-12}	-3.90×10^{-22}	50889.0	5.60	9.700
B1055−52	0.197108	5.073371	-1.501×10^{-13}	...	43555.6	14.00	17.000
B1221−63	0.216476	4.619445	-1.057×10^{-13}	...	46800.0	6.10	9.100
B1702−19	0.298987	3.344622	-4.629×10^{-14}	3.34×10^{-26}	48733.0	7.30	14.700
B1953+50	0.518938	1.927013	-5.096×10^{-15}	-9.82×10^{-27}	48741.0	6.00	13.200
B0450+55	0.340729	2.934880	-2.043×10^{-14}	-1.79×10^{-25}	49910.0	8.10	29.100
B1727−47	0.829829	1.205068	-2.376×10^{-13}	5.60×10^{-24}	50939.0	20.00	32.000
B0540+23	0.245975	4.065458	-2.549×10^{-13}	2.42×10^{-25}	48892.0	6.20	18.900
B1600−49	0.327418	3.054204	-9.509×10^{-15}	...	46800.0	4.40	13.000
B1818−04	0.598076	1.672029	-1.770×10^{-14}	3.57×10^{-26}	46634.0	11.00	20.000
B1358−63	0.842790	1.186536	-2.355×10^{-14}	...	46800.0	10.00	19.000
B1426−66	0.785441	1.273170	-4.489×10^{-15}	...	46800.0	18.00	28.000
B1742−30	0.367429	2.721616	-7.902×10^{-14}	-8.30×10^{-26}	49890.0	7.80	23.000
B1607−52	0.182492	5.479702	-1.551×10^{-13}	...	48360.5	2.20	4.100
B1719−37	0.236173	4.234181	-1.946×10^{-13}	...	48381.0	4.00	9.000

[a] Pulsar rotational period, T, and frequency, f_0.

[b] First and second time derivatives of f_0.

[c] Modified Julian Date of pulse ephemeris.

[d] Pulse width at 50% and 10% of peak intensity.

Table 2.3: Characteristics of the radio, optical and X-ray detected rotation-powered pulsars

Name	l_E[a] (deg)	b_E[a] (deg)	detected[b] R O X	$\dot{E}/(4\pi d^2)$ (erg/s/cm^2)	lg $\dot{E}$[c] (erg/s)	lg[d] L_x^{tot} (erg/s)	lg[d] L_x^{puls} (erg/s)	lg[d] L_x^{pn} (erg/s)	P[e] (ms)	$\dot{P}\times10^{-15}$ (ss^{-1})
J0030+0451	8.91	1.45			–	–	∼29.8	–	4.8	–
B0633+17	98.11	−5.43	? d p	$1.1\ 10^{-8}$	34.51	31.10	30.62	–	237.09	10.97
B1509−58	243.89	−39.40	p d p	$7.7\ 10^{-9}$	37.25	34.29	34.10	35.3	150.23	1540.19
B1929+10	297.05	32.29	p d p	$1.1\ 10^{-9}$	33.59	30.00	29.5	–	226.51	1.16
J0437−47	50.47	−67.87	p - p	$1.0\ 10^{-9}$	33.62	30.86	30.3	–	5.75	$2.0\ 10^{-5}$
B1821−24	275.56	−1.55	p - p	$6.2\ 10^{-10}$	36.35	33.24	∼32.56	–	3.05	$1.6\ 10^{-3}$
B0656+14	104.64	−8.44	p p p	$5.5\ 10^{-10}$	34.58	32.98	32.15	–	384.87	55.03
B0540−69	301.63	−86.66	p p p	$5.1\ 10^{-10}$	38.17	36.21	36.1	37.2	50.37	479.06
J2124−33	312.74	−17.82	p - p	$4.7\ 10^{-10}$	33.55	30.35	29.8	–	4.93	$1.08\ 10^{-5}$
B1055−52	195.77	−52.39	p d p	$1.1\ 10^{-10}$	34.48	33.42	32.57	–	197.10	5.83

[a] Ecliptic longitude and latitude.
[b] Energy ranges in which pulsed (p), unpulsed (d) radiation has been detected: R:radio, O:optical, X:X-rays.
[c] $\dot{E}$ is the pulsar spin-down power.
[d] L_x^{tot} the sum of the pulsed and unpulsed X-ray luminosities; L_x^{puls} is the pulsed luminosity; L_x^{pn} is the total luminosity including nebula emission.
[e] Pulsar period.

Table 2.4: Characteristics of the radio, optical and X-ray detected rotation-powered pulsars(II)

Name	nH cm^{-2}	λ_p-R12[a] (ct/s)	λ_p-R45[a] (ct/s)	λ_p-R67[a] (ct/s)	λ_n-R12[a] (ct/s/arcmin^2)	λ_n-R45[a] (ct/s/arcmin^2)	λ_n-R67[a] (ct/s/arcmin^2)
J0030+0451	3.1×10^{20}	1.2×10^{-3}	4.1×10^{-3}	5.1×10^{-3}	5×10^{-4}	10^{-4}	1.2×10^{-4}
B0633+17	4.1×10^{21}	2.7×10^{-8}	3.5×10^{-2}	7.5×10^{-2}	7.2×10^{-4}	1.2×10^{-4}	1.3×10^{-4}
B1509−58	1.4×10^{22}	2.2×10^{-21}	3.2×10^{-2}	2×10^{-1}	4.4×10^{-4}	2×10^{-4}	4.5×10^{-4}
B1929+10	3.8×10^{21}	4.9×10^{-9}	2.4×10^{-3}	5.1×10^{-3}	4.2×10^{-4}	1.5×10^{-4}	1.8×10^{-4}
J0437−47	1.8×10^{20}	1.2×10^{-2}	2×10^{-2}	2.5×10^{-2}	9.8×10^{-4}	1.4×10^{-4}	1.4×10^{-4}
B1821−24	1.9×10^{21}	3×10^{-6}	3.6×10^{-3}	5.8×10^{-3}	3.4×10^{-4}	6.3×10^{-4}	6×10^{-4}
B0656+14	1.3×10^{21}	5.1×10^{-4}	8.1×10^{-2}	1.2×10^{-1}	8.4×10^{-4}	1.2×10^{-4}	1.3×10^{-4}
B0540−69	6.7×10^{20}	1.1×10^{-2}	1.8×10^{-1}	2.3×10^{-1}	4.6×10^{-4}	6.3×10^{-4}	5.7×10^{-4}
J2124−33	5.5×10^{20}	3.5×10^{-4}	3.5×10^{-3}	4.5×10^{-3}	4.7×10^{-4}	1.2×10^{-4}	1.4×10^{-4}
B1055−52	3.2×10^{21}	5.1×10^{-7}	3.9×10^{-2}	7.5×10^{-2}	4.7×10^{-4}	1.7×10^{-4}	1.5×10^{-4}

[a] Energy bands: R12=0.12–0.284 keV, R45=0.47–1.21 keV, R67=0.76-2.04 keV

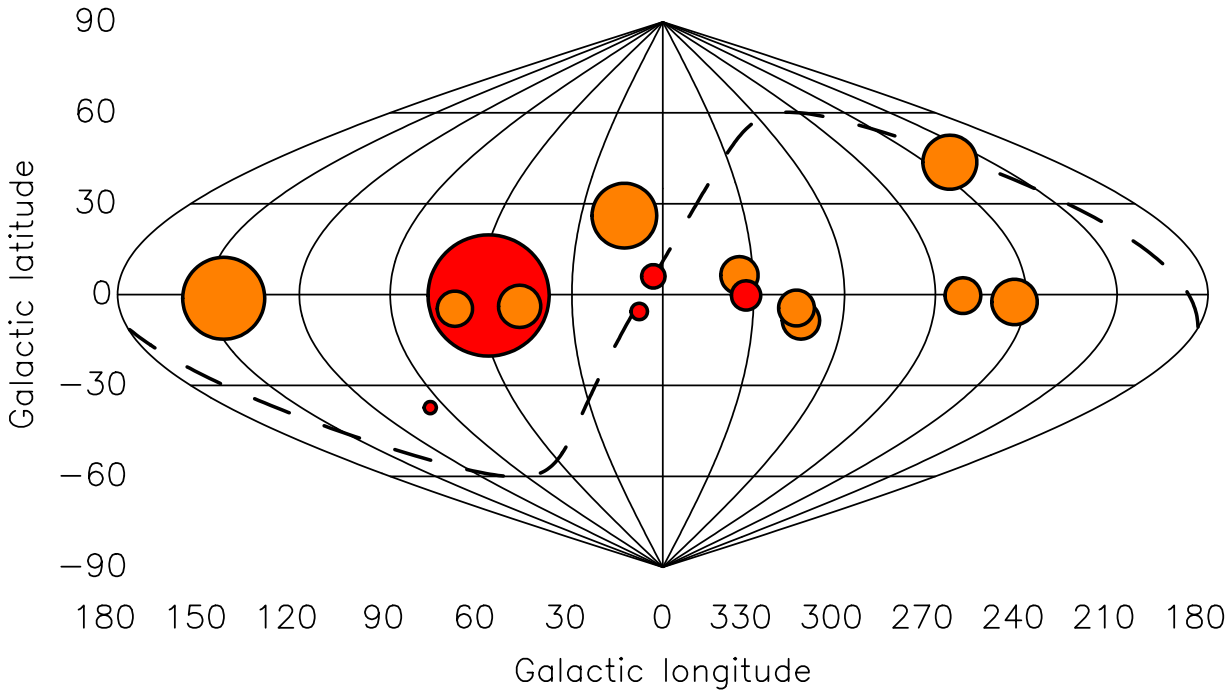

Figure 2.1: Position of the 15 best Q pulsars, in galactic coordinates. The sizes of the circles indicate the pulsar quality factor Q. Dark color circles indicate pulsars with periods under 100 ms, and light color circles correspond to pulsars with periods longer than 100 ms. The dashed line shows the ecliptic plane.

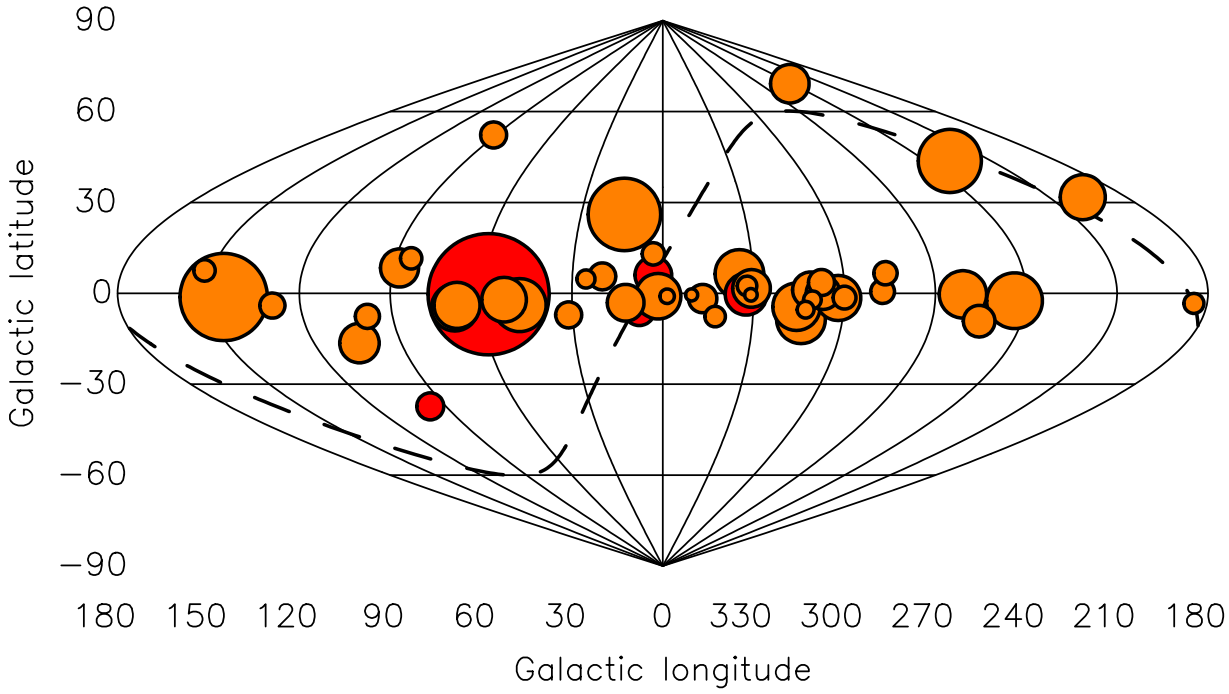

Figure 2.2: Same as Fig. 2.1 for the 50 best Q pulsars. Note that the pulsars appear concentrated along the galactic plane.

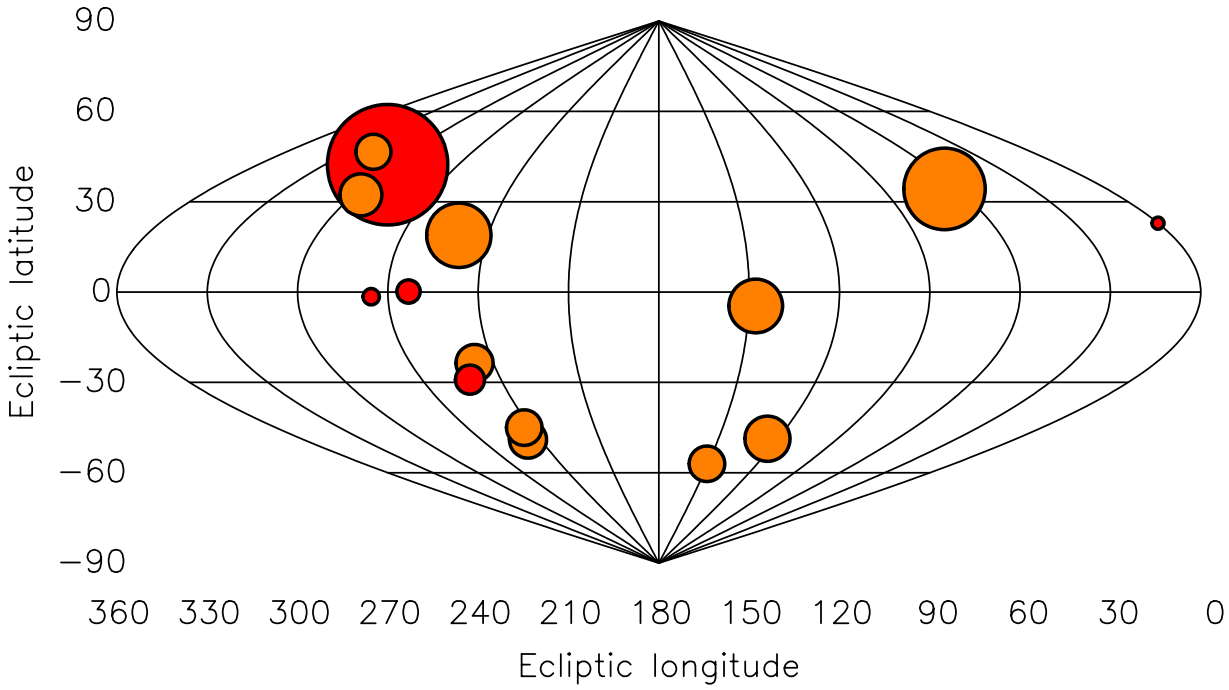

Figure 2.3: Same as Fig. 2.1, in ecliptic coordinates.

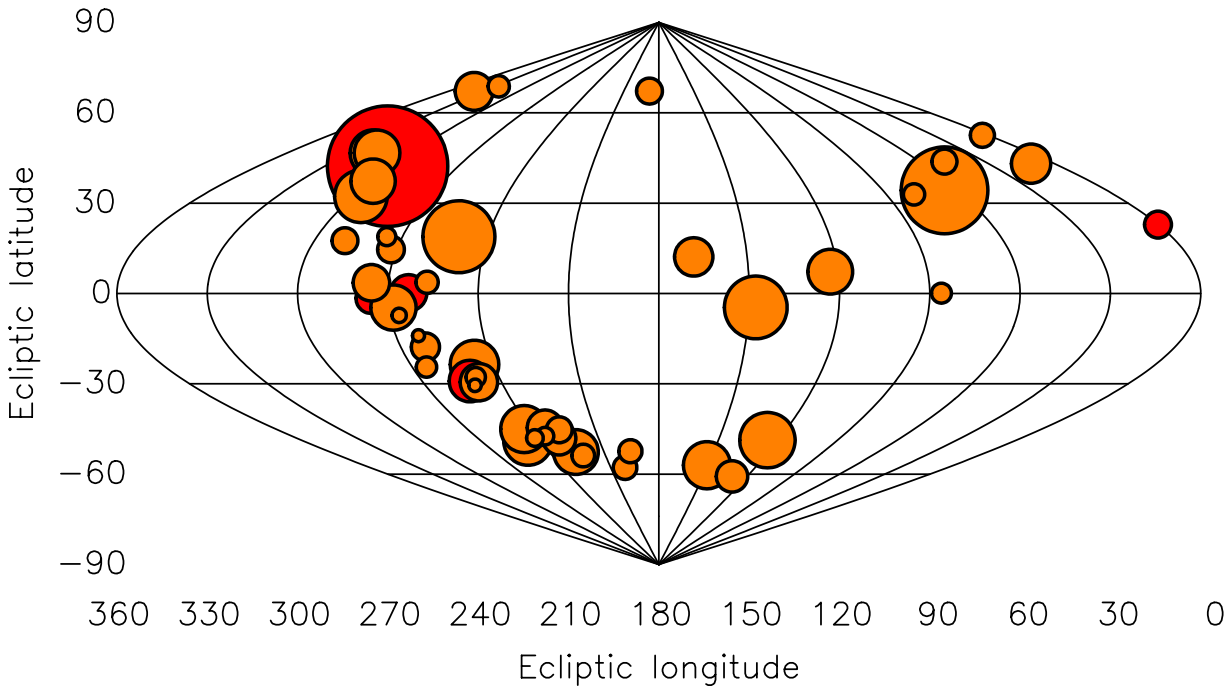

Figure 2.4: Same as Fig. 2.2, in ecliptic coordinates.

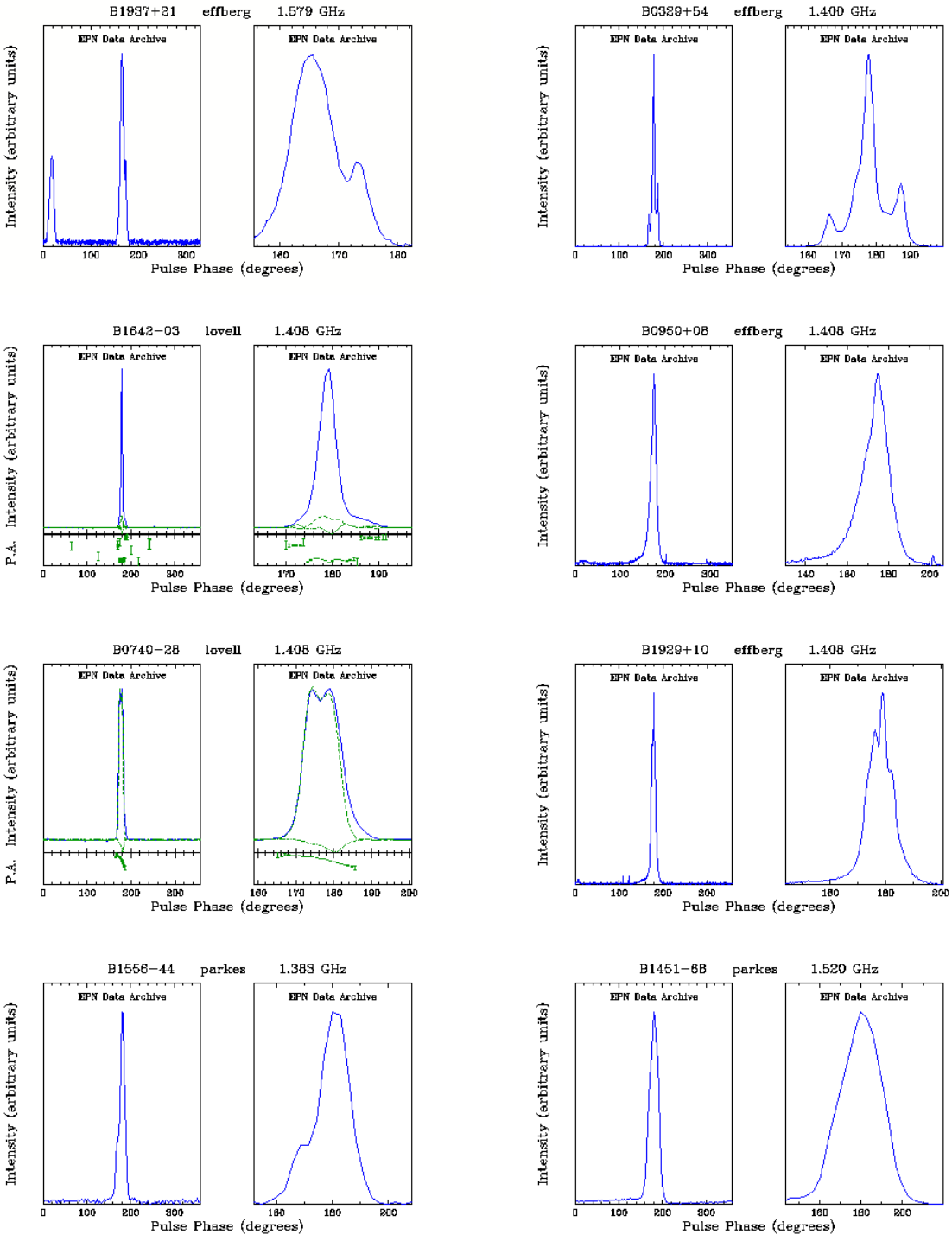

Figure 2.5: Pulse profiles of the selected pulsars (from EPN 2004).

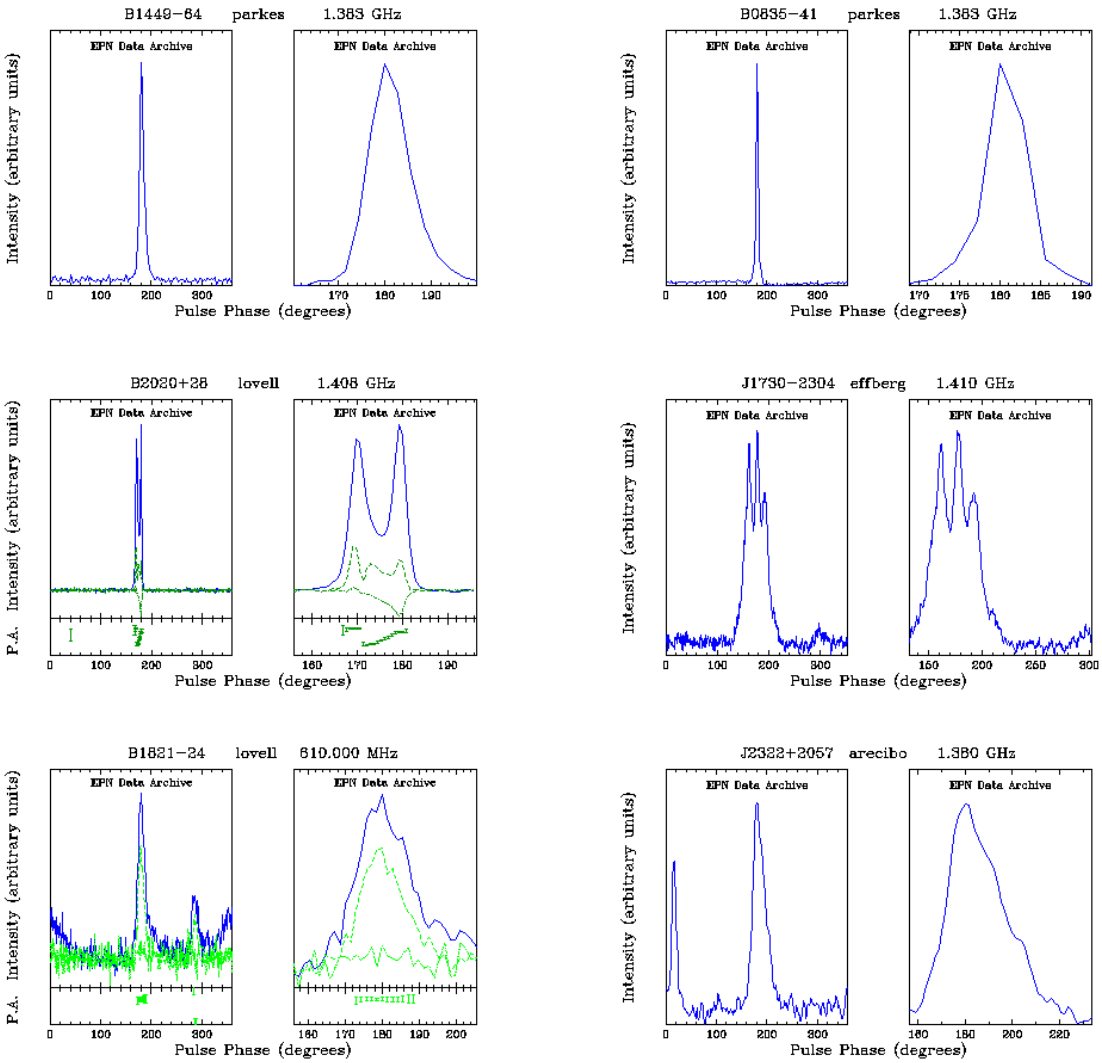

Figure 2.6: Pulse profiles *(continuation)*.

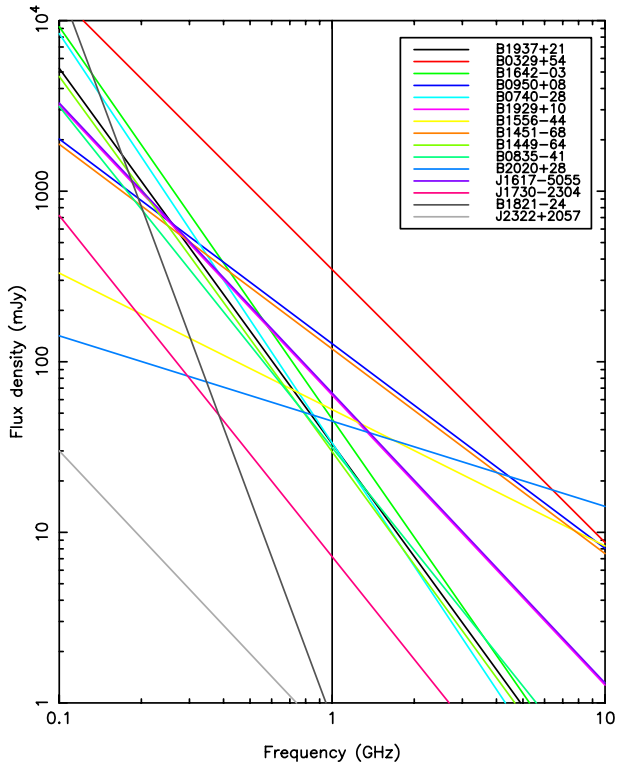

Figure 2.7: Flux density of the 15 best Q pulsars as a function of frequency.

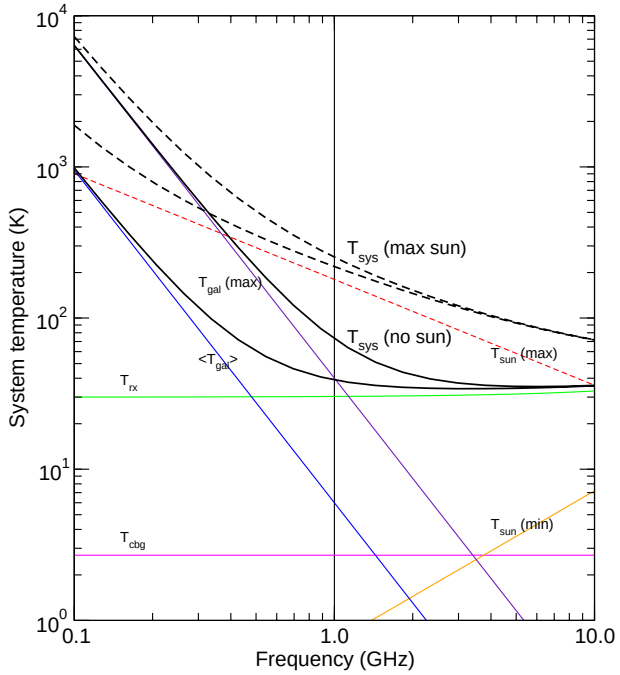

Figure 2.8: System temperature, $T_{\rm sys}$, as a function of frequency, showing the contributions from the receiver, $T_{\rm rx}$, from the cosmic background radiation, $T_{\rm cbg}$, from the galactic background radiation, $T_{\rm G}$ (its average and its maximum for the galactic center), and from solar radiation for a distance of 1 AU, an effective area of 10 m^2, and seen through a -30 dB sidelobe, $T_{\rm sun}$ (its minimum for the quiet Sun and maximum for the active Sun).

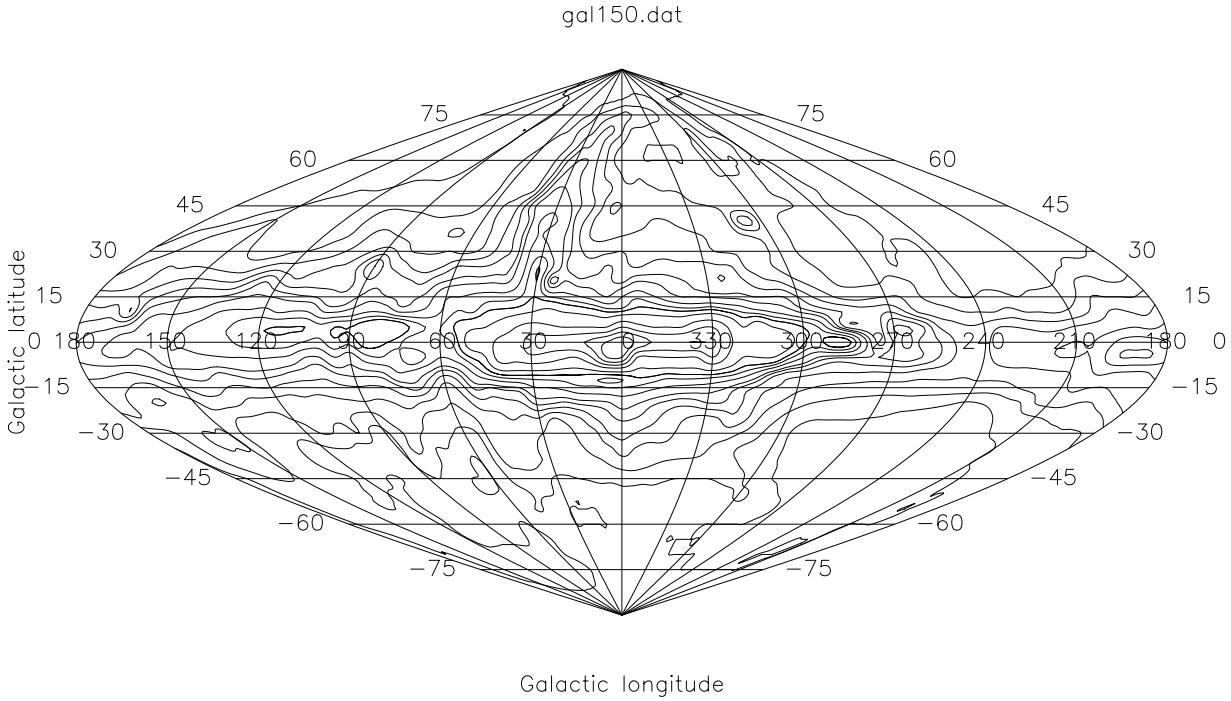

Figure 2.9: Galactic background brightness temperature at 150 MHz, in galactic coordinates. Contour levels are 200 K to 500 K in steps of 50 K, 600 K to 1000 K in steps of 100 K, 1200 K, and 1500 K to 3000 K in steps of 500 K.

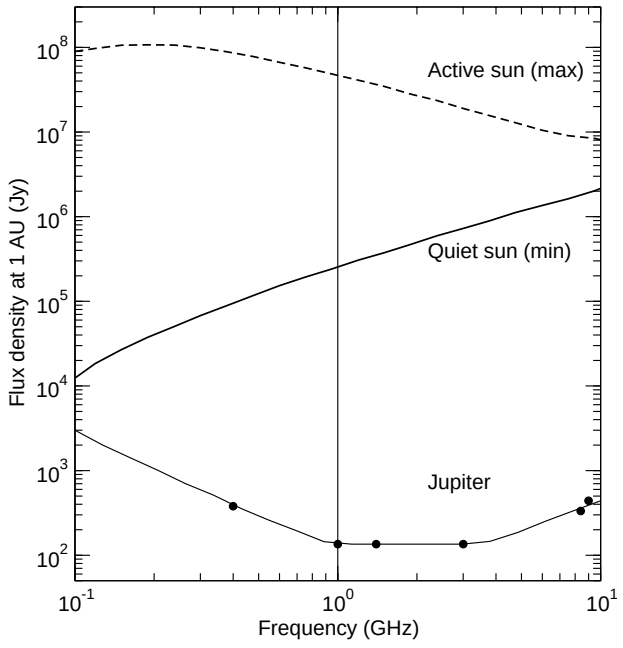

Figure 2.10: Flux density of the active and quiet Sun, and Jupiter, scaled for a distance of 1 AU (Kraus 1966; Roberts & Stanley 1959).

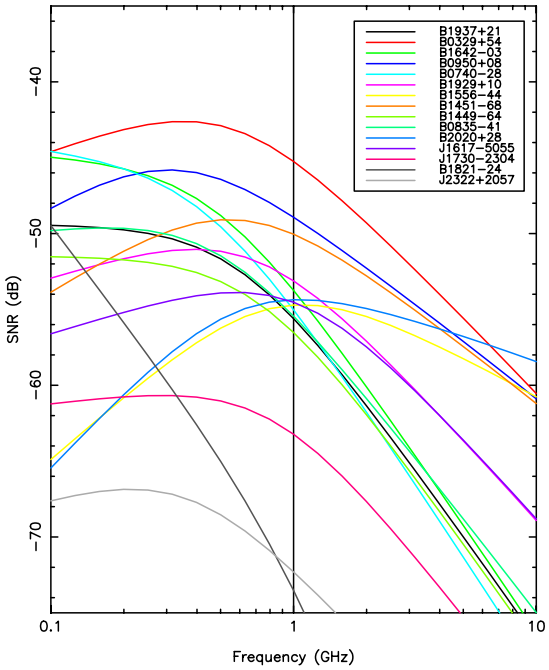

Figure 2.11: SNR as a function of frequency for the observation of the 15 best Q pulsars, assuming an effective area $A_{\mathrm{e}} = 10\ \mathrm{m}^2$, a beam efficiency $\eta_{\mathrm{M}} = 0.9$, and no contribution from the Sun emission.

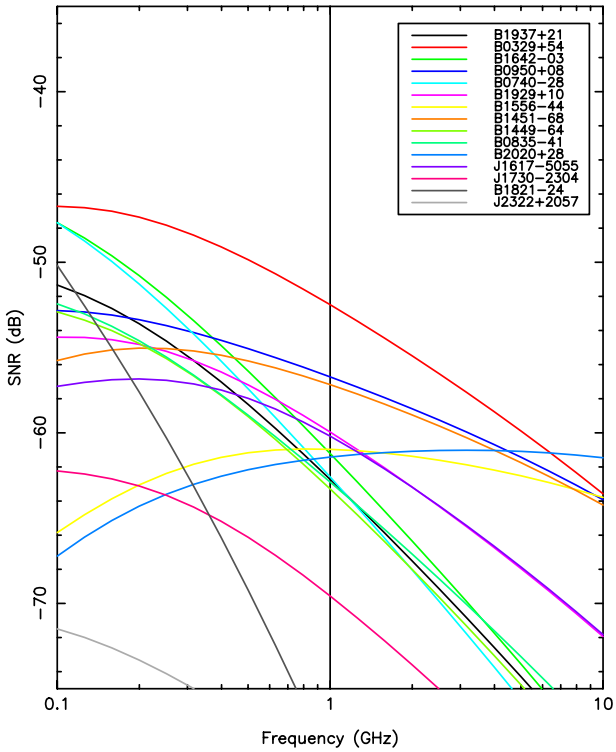

Figure 2.12: Same as Fig. 2.11 for the maximum active Sun flux density at 1 AU.

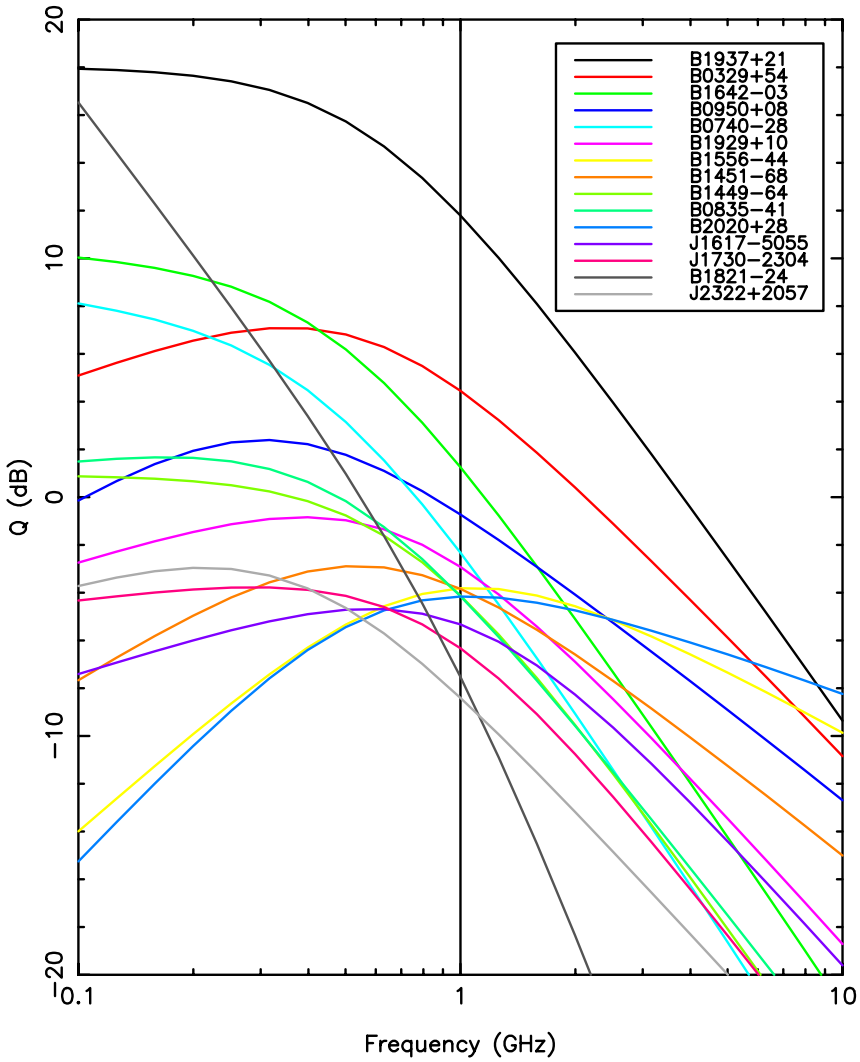

Figure 2.13: Quality factor Q per 10^9 samples, referred to an accuracy of 10^6 m, as a function of frequency for the observation of the 15 best Q pulsars, assuming an effective area $A_e = 10$ m^2, a beam efficiency $\eta_M = 0.9$, and no contribution from the Sun emission.

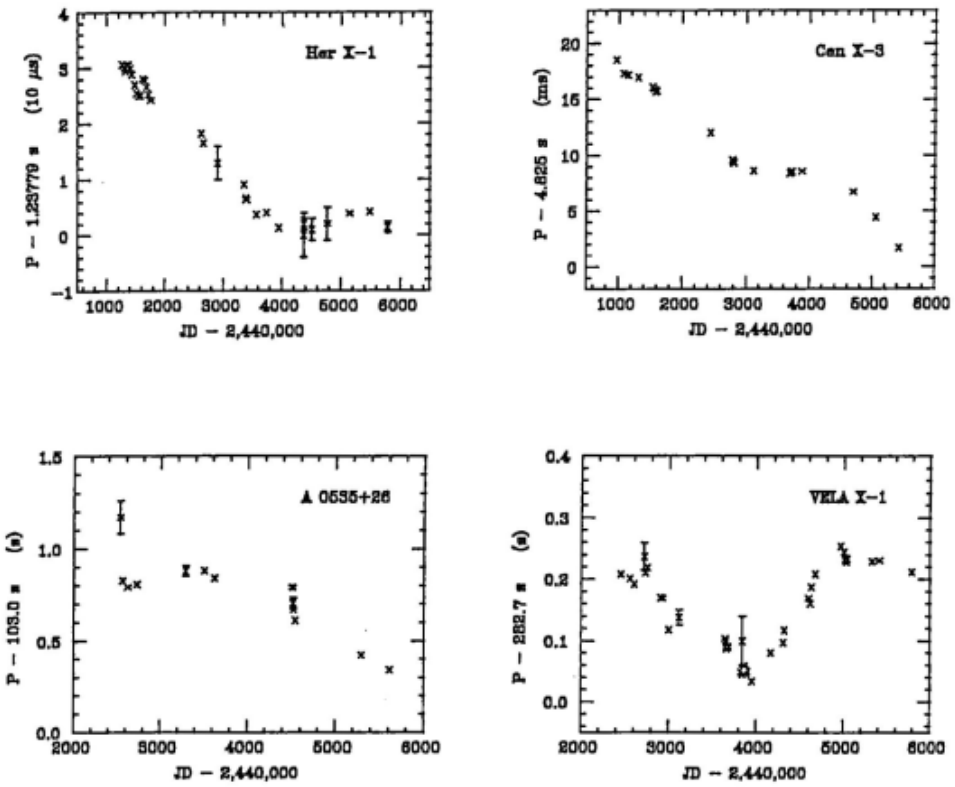

Figure 2.14: Period changes of four X-ray binary pulsars (White et al. 1995).

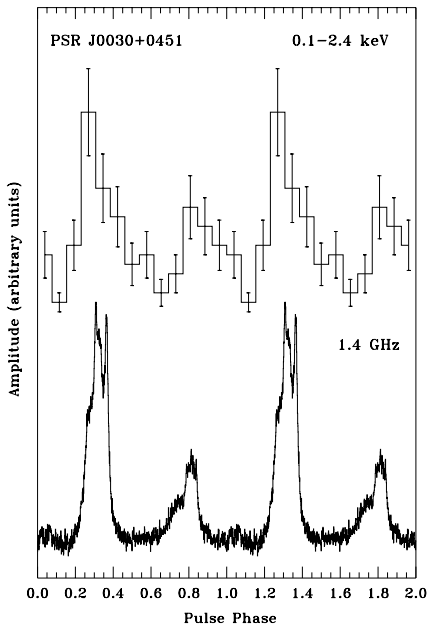

Figure 2.15: X-ray and radio pulse profile of PSR J0030+0451 as observed with the ROSAT PSPC in the 0.1–2.4 keV band (top) and the Arecibo radio telescope at 1.4 MHz (bottom). Two phases cycles are shown for clarity.

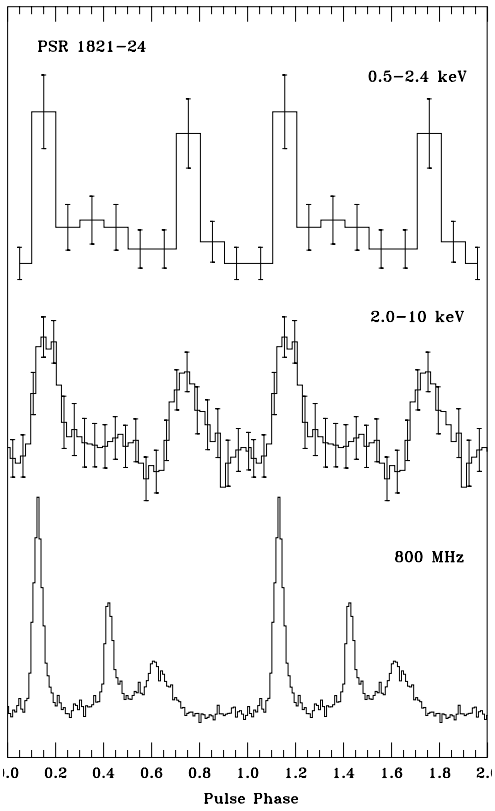

Figure 2.16: Integrated pulse profiles of the globular cluster pulsar PSR 1821−24 as observed with the ROSAT HRI (top), the ASCA GIS detector and with the NRAO at 800 MHz (bottom). Two phase cycles are shown for clarity. The X-ray pulse profiles are characterized by a double peak structure with a phase separation of ~ 0.6 between the two peaks. The radio profile at 800 MHz depicts three pulse components. At this frequency the dominating radio pulse is nearly phase aligned with the primary X-ray pulse.

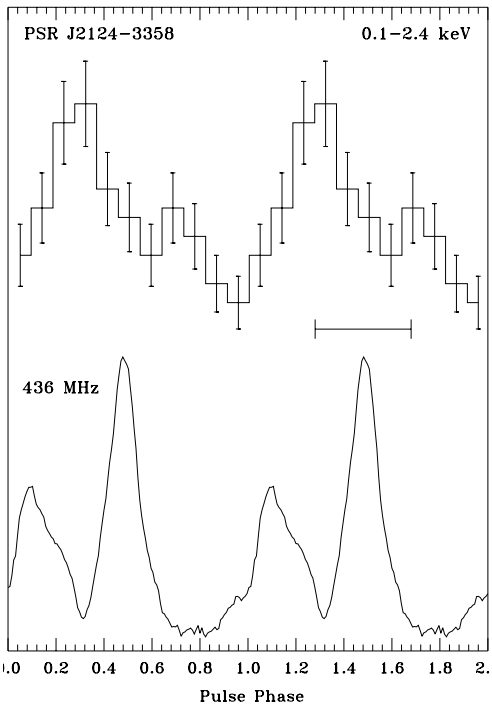

Figure 2.17: Light curves of PSR J2124-3358 as observed with the ROSAT HRI in 0.1−2.4 keV (top) and the Parkes radio telescope at 436 MHz (bottom). Two phase cycles are shown for clarity. Both light curves are characterized by two peaks which are separated by ~ 0.4 rotations.

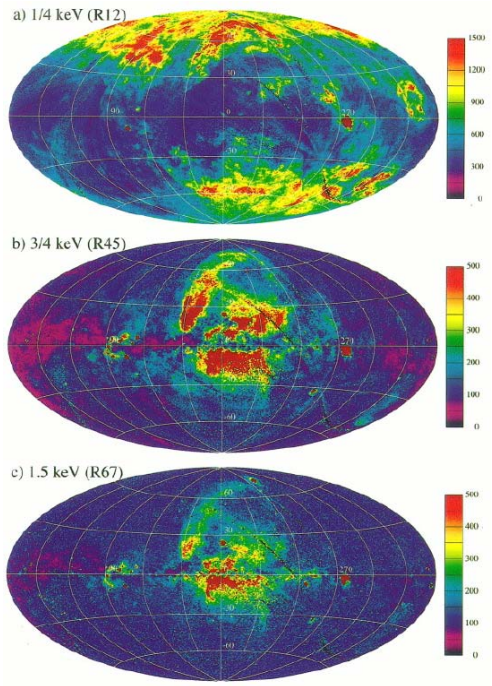

Figure 2.18: ROSAT survey diffuse X-ray background maps. Galactic longitude increasing to the left. The values next to the color bars indicate the intensity and the units are 10^{-6} counts s^{-1} $arcmin^{-2}$. Regions of missing data are black.

Chapter 3

Geometry

This chapter provides an overview of the geometrical aspects of a pulsar-based location system and of how position estimation algorithms and associated performance bounds are obtained. The described algorithms constitute a post-processing scheme of timing estimates (front-end processing) obtained from the received signal and exposed in later chapters, as first described in figure (1.1). Therefore, performance bounds of position estimation are determined by the performance bounds of timing estimation in the previous stage. Timing estimation basically provides differential information between the expected and measured pulse arrival times, which is used to infer a position estimate, as described in figure (3.2). Such measurements are affected by noise, so that a precise characterization of signal and noise statistics is necessary to formulate well-performing algorithms. This approach, based on the Maximum Likelihood (ML) criterion, will be the workhorse of this and following chapters.

The main issues addressed are:

- the achievable position accuracy.
- the achievable accuracy of the (auto-estimated) internal clock.
- the ambiguity problems related with the unknown number of phase-cycles of the pulsar signals.

3.1 Introduction

Pulsar-based location is only possible if pseudo Time-Of-Arrival (p-TOA) estimates[1] from at least two pulsars can be obtained. For the location scales considered, the distance from the spacecraft to the pulsar is so much larger than the travel distance that the angle of arrival of the pulsar signals is practically constant everywhere in the location sphere. This important fact simplifies the location algorithm based on p-TOA measurements and excludes location algorithms based on variations in the angle of arrival.

These algorithms combine N p-TOA measurements (from N pulsars) to obtain a position estimate. In contrast to artificial signals for location, pulsar signals are not modulated and it is not possible to identify the number of phase cycles (pulsar periods) between two positions (see figure (3.2) for clarification). This will produce an ambiguity problem as p-TOA measurements are, indeed, phase evolution measurements: the N p-TOA measurements are N values defined in the interval $[0, 1)$ indicating the exact time in the phase evolution of each pulsar with respect to a reference time. In the signal model subsection, we describe how this ambiguity impacts the location algorithm.

This first feasibility study assumes a simplified constant speed model for the spacecraft over long periods of time. The inclusion of higher position derivatives would refine further the trajectory model, but more complex models are required.

[1] p-TOA measurements are defined as the time of arrival of the pulse with respect to a local timing reference: see figure (3.1)

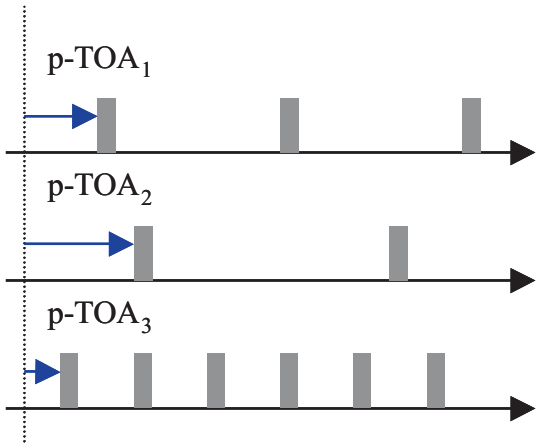

Figure 3.1: Depiction of p-TOA measurements with respect to several pulsars. The vertical line stands for the local time reference.

3.2 Signal Model

In this section, the signal model of the available p-TOA measurements is precisely defined. The data structures are formulated in matrix notation along with the necessary statistical characterization for the derivation of optimum algorithms. It is assumed that Pulse Arrival Time Drift (PATD) measurements may also be available. Using this signal model, it will be possible to obtain closed-form expressions for the location algorithm and its achievable position accuracy, showing that some assumptions on the internal clock are also necessary.

3.2.1 Signal model for phase estimates

It is known that pulsars have incredible stability properties that allow to predict the exact phase evolution of the pulsar signal at any instant in the reference frame of the Solar System Barycenter (SSB) using,

- Some previous estimate of the phase evolution at a reference time T_0
- An estimate of the pulse frequency (PF)
- Its multiples derivatives.

The exact phase evolution is expressed as follows,

$$\Phi_n^{\mathrm{SSB}}(t) = \left[\Phi_n^{\mathrm{SSB}}(T_0) + f_n \cdot (t - T_o) + \sum_{m=2}^{M} \frac{f_n^{(m)} \cdot (t - T_o)^m}{(m)!} \right]_w \tag{3.1}$$

where $\Phi_n^{\mathrm{SSB}}(t)$ is the phase evolution of the n-th pulsar at a generic time t, f_n is the known PF of the n-th pulsar, $f_n^{(m)}$ are its known multiple derivatives and $[\,]_w$ is the phase wrapping operation, defined as,

$$[x]_w = x + m_x \in [0, 1) \tag{3.2}$$

with m_x the integer satisfying the $(\in [0,1))$ condition. This operation guarantees that the obtained measurements are real numbers in the interval $[0, 1)$. It is necessary to consider explicitly the wrapping operation and its associated m_x as the previous timing estimation stage can only resolve time differences within one pulsar period. This fact also becomes evident in figure (3.2), where for distances spanning several pulsar periods, the unwrapped phase is the magnitude directly related to differences in position. In the literature, (3.1) is usually truncated to four or five terms, taking into account that higher order terms only affect over years.

Assuming a phase estimate for each of the N available pulsars, the signal model can be expressed as,

$$\widehat{\Phi}_n^{\mathbf{x}}(t) = \left[\Phi_n^{\mathrm{SSB}}(t-\tau_n) + w_{\Phi_n}\right]_w \tag{3.3}$$

where $\widehat{\Phi}_n^{\mathbf{x}}(t)$ is the phase estimate associated with the n-th pulsar taken at the common and unknown initial time t at the spacecraft (note that the superindex $\mathbf{x}$ is used to remark that that is a spacecraft measurement), τ_n is the phase delay with respect to the SSB and w_{Φ_n} is the additive Gaussian noise sample associated with the estimate $\widehat{\Phi}_n^{\mathbf{x}}(t)$. Phase estimates for each pulsar are generated in front-end processing, and the Gaussian nature of the phase estimation noise is guaranteed over the operating region of the phase estimation algorithms described later in the document. Thus, the algorithms described in this chapter constitute post-filtering of the phase (timing estimates). Noise samples are real (non-complex), independent zero-mean Gaussian random variable with covariance matrix,

$$\mathbf{R}_\Phi = E\left[\mathbf{w}_\Phi \mathbf{w}_\Phi^T\right] = \begin{bmatrix} \sigma_{\Phi_1}^2 & 0 & 0 \\ 0 & \ddots & 0 \\ 0 & 0 & \sigma_{\Phi_N}^2 \end{bmatrix} \tag{3.4}$$

where $\mathbf{w}_\Phi = [w_{\Phi_1}, \cdots, w_{\Phi_N}]^T$. This covariance matrix completely characterizes the noise statistics.

3.2.2 Simplified signal model for phase estimates

This subsection modifies the previous signal model to facilitate the natural formulation of location algorithms. The first natural approach assumes that we have some coarse knowledge of the measurement time t (some ambiguity remains). Assuming that t is close to T_0', we can simplify (3.3) as follows,

$$\widehat{\Phi}_n^{\mathbf{x}}(t) = \left[\Phi_n^{\mathrm{SSB}}(T_0') + f_n \cdot (t - T_o' - \tau_n) + w_{\Phi_n}\right]_w \tag{3.5}$$

where it can be noted that only two terms of the phase evolution (3.1) have been used exploiting the vicinity of t to T_0'. This is not a strong assumption as the rest of terms can only affect after several months. At present, only a very coarse estimation of t is needed. Note also that the reference phase $\Phi_n^{\mathrm{SSB}}(T_0')$ can be obtained precisely using (3.1),

$$\Phi_n^{\mathrm{SSB}}(T_0') = \Phi_n^{\mathrm{SSB}}(T_0) + f_n \cdot (T_0' - T_o) + \sum_{m=1}^{M} \frac{f_n^{(m)} \cdot (T_0' - T_o)^{m+1}}{(m+1)!} \tag{3.6}$$

where all the terms are known.

Now, the specific delay for the n-th phase estimate τ_n shown in (3.5) can be easily related with the position of the spacecraft and the direction of arrival (DOA) for the specific pulsar,

$$\tau_n = \frac{1}{c} \mathbf{u}_n{}^T \mathbf{x} \tag{3.7}$$

where $\mathbf{u}_n$ is the unitary vector in the direction of the pulsar in any Cartesian system (centered in the SSB in our case) and c is the speed of light. This relationship is linear as the angle of arrival from the pulsar is constant everywhere. As can be seen in figure (3.2), the delay with respect to the SSB can be understood as the projection of the position vector $\mathbf{x}$ onto the constant angle of arrival of the pulsar.

For a typical distance of 1 Kpc (Kparsec) between the pulsar and the SSB, the constant angle-of-arrival (AOA) assumption is satisfied as

$$\frac{\|x\|}{1\mathrm{Kpc}} << 1 \Rightarrow \|x\| < \frac{1\mathrm{Kpc}}{100} \approx 3 \cdot 10^{17}\mathrm{m} \tag{3.8}$$

Let us now to define the final signal model for the p-TOA measurements. Taking (3.5) and (3.7), we have,

$$\widehat{\Phi}_n^{\mathbf{x}}(t) = \left[\Phi_n^{\mathrm{SSB}}(T_0') + f_n \cdot \left(t - T_o' - \frac{1}{c}\mathbf{u}_n{}^T \mathbf{x}\right) + w_{\Phi_n}\right]_w \tag{3.9}$$

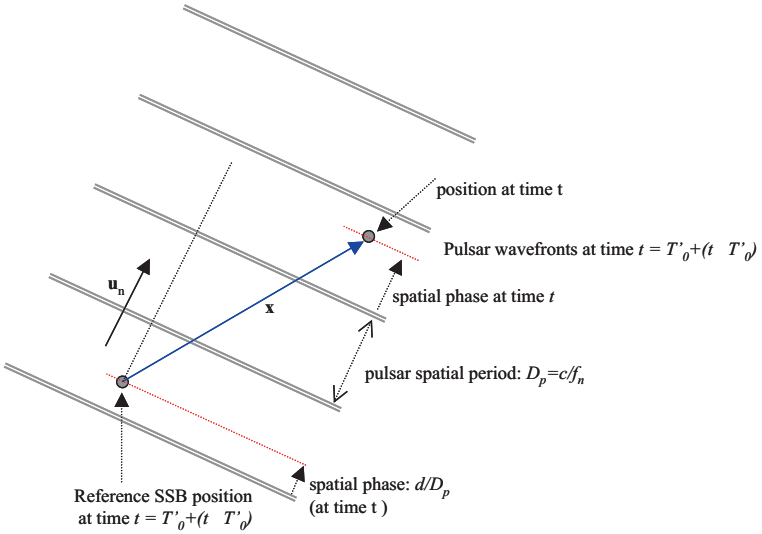

Figure 3.2: Geometrical interpretation of the phase estimate corresponding to time $t = T_0' + (t - T_0')$ as a snapshot depicting the pulsar wavefronts as reference. The correction with respect to the reference position is represented by $\mathbf{x}$. The source of ambiguity is observed as an integer number of spatial pulsar periods D_p in the direction $\mathbf{u}_n$ of the pulsar.

and exploiting the definition of the wrapping operation (3.2),

$$\widehat{\Phi}_n^{\mathbf{x}}(t) = \Phi_n^{\mathrm{SSB}}(T_0') + f_n \cdot \left(t - T_o' - \frac{1}{c} \mathbf{u}_n{}^T \mathbf{x} \right) + m_n + w_{\Phi_n} \tag{3.10}$$

where m_n is an unknown integer related with the number of wrapped phase cycles for each pulsar signal. Now, rearranging terms we can find the following transformation of measurements,

$$\lambda_n = f_n^{-1} \left(\widehat{\Phi}_n^{\mathbf{x}}(t) - \Phi_n^{\mathrm{SSB}}(T_0') \right) + T_o' = t - \frac{1}{c} \mathbf{u}_n{}^T \mathbf{x} + f_n^{-1} m_n + f_n^{-1} w_n \tag{3.11}$$

where λ_n are the linear transformed initial phase delays. Basically, this last transformation tries to generalize the relationship between the p-TOA measurements and the unknown parameters: time, position and ambiguity.

In this last expression, it can be seen that the new transformed measurements have a completely linear relationship with the unknown parameters and are still corrupted with Gaussian noise. This can be expressed in vector notation as follows:

$$\begin{bmatrix} \lambda_1 \\ \vdots \\ \lambda_N \end{bmatrix} = \begin{bmatrix} \mathbf{1}_N & \begin{bmatrix} \frac{-1}{c} u_1^T \\ \vdots \\ \frac{-1}{c} u_N^T \end{bmatrix} \end{bmatrix} \cdot \begin{bmatrix} t \\ \mathbf{x} \end{bmatrix} + \begin{bmatrix} f_1^{-1} & 0 & 0 \\ 0 & \ddots & 0 \\ 0 & 0 & f_N^{-1} \end{bmatrix} \cdot \begin{bmatrix} m_1 \\ \vdots \\ m_N \end{bmatrix} + \begin{bmatrix} f_1^{-1} & 0 & 0 \\ 0 & \ddots & 0 \\ 0 & 0 & f_N^{-1} \end{bmatrix} \cdot \begin{bmatrix} w_{\Phi_1} \\ \vdots \\ w_{\Phi_N} \end{bmatrix} \tag{3.12}$$

$$\lambda = \begin{bmatrix} \mathbf{1}_N & -\mathbf{U} \end{bmatrix} \cdot \begin{bmatrix} t \\ \mathbf{x} \end{bmatrix} + \mathbf{F} \cdot \begin{bmatrix} m_1 \\ \vdots \\ m_N \end{bmatrix} + \mathbf{F} \cdot \begin{bmatrix} w_{\Phi_1} \\ \vdots \\ w_{\Phi_N} \end{bmatrix} \tag{3.13}$$

where $\mathbf{U}$ and $\mathbf{F}$ are defined in the trivial way as,

$$\mathbf{U} = \begin{bmatrix} \frac{1}{c} u_1^T \\ \vdots \\ \frac{1}{c} u_N^T \end{bmatrix} \tag{3.14}$$

$$\mathbf{F} = \begin{bmatrix} f_1^{-1} & 0 & 0 \\ 0 & \ddots & 0 \\ 0 & 0 & f_N^{-1} \end{bmatrix} \tag{3.15}$$

Finally, we can redefine the noise terms as:

$$\mathbf{w}_\lambda = \mathbf{F} \cdot \begin{bmatrix} w_{\Phi_1} \\ \vdots \\ w_{\Phi_N} \end{bmatrix} \tag{3.16}$$

It is easy to note that $\mathbf{w}_\lambda$ is a zero-mean random Gaussian vector with the following covariance matrix,

$$\mathbf{R}_\lambda = E\big[\mathbf{w}_\lambda \cdot \mathbf{w}_\lambda{}^T\big] = \mathbf{F}\mathbf{R}_\Phi\mathbf{F}^T = \begin{bmatrix} f_1^{-2}\sigma_{\Phi_1}^2 & 0 & 0 \\ 0 & \ddots & 0 \\ 0 & 0 & f_N^{-2}\sigma_{\Phi_N}^2 \end{bmatrix} = \begin{bmatrix} \sigma_{\lambda_1}^2 & 0 & 0 \\ 0 & \ddots & 0 \\ 0 & 0 & \sigma_{\lambda_N}^2 \end{bmatrix} \tag{3.17}$$

where $\sigma_{\lambda_n}^2 = f_n^{-2}\sigma_{\Phi_n}^2$
So, the final model for the modified phase estimates is:

$$\lambda = \begin{bmatrix} \mathbf{1}_N & -\mathbf{U} \end{bmatrix} \cdot \begin{bmatrix} t \\ \mathbf{x} \end{bmatrix} + \mathbf{F} \cdot \mathbf{m} + \mathbf{w}_\lambda \tag{3.18}$$

It may seem strange to model the internal time t as an unknown when in practical applications the internal clock will have very stable properties, even in long journeys. It will be seen in the ambiguity section, that modeling the clock as an unknown simplifies the ambiguity resolution problem.

3.2.3 Signal model for PATD estimates

It is shown in this report that Pulse Arrival Time Drift (PATD) estimates from pulsars can also be obtained. This will be exploited in the constant speed model as the estimated PATD are linearly related with the speed of the spacecraft. Additionally, PATD estimates may also be used for ambiguity resolution. The general signal model for PATD estimates is expressed as follows,

$$\gamma_n = \frac{1}{c}\mathbf{u}_n^T \cdot \mathbf{s} + w_{\gamma_n} \tag{3.19}$$

where $\mathbf{s}$ is the speed of the spacecraft and w_{γ_n} is the zero-mean Gaussian noise associated with this PATD estimate. This noise term is considered component-wise independent. Hence, its covariance matrix becomes,

$$\mathbf{R}_\gamma = E\big[\mathbf{w}_\gamma \mathbf{w}_\gamma{}^T\big] = \begin{bmatrix} \sigma_{\gamma_1}^2 & 0 & 0 \\ 0 & \ddots & 0 \\ 0 & 0 & \sigma_{\gamma_N}^2 \end{bmatrix} \tag{3.20}$$

where $\mathbf{w}_\gamma = [w_{\gamma_1}, \cdots, w_{\gamma_N}]^T$. So, if the N PATD estimates are collectred into one vector, we get,

$$\gamma = \mathbf{U} \cdot \mathbf{s} + \mathbf{w}_\gamma \tag{3.21}$$

where $\mathbf{U}$ was defined in (3.14).

3.2.4 General signal model

The previous signal model sections were devoted to showing the relationship between the available measurements (p-TOAs estimates and PATDs) and the parameter of interest. This section generalizes the previous signal models for the case of more than a single observation window.

Let us assume that L consecutive observation windows are used to estimate L p-TOAs and PATDs for each of the N available pulsars. This means that $N \cdot L$ p-TOA and PATD estimates are available. Using (3.18), the l-th set of p-TOA estimates can be expressed as,

$$\lambda_{(l)} = \begin{bmatrix} \mathbf{1}_N & -\mathbf{U} \end{bmatrix} \cdot \begin{bmatrix} t \\ \mathbf{x} + l \cdot \mathbf{s} \end{bmatrix} + \mathbf{F} \cdot \mathbf{m} + \mathbf{w}_{\lambda_{(l)}} \tag{3.22}$$

where the term $\mathbf{x} + l \cdot \mathbf{s}$ indicates that the position of the spacecraft in the l-th observation window will be the position at the last observation window linearly offset with the speed of the spacecraft. Finally, if we define a new modified p-TOAs vector as the stacked version of all the L estimated set of p-TOAs as,

$$\widetilde{\lambda} = \left[\lambda_{(1)}^T, \cdots, \lambda_{(L)}^T\right]^T \tag{3.23}$$

and the stacked version of the noise samples as,

$$\mathbf{w}_{\widetilde{\lambda}} = \left[\mathbf{w}_{\lambda_{(\mathbf{1})}}{}^T, \cdots, \mathbf{w}_{\lambda_{(\mathbf{L})}}{}^T\right]^T \tag{3.24}$$

then, we can define the general signal model for p-TOAs estimates as follows,

$$\widetilde{\lambda} = \begin{bmatrix} \mathbf{1}_N & -\mathbf{U} & \mathbf{0} \\ \mathbf{1}_N & -\mathbf{U} & -\mathbf{U} \\ \mathbf{1}_N & -\mathbf{U} & -2\mathbf{U} \\ \vdots & \vdots & \vdots \\ \mathbf{1}_N & -\mathbf{U} & -(L-1)\mathbf{U} \end{bmatrix} \cdot \begin{bmatrix} t \\ \mathbf{x} \\ \mathbf{s} \end{bmatrix} + \widetilde{\mathbf{F}} \cdot \mathbf{m} + \mathbf{w}_{\widetilde{\lambda}} = \mathbf{A}_\lambda \cdot \begin{bmatrix} t \\ \mathbf{x} \\ \mathbf{s} \end{bmatrix} + \widetilde{\mathbf{F}} \cdot \mathbf{m} + \mathbf{w}_{\widetilde{\lambda}} \tag{3.25}$$

where

$$\widetilde{\mathbf{F}} = \left[\mathbf{F}^T, \cdots, \mathbf{F}^T\right]^T \tag{3.26}$$

As far as neither PATD estimates nor the time offset t are sensitive to distance, it is not difficult to generalize from (3.21) the expression for the L set of PATD estimates, including zero matrices at the necessary positions,

$$\widetilde{\gamma} = \begin{bmatrix} \mathbf{0}_N & \mathbf{0}_{P,P} & \mathbf{U} \\ \vdots & \vdots & \vdots \\ \mathbf{0}_N & \mathbf{0}_{P,P} & \mathbf{U} \end{bmatrix} \cdot \begin{bmatrix} t \\ \mathbf{x} \\ \mathbf{s} \end{bmatrix} + \mathbf{w}_{\widetilde{\gamma}} = \mathbf{A}_\gamma \cdot \begin{bmatrix} t \\ \mathbf{x} \\ \mathbf{s} \end{bmatrix} + \mathbf{w}_{\widetilde{\gamma}} \tag{3.27}$$

where $\widetilde{\gamma}$ and $\mathbf{w}_{\widetilde{\gamma}}$ are defined in the same way as $\widetilde{\lambda}$ and $\mathbf{w}_{\widetilde{\lambda}}$,

$$\widetilde{\gamma} = \left[\gamma_{(1)}^T, \cdots, \gamma_{(L)}^T\right]^T \tag{3.28}$$

$$\mathbf{w}_{\widetilde{\gamma}} = \left[\mathbf{w}_{\gamma_{(\mathbf{1})}}{}^T, \cdots, \mathbf{w}_{\gamma_{(\mathbf{L})}}{}^T\right]^T \tag{3.29}$$

with $\gamma_{(l)}$ and $\mathbf{w}_{\gamma_{(l)}}$ the vectors containing the N PATD estimates and their associated noise terms for the l-th observation window. Finally, the covariance matrices of the stacked noise sample vectors can be defined as,

$$\mathbf{R}_{\widetilde{\lambda}} = E\left[\mathbf{w}_{\widetilde{\lambda}} \mathbf{w}_{\widetilde{\lambda}}{}^T\right] = \begin{bmatrix} \mathbf{R}_{\widetilde{\lambda}_{(1)}} & 0 & 0 \\ 0 & \ddots & 0 \\ 0 & 0 & \mathbf{R}_{\widetilde{\lambda}_{(L)}} \end{bmatrix} \tag{3.30}$$

$$\mathbf{R}_{\tilde{\gamma}} = E\left[\mathbf{w}_{\tilde{\gamma}}\mathbf{w}_{\tilde{\gamma}}{}^{T}\right] = \begin{bmatrix} \mathbf{R}_{\tilde{\gamma}_{(1)}} & 0 & 0 \\ 0 & \ddots & 0 \\ 0 & 0 & \mathbf{R}_{\tilde{\gamma}_{(L)}} \end{bmatrix} \tag{3.31}$$

3.3 Location algorithm without ambiguity

This section presents the location algorithms and their performance assuming that there is no ambiguity problem, that is, vector $\mathbf{m}$ in (3.18) and (3.25) is known. The following section will focus on some key points of the ambiguity problem. Two cases are considered in this section: single and multiple observation windows. The former is the simplest algorithm that transforms N p-TOAs into a position estimate in the optimal way. The latter exploits several correlative observation windows using the constant speed model.

3.3.1 Single observation window

In this case, only N p-TOA measurements are available for the location algorithm. Assuming that $\mathbf{m}$ is known ($\mathbf{m}_0$ is the true value), the signal model shown in (3.18) can be rewritten as,

$$\lambda - \mathbf{F}\cdot\mathbf{m}_0 = \begin{bmatrix} \mathbf{1}_N & -\mathbf{U} \end{bmatrix} \cdot \begin{bmatrix} t \\ \mathbf{x} \end{bmatrix} + \mathbf{w}_\lambda \tag{3.32}$$

where all parameters except the position of the spacecraft and, in general, the time offset, are known. In a practical implementation, the internal clock will be provided by some stable hardware clock: the precision of the internal clock is enough to assume that t is known. However, as seen in the ambiguity section, it is also interesting to obtain the performance assuming that the clock is unknown.

To get an idea of the achievable accuracy of the location algorithms, we compute the Maximum Likelihood (ML) estimation of the position and its corresponding covariance matrix. This provides the asymptotic theoretical limit of the accuracy, or Cramer-Rao Bound (CRB).

Basics of ML estimation for the linear signal model

We introduce briefly some basics on (unconstrained) ML estimation for the linear signal model to be particularized later to position estimation. Let us assume the following measurement equation,

$$\mathbf{x} = \mathbf{A}\mathbf{h} + \mathbf{n}$$

with $\mathbf{x}$ the measurement vector, $\mathbf{A}$ the matrix characterizing the structure of the data, $\mathbf{h}$ the parameter vector to estimate and $\mathbf{n}$ the noise vector. If the noise is Gaussian, complex and zero-mean, with covariance matrix $\mathbf{R}_n$, the probability density function (pdf) of $\mathbf{x}$ is expressed as,

$$p(\mathbf{x}|\mathbf{h}) = \frac{1}{\pi^N \det\mathbf{R}_n} e^{-(\mathbf{x}-\mathbf{A}\mathbf{h})^{\mathrm{H}}\mathbf{R}_n^{-1}(\mathbf{x}-\mathbf{A}\mathbf{h})}$$

with $\mathbf{R}_n$ the covariance matrix of the zero-mean Gaussian noise vector $\mathbf{n}$: $\mathbf{R}_n = E\{\mathbf{n}\mathbf{n}^{\mathrm{H}}\}$, with the superscript ^{H} denoting the Hermitian (conjugate transpose) operator. Although in our case, the data vector $\mathbf{x}$ is real, the estimation equation to be obtained will also be applicable (the corresponding pdf for real data should be used). The ML estimate of $\mathbf{h}$, $\hat{\mathbf{h}}$, is obtained maximizing equation (3.3.1) with respect to the unknown (unconstrained) parameter. Hence, the exponent is to be minimized and,

$$\hat{\mathbf{h}} = \left(\mathbf{A}^{\mathrm{H}}\mathbf{R}_n^{-1}\mathbf{A}\right)^{-1}\mathbf{A}^{\mathrm{H}}\mathbf{R}_n^{-1}\mathbf{x}$$

This is an unbiased estimator, $E\{\hat{\mathbf{h}}\} = \mathbf{h}$, with error covariance matrix,

$$\begin{aligned} \mathbf{R}_e &= E\{(\hat{\mathbf{h}}-\mathbf{h})(\hat{\mathbf{h}}-\mathbf{h})^{\mathrm{H}}\} \\ &= \left(\mathbf{A}^{\mathrm{H}}\mathbf{R}_n^{-1}\mathbf{A}\right)^{-1} \end{aligned} \tag{3.33}$$

ML estimation of the position vector

As far as the relationship between the measurements and the parameter of interest shown in (3.32) is linear, the ML estimation of the parameters ($\mathbf{x}$ and t) and the associated covariance matrix has a closed-form expression,

$$\widehat{\widetilde{\mathbf{x}}} = \left[\mathbf{A}^T\mathbf{R}_\lambda^{-1}\mathbf{A}\right]^{-1}\mathbf{A}^T\mathbf{R}_\lambda^{-1}\left(\lambda - \mathbf{f}^{-1} \odot \mathbf{m}_0\right) \tag{3.34}$$

$$\mathbf{R}_{\widehat{\widetilde{\mathbf{x}}}} = \left[\mathbf{A}^T\mathbf{R}_\lambda^{-1}\mathbf{A}\right]^{-1} \tag{3.35}$$

where the definition of $\widetilde{\mathbf{x}}$ and $\mathbf{A}$ depends on the assumption about t. If t is considered unknown,

$$\widetilde{\mathbf{x}} = \left[t, \mathbf{x}^T\right]^T \qquad \mathbf{A} = \begin{bmatrix} \mathbf{1}_N & -\mathbf{U} \end{bmatrix} \tag{3.36}$$

and if the internal clock t is considered known,

$$\widetilde{\mathbf{x}} = \mathbf{x} \qquad \mathbf{A} = [-\mathbf{U}] \tag{3.37}$$

Matrix $\mathbf{R}_{\widehat{\widetilde{\mathbf{x}}}}$ shows in their diagonal elements the variance for all estimated parameters. These are, the unknown instant of time t and the position of the spacecraft $\mathbf{x}$ if t is considered unknown or just the position of the spacecraft if the internal clock is assumed known. In the following two subsections, we will show the exact closed-form expressions of the accuracy (time and position) for both cases: known time t and unknown time t.

Known internal clock

As will be seen in the ambiguity resolution section, this expression is used to evaluate the final position algorithm in the case that the ambiguity has been solved. As far as $\mathbf{R}_{\widehat{\widetilde{\mathbf{x}}}}$ only includes the position estimation variance, the performance can be obtained as follows,

$$\mathbf{R}_{\mathbf{x}} = \mathbf{R}_{\widehat{\widetilde{\mathbf{x}}}} \qquad \sigma_x^2 \approx \mathrm{tr}[\mathbf{R}_{\mathbf{x}}] = \mathrm{tr}\left[\sum_n \sigma_{\lambda_n}^{-2}\mathbf{u}_n{\mathbf{u}_n}^T\right]^{-1} \tag{3.38}$$

To simplify, let us assume that all involved pulsars have similar timing variances ($\overline{\sigma}_\lambda^2$). Under this assumption, the expected position accuracy can be expressed as,

$$\sigma_x^2 \approx \mathrm{tr}[\mathbf{R}_{\mathbf{x}}] = \overline{\sigma}_\lambda^2 \ \ \mathrm{tr}\left[\left[\sum_n \mathbf{u}_n{\mathbf{u}_n}^T\right]^{-1}\right] \tag{3.39}$$

and finally, assuming a uniformly distribution of pulsars (optimistic assumption), the expression is simplified to,

$$\sigma_x^2 \approx \mathrm{tr}[\mathbf{R}_{\mathbf{x}}] = \overline{\sigma}_\lambda^2 c^2 \frac{P}{N} \tag{3.40}$$

where P is the dimension problem, two for 2D location and 3 for 3D location. Obviously, this expression is only presented to have a coarse idea of performance. In the simulations, only (3.38) will be used.

Unknown internal clock

As the ambiguity resolution section will show, this assumption is used to solve the major part of the ambiguity problem. The trick here is to estimate also the internal clock with the incoming p-TOA measurements in order to compare with the real internal clock provided by the hardware. This will allow to discard a large part of the ambiguity points produced by the unknown number of phase cycles. Achieving this goal is extremely important to computing the achievable accuracy for the internal clock (in seconds) and for the spacecraft position (in meters).

Taking into account that the term $\mathbf{R}_{\widehat{\widetilde{\mathbf{x}}}}$ includes the accuracy of the clock and the position, both terms can be computed as follows,

$$\mathbf{R}_{\mathbf{x}} = \mathbf{T}_{\mathbf{x}}{}^{T}\mathbf{R}_{\widehat{\widetilde{\mathbf{x}}}}\mathbf{T}_{\mathbf{x}} \tag{3.41}$$

$$\sigma_t^2 = \mathbf{T}_t{}^{T}\mathbf{R}_{\widehat{\widetilde{\mathbf{x}}}}\mathbf{T}_t \tag{3.42}$$

where $\mathbf{T}_{\mathbf{x}} = [\mathbf{0}_{2,1}, \mathbf{I}_{2,2}]^T$ and $\mathbf{T}_t = [1,0,0]^T$. To compare what the effect is of assuming an unknown internal clock, it can be shown after non-trivial algebraic manipulations, that this term can be also expressed as,

$$\mathbf{R}_{\mathbf{x}}^{-1} = \left[\sum_n \sigma_{\lambda_n}^{-2}\mathbf{u}_n\mathbf{u}_n{}^{T}\right] - \left[\sum_n \sigma_{\lambda_n}^{-2}\right]^{-1}\left[\sum_n\sum_{n'} \sigma_{\lambda_n}^{-2}\sigma_{\lambda_{n'}}^{-2}\,\mathbf{u}_n\mathbf{u}_{n'}{}^{T}\right] \tag{3.43}$$

Again, as in the previous subsection , let us assume that similar variance are obtained for all pulsars,

$$\mathbf{R}_{\mathbf{x}} \approx \overline{\sigma}_{\lambda}\left[\sum_n \mathbf{u}_n\mathbf{u}_n{}^{T} - \sum_n\sum_{n'} \mathbf{u}_n\mathbf{u}_{n'}{}^{T}\right]^{-1} \tag{3.44}$$

and a final expression of the position error is given by,

$$\sigma_x^2 \approx \mathrm{tr}[\mathbf{R}_{\mathbf{x}}] = \overline{\sigma}_{\lambda}\ \ \mathrm{tr}\left[\left[\sum_n \mathbf{u}_n\mathbf{u}_n{}^{T} - \sum_n\sum_{n'} \mathbf{u}_n\mathbf{u}_{n'}{}^{T}\right]^{-1}\right] \tag{3.45}$$

This last expression of the mean position error tends to the following closed-form expressions if the available pulsars are uniformly distributed in all possible directions,

$$\sigma_x^2 \approx \overline{\sigma}_{\lambda}^2 \cdot c^2 \frac{P}{N-1} \tag{3.46}$$

where again P is the dimension problem, two for 2D location and 3 for 3D location.

3.3.2 Multiple observation windows

This section is provided to get an idea of the achievable accuracy when more than one correlative observation window is used. This will be necessary when the available time to estimate the position is large enough to invalidate the natural static assumption considered in the p-TOAs estimate.

Assuming that we have L phase and PATD estimates for each one of the N available pulsars, the general model shown in (3.25) and (3.27) can be rewritten taking into account that now, $\mathbf{m} = \mathbf{m}_0$ is known,

$$\begin{bmatrix} \widetilde{\lambda} \\ \widetilde{\gamma} \end{bmatrix} - \begin{bmatrix} \widetilde{\mathbf{F}} \\ \mathbf{0} \end{bmatrix} \cdot \mathbf{m}_0 = \begin{bmatrix} \mathbf{A}_{\lambda} \\ \mathbf{A}_{\gamma} \end{bmatrix} \cdot \begin{bmatrix} t \\ \mathbf{x} \\ \mathbf{s} \end{bmatrix} + \begin{bmatrix} \mathbf{w}_{\widetilde{\lambda}} \\ \mathbf{w}_{\widetilde{\gamma}} \end{bmatrix} \tag{3.47}$$

As in the single observation window case, it can be considered that the internal clock is known or not. This will be clearly explained in the ambiguity resolution section. In the following (simplified) development no special emphasis will be given to this point. To consider the case with known internal clock, we only have to remove this parameter to the unknowns vector and modify accordingly the definition of matrix $\mathbf{A}$

Let us assume the general case where $\widetilde{\mathbf{x}}$, the unknowns vector, $\mathbf{A}$, the model matrix, and $\mathbf{T}_{\mathbf{x}}$ are defined as,

$$\widetilde{\mathbf{x}} = \begin{bmatrix} t \\ \mathbf{x} \\ \mathbf{s} \end{bmatrix} \tag{3.48}$$

$$\mathbf{A} = \begin{bmatrix} \mathbf{A}_{\lambda} \\ \mathbf{A}_{\gamma} \end{bmatrix} \tag{3.49}$$

$$\mathbf{T}_{\mathbf{x}} = [\mathbf{0}_{2,1}, \mathbf{I}_{2,2}, \mathbf{0}_{2,2}]^T \tag{3.50}$$

As far as the signal model presented in (3.47) has the same terms than in the single observation window, the same expressions can be used. The final expression of the position accuracy is then,

$$\mathbf{R}_{\widehat{\widetilde{\mathbf{x}}}} = \left[\mathbf{A}^T \begin{bmatrix} \mathbf{R}_{\widetilde{\lambda}}^{-1} & \mathbf{0} \\ \mathbf{0} & \mathbf{R}_{\widetilde{\gamma}}^{-1} \end{bmatrix} \mathbf{A}\right]^{-1} = \left[{\mathbf{A}_\lambda}^T \mathbf{R}_{\widetilde{\lambda}}^{-1} \mathbf{A}_\lambda + {\mathbf{A}_\gamma}^T \mathbf{R}_{\widetilde{\gamma}}^{-1} \mathbf{A}_\gamma\right]^{-1} \tag{3.51}$$

and finally, the position accuracy is obtained as,

$$\mathbf{R}_{\mathbf{x}} = {\mathbf{T}_{\mathbf{x}}}^T \mathbf{R}_{\widehat{\widetilde{\mathbf{x}}}} \mathbf{T}_{\mathbf{x}} \tag{3.52}$$

Although this expression is quite simple, the result is very useful. The diagonal elements of matrix $\mathbf{R}_{\widehat{\widetilde{\mathbf{x}}}}$ show the accuracy obtained in the estimation of position, speed and time-offset. The first two elements provide us with the achievable accuracy for spacecraft navigation. The last term provides information on the capability of the system is able to estimate the time-offset. If this estimation is good enough, the system will be able to estimate the difference between the local internal clock and the pulsar-based estimated clock. This will allow to correct the internal atomic clock with a more precise source: the pulsars. In the simulation section, results of the auto-estimation of the on-board clock is also presented for this interesting feature of pulsar-based location.

3.4 Ambiguity resolution

The ambiguity resolution problem will be, by far, one of the most important points in the geometrical considerations of this study. In general, it can be considered one important point to solve since no modulation or additional information is obtained from the pulsars. The ambiguity resolution algorithm has to be capable of estimating the vector $\mathbf{m}$ in (3.18) and (3.25) in order to apply the algorithms presented in the previous section.

In the first subsection, the main ideas for ambiguity resolution will be presented. In the following subsections, the signal model needed to formulate the ambiguity resolution will be also presented and some closed-form expressions for the ambiguity probability will be derived. Finally, some issues about implementation complexity will be addressed. Most of the mathematical developments related with ambiguity resolution have been included in the appendix to this chapter. At this stage, only descriptive arguments are provided.

3.4.1 Methods for the ambiguity resolution

The ambiguity problem presented in the pulsar-based location algorithm appears as no a-priori knowledge of the phase-cycle number for each pulsar is available. This is mathematically expressed by the unknown integer vector presented is the general formulation in (3.18) and (3.25).

In this document, two ways to estimate $\mathbf{m}$ will be introduced: the former limits the number of possible values for $\mathbf{m}$ assuming that there is a priori coarse knowledge of the spacecraft position and a good estimation of the internal clock; the latter uses additional pulsars to geometrically solve some remaining ambiguity points (few values for the integer vector $\mathbf{m}$).

Previous knowledge of position and time

In general, it can be assumed that there is a previous coarse knowledge of the spacecraft position. In the worst case, it will be the entire possible positions assuming the maximum speed of the spacecraft, but in general better previous position estimation may be assumed. Additionally, the internal clock of the spacecraft can be considered stable enough to be a valid reference.

Let us assume that the previous knowledge of the spacecraft position is a sphere of radius R meters. It is not difficult to count the possible values for each component of $\mathbf{m}$. This number is related to the number of times the period of the pulsar-signal (translated to meters) fits in the coarse position estimation (of radius R). Once we have this set of possible values for $\mathbf{m}$, we can formulate the position estimation algorithm in each of the possible values for $\mathbf{m}$.

It is important to note that if we assume that the internal clock is known, only three pulsars will be needed to compute a valid 3D spacecraft position and better accuracies are obtained (with respect to assuming t unknown) but it will be really hard to decide which value of $\mathbf{m}$ is the correct one.

The trick here consists of processing one more pulsar and assuming that the internal clock is unknown. Simulation results show that the major part of possible values of $\mathbf{m}$ produce estimates of the internal clock t very different from its current value. Then all the values of $\mathbf{m}$ that yield a time estimate far from the current internal clock (hardware) will be discarded. In general the rule can be mathematically expressed as,

$$\left\| \widehat{t} - t \right\| > \Upsilon \left(\sigma_t \right) \tag{3.53}$$

where $\widehat{t}$ is the estimated time and σ_t is its associated variance, both obtained using the closed-form expressions presented in the previous section. Υ is a threshold parameter that can take values of 4,5,6,etc.

This technique can eliminate a great number of possible values of $\mathbf{m}$, called ambiguity points. It is important to note that this technique can be applied with 4 or more pulsars (for 3D location). It is important to note also that as far as the initial coarse location increases, so does the number of possible values for $\mathbf{m}$. Then, this technique possibly fails. In this case the second technique presented in this document has to be applied.

This first technique is by far, the simplest and most robust technique and it will be applied to reduce the possibly huge number of ambiguity points to only a few. The simulations section shows how it works for several initial coarse locations.

ML function for each possible point

If the first technique is not able to remove all the possible values for $\mathbf{m}$ (except for the correct one), the problem of deciding which of a set of M possible values for $\mathbf{m}$ is the most likely should be addressed. The only way to do this is to evaluate the maximum likelihood function at each of these points. Obviously the use of additional pulsars will facilitate the task. For instance, it can be proved that it is not possible to discard one ambiguity point (a value for $\mathbf{m}$ not discarded with the first technique) if only four pulsars are used. It means that if the first technique fails, a minimum of five pulsars have to be processed.

Appendix A shows the development needed to evaluate the fail-probability of ambiguity resolution. This development basically shows the probability that the ML function evaluated at an incorrect point would be larger than the ML function evaluated at the correct point. The results shown in this appendix are a good reference to evaluating the necessity of processing additional pulsars.

3.4.2 Implementation issues

This subsection summarizes the complexity related with the ambiguity resolution problem and some key points in implementation. First of all, the ambiguity resolution problem is clearly related with the initial coarse estimation of the spacecraft position and the initial uncertainty of the on-board clock. Both are critical parameters in the evaluation of the ambiguity resolution complexity. At the end of this section, an expression of complexity will be given in terms of position and clock ambiguity.

Complexity analysis

In general, the ambiguity resolution problem consists of solving which of the possible integer values $\mathbf{m}$ in (3.60) is the correct value. Basically, as explained in previous sections, this is related with the unknown integer number of phase-cycles associated with each pulsar. Let us assume that the mobile can lie in a spherical volume of radius R meters. Let us also assume that the internal clock has a maximum deviation of $\triangle t$ seconds (this is the maximum deviation of the clock in the whole trip). Depending on the unknown exact position of the spacecraft and the exact value of the internal on-board clock, the integer included in $\mathbf{m}$ can take different values. The number of possible values is related with R and $\triangle t$ as follows,

$$p = \left\lceil \frac{R/c + \triangle t}{T} \right\rceil \tag{3.54}$$

where T is the period of the pulsar and $\lceil\ \rceil$ is the upper-integer operation. It is clear from this expression that large-period pulsars will be better to resolve ambiguity with less complexity.

Assuming that the number of possible values is similar for all used pulsars ($\overline{p}$), it seems from (3.60) that, as far as the dimension of $\mathbf{m}$ is N (the number of used pulsars) the complexity of the ambiguity resolution may rise exponentially with the number used pulsars N as,

$$O \propto p^N \tag{3.55}$$

Fortunately, the complexity of the ambiguity resolution algorithm can be drastically reduced with the following reasoning:

1. Let us assume that we want to find the position of the spacecraft in a P-dimensional space (normally P is considered 2 or 3).

2. If we first generate the possible ambiguity points using only $P+1$ pulsars, we will get a set of $p^{(P+1)}$ points.

3. Under each one of the $p^{(P+1)}$ hypothesis (to assume that this point is correct), we can compute the position (with this first $P+1$ pulsars with a certain accuracy (normally really smaller than the initial coarse location) following expression (3.42) or (3.42).

4. Now, the rest of pulsars used to improve accuracy and ambiguity resolution, only add a few ambiguity points due to the fact that for each hypothesis they include the following number of points

$$p_{\sigma_x} = \left\lceil \frac{\sigma_x}{c \cdot T} \right\rceil \tag{3.56}$$

   where σ_x is the accuracy obtained with the first $P+1$ pulsars. Obviously, the number of ambiguity points included with these additional pulsars is clearly lower that the original one.

In conclusion, the complexity associated with the ambiguity resolution can be expressed as follows,

$$O \propto \left(\left\lceil \frac{R/c + \triangle t}{T} \right\rceil \right)^{(P+1)} \cdot \left(\left\lceil \frac{\sigma_x}{c \cdot T} \right\rceil \right)^{N-P+1} \tag{3.57}$$

Using the approximation shown in (3.46) when $N = P+1$, it can be observed that,

$$\frac{\sigma_x}{c \cdot T} \approx \frac{\overline{\sigma}_\lambda \cdot c\sqrt{\frac{P}{N-1}}}{\frac{1}{c \cdot T}} \approx \frac{\overline{\sigma}_\lambda}{T} << 1 \tag{3.58}$$

This means, that the complexity of the ambiguity problem can be reduced to,

$$O \propto \left(\left\lceil \frac{R/c + \triangle t}{T} \right\rceil \right)^{(P+1)} \tag{3.59}$$

The conclusion is that the complexity of ambiguity only depends on the initial ambiguity in position and clock, not on the number of used pulsars. Additionally, the internal clock will be in most cases stable enough not to add additional ambiguity points, so it can be removed from (3.59).

Problems related with ambiguity resolution

One of the most critical problems related with ambiguity is that a power failure could stop the location system during a certain period of time (failure-time). After that, the ambiguity resolution algorithm will spend some time before restoring the spacecraft tracking regime. In this particular case, the ambiguity resolution task will be difficult if the number of initial ambiguity points (values for $\mathbf{m}$) rises to huge values. Indeed, the complexity associated with ambiguity resolution is related with the initial coarse location or previous position estimate. So can the effect of a power-failure be derived.

Accuracy versus ambiguity resolution

It is clear from previous subsections that the best pulsars to resolve the ambiguity problem are those with large periods. Fortunately, they are also the most powerful pulsars in terms of SNR. Nevertheless, their timing noise is higher than for millisecond pulsars and the latter should be used to stabilize large period pulsars over long time spans. Millisecond pulsars will allow to improve the accuracy but they are not good resolving ambiguities so they cannot be used as the first $P+1$ pulsars needed to define the first ambiguity points.

3.5 Numerical simulation

This section presents the numerical simulations conducted to show the main features of the proposed algorithm: achievable position accuracy and some results related with the ambiguity resolution problem.

3.5.1 Results with a single observation window

This first subsection shows the performances of the location algorithm based on a single observation window.

- Figure (3.3) shows the achievable timing performance for each of the best ten pulsars. Their corresponding time threshold[2] can be observed in the same figure. This time threshold (the vertical line of the same color) represents the minimum integration time needed to use the associated pulsar timing estimate.
- Figure (3.4) shows the location algorithm performances for the best 10 pulsars, always taking the best combination. This means that the algorithm will intelligently select the pulsars with minimum time-thresholds to provide a position with minimum latency. As integration time progresses, additional pulsars can be incorporated to the location process. This figure is divided into four sections showing: the position accuracy, the individual coordinates accuracy, the number of used pulsars (due to the minimum time threshold) and the accuracy in the internal clock estimation.
- Figures (3.5) and (3.6) show the location algorithm performances using only 4 pulsars. In the first figure, the best pulsars are chosen in terms of accuracy while in the second one, the best pulsars are selected in terms of time-threshold. This means that the first selection will obtain better accuracies with enough integration time while the second one will provide a solution in the minimum time. These two figures, organized as in figure (3.4), allow us to compare the trade-off between time and accuracy if only four pulsars are selected.

3.5.2 Results with a multiple observation window

It is clear that the single observation window model cannot be infinitely extended in time. So, the multiple observation window model must be used. This section provides simulations using multiple observation windows.

Choosing the best combination of pulsars to perform the position estimation with multiple observation windows is not a trivial task. It has to be taken into account that if a group of pulsars is large, it will achieve better performances (for large observation windows) but at the same time, the minimum integration time for each individual window will increase, along with the minimum time to get the first position estimate. Figure (3.7) shows the best performances for each instant of time choosing the most favorable group of pulsars. The algorithm first groups a few pulsars (four) to get a short time-threshold and medium position accuracies and later more pulsars are incorporated to improve the position accuracy. As we are selecting the best combination in terms of accuracy, the best combination in terms of clock estimation is unpredictable. For long observation periods, it seems that both estimations (clock and position) are good enough.

[2] as shown later, the equations describing phase noise are valid above a minimum observation time. This question is addressed in detail in the timing estimation chapter.

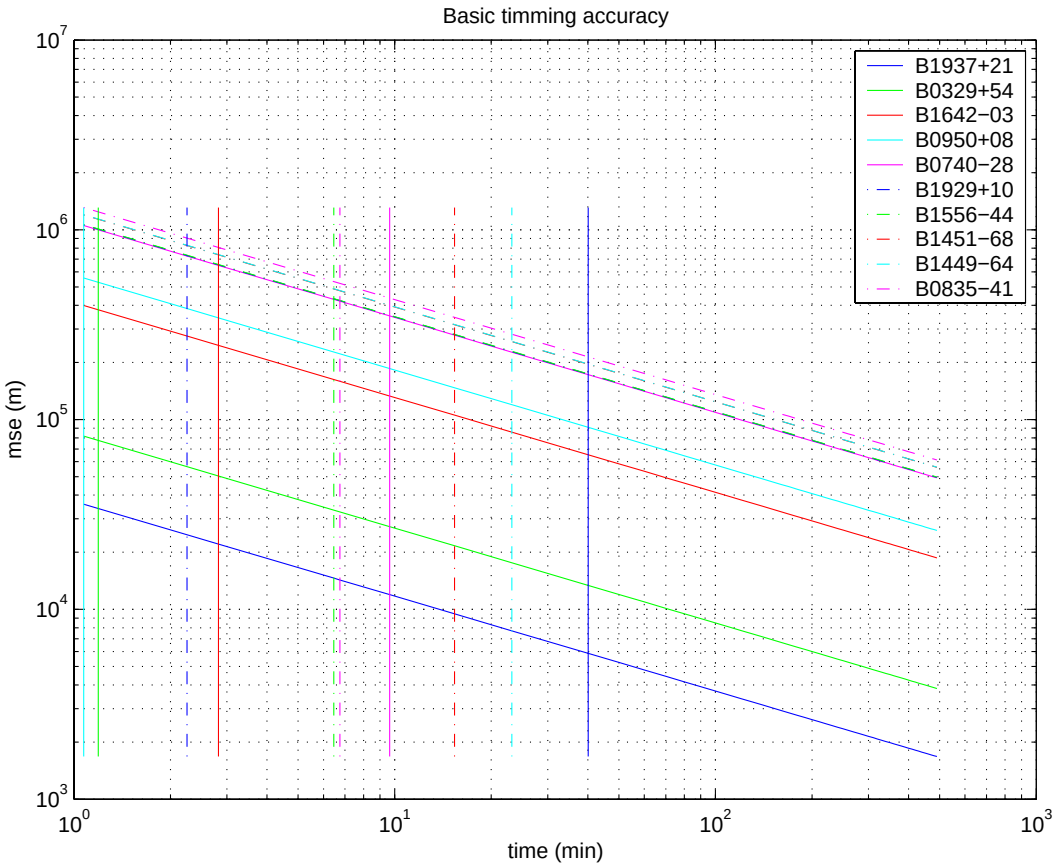

Figure 3.3: Timing accuracies for the best 10 pulsars

The accuracies presented in figure (3.7) are then the best accuracies achievable with any combination of the first 10 pulsars.

For comparison, the performances obtained with a single observation window are reproduced. The precision of the internal clock estimation is also simulatred. This performance can be used to study the possibility of correcting the onboard clock in very long space journeys.

Finally figures (3.8) and (3.9) show the same performance but when only the best 4 pulsars are used. Here, there are no multiple possible combinations. Each figure shows the best selection of four pulsars in terms of accuracy and time threshold.

3.5.3 Ambiguity resolution results

The most important technique to ameliorate the ambiguity phenomena is the first proposed technique based on the estimation of the internal clock and the comparison with the hardware-based internal clock. The purpose here is to estimate the internal clock using one additional pulsar (four pulsars in total) and to compare with the internal hardware-based clock. For each one of the possible ambiguity points (values for the vector $\mathbf{m}$ that gives a position inside the initial coarse position estimation), the estimated clock is compared with the real hardware clock. If the difference (also called time offset) is larger than the standard deviation associated with the clock estimation (See previous sections for more details) then, this point is discarded.

Here, we present a brief simulation of the effect of this first technique. The first six valid pulsars have been taken in order to check which combination (of four pulsars) yields the best ambiguity resolution performance.

- Tables (3.1) and (3.2) summarize the results of the experiment. Each row represents the performance

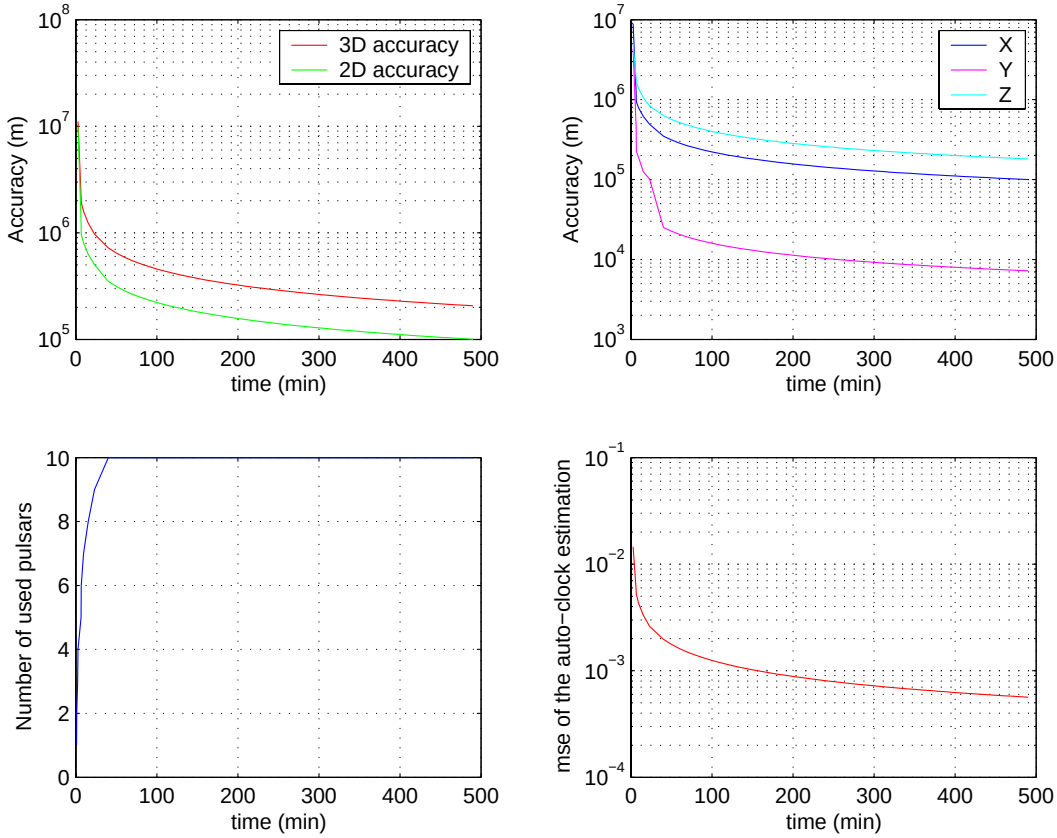

Figure 3.4: Performances with the best 10 Pulsars

associated to each combination of pulsars. The first column shows the combination itself, specifying pulsrs as shown in table (2.1). It is important to note that the first pulsar in that table has not been used because its period is very small, and the complexity of ambiguity resolution is considerable.

- The second column provides the minimum integration time for the associated combination of pulsars and also the time used in the simulation.
- The third column shows the accuracy of internal clock estimation. This is a crucial parameter in the ambiguity resolution problem.
- The following six columns correspond (in groups of two columns) to the results of the simulations for three different values of initial coarse position estimation: 10^8, $5 \cdot 10^8$ and 10^9 meters. Each of the simulations shows in their two columns the number of ambiguity points (first column) and the number of ambiguity points that remains after the first ambiguity resolution technique. In these second columns, the minimum time-offset associated with ambiguity points is also presented in order to show how close to fail/sucsses the ambiguity resolution algorithm is.

The most important point is that the combination that has zero ambiguity points after the first technique does not require additional pulsars to solve the ambiguity.

The conclusion is that the resolution ambiguity problem will be really complex if the ambiguity of the position grows up to several times the period of the pulsars used (translated to distances multiplying by c). This could be caused by a power failure of a temporal disconnection of the location algorithm.

Table 3.1: Number of ambiguity points for all possible pulsar combinations

Comb	Time precision (seconds)	Amb. Points $R = 10^8\,m$	Time offset and Amb. points $R = 10^8\,m$ (seconds)	Amb. Points $R = 5 \cdot 10^8\,m$	Time offset and Amb. points $R = 5 \cdot 10^8\,m$ (seconds)	Amb. Points $R = 10^9\,m$	Time offset and Amb. points $R = 10^9\,m$ (seconds)
7 8 9 10	0.006186	10	0.619412 / 0	1040	0.002413 / 6	7286	0.000455 / 80
6 8 9 10	0.008192	2	0.749464 / 0	464	0.029890 / 6	3230	0.003680 / 42
6 7 9 10	0.009820	2	0.553987 / 0	514	0.003609 / 4	3822	0.003609 / 56
6 7 8 10	0.005467	8	0.676002 / 0	888	0.004347 / 6	6790	0.000232 / 58
6 7 8 9	0.009635	6	0.541348 / 0	948	0.013010 / 12	6582	0.000238 / 114
5 8 9 10	0.004362	8	0.901348 / 0	1220	0.001568 / 6	8592	0.001568 / 62
5 7 9 10	0.006027	4	1.981424 / 0	870	0.016083 / 6	6436	0.000104 / 52
5 7 8 10	0.008501	4	1.515392 / 0	492	0.001034 / 4	3792	0.001034 / 48
5 7 8 9	0.022387	2	1.645327 / 0	514	0.012865 / 22	3542	0.002131 / 144
5 6 9 10	0.013306	0	– / 0	218	0.020813 / 6	1800	0.007701 / 30
5 6 8 10	0.003215	12	0.024754 / 0	1266	0.000064 / 4	9584	0.000064 / 36
5 6 8 9	0.010246	6	0.183642 / 0	902	0.007497 / 16	6240	0.000878 / 114
5 6 7 10	0.003939	12	0.811416 / 0	1114	0.010689 / 6	8360	0.000072 / 34
5 6 7 9	0.009504	4	3.292745 / 0	530	0.009572 / 6	4004	0.002355 / 58
5 6 7 8	0.009825	8	0.550958 / 0	882	0.001201 / 14	6684	0.001201 / 100
4 8 9 10	0.004260	14	0.615269 / 0	1626	0.001714 / 10	11404	0.000163 / 82
4 7 9 10	0.006187	8	2.538499 / 0	798	0.013305 / 4	5922	0.001607 / 50
4 7 8 10	0.011981	2	0.696712 / 0	226	0.016142 / 2	1662	0.010538 / 26
4 7 8 9	1.574750	0	– / 0	12	0.100168 / 12	68	0.079125 / 68
4 6 9 10	0.011232	2	0.794299 / 0	452	0.010698 / 8	3608	0.002893 / 54
4 6 8 10	0.003573	12	0.640074 / 0	1500	0.005507 / 12	11318	0.000285 / 56
4 6 8 9	0.009688	12	0.155647 / 0	1498	0.001162 / 18	10360	0.000181 / 178
4 6 7 10	0.004785	6	1.427413 / 0	904	0.000242 / 4	6750	0.000242 / 38
4 6 7 9	0.009626	4	1.091649 / 0	726	0.001837 / 8	5402	0.001557 / 76
4 6 7 8	0.055271	2	0.918034 / 0	178	0.017223 / 12	1422	0.007016 / 114
4 5 9 10	0.009677	2	2.223698 / 0	414	0.009574 / 4	3350	0.003284 / 42
4 5 8 10	0.006355	8	0.534484 / 0	500	0.000690 / 2	3988	0.000217 / 18
4 5 8 9	0.014219	8	1.638102 / 0	814	0.008895 / 18	5650	0.001555 / 146
4 5 7 10	0.012368	0	– / 0	230	0.053488 / 2	1744	0.004039 / 24
4 5 7 9	0.014321	4	1.840221 / 0	398	0.022602 / 8	2964	0.004707 / 66
4 5 7 8	0.049747	0	– / 0	110	0.075757 / 6	850	0.002703 / 66
4 5 6 10	0.005853	16	0.826915 / 0	702	0.019051 / 4	5098	0.000678 / 24
4 5 6 9	0.007175	2	3.480553 / 0	166	0.051531 / 0	1272	0.001750 / 14
4 5 6 8	0.007121	28	0.156164 / 0	1294	0.002219 / 10	9196	0.002219 / 104
4 5 6 7	0.007336	16	0.336415 / 0	700	0.005113 / 8	4916	0.005113 / 42
3 8 9 10	0.014165	4	1.631889 / 0	392	0.000962 / 10	2828	0.000962 / 68
3 7 9 10	0.006138	4	2.424509 / 0	638	0.002567 / 4	4632	0.002567 / 38
3 7 8 10	0.004758	0	– / 0	198	0.021131 / 2	1572	0.003802 / 8
3 7 8 9	0.004717	16	0.100901 / 0	2512	0.006792 / 12	17770	0.000209 / 150
3 6 9 10	0.008954	2	0.714296 / 0	480	0.002231 / 10	3856	0.001087 / 46
3 6 8 10	0.010042	4	1.430937 / 0	438	0.001177 / 6	3268	0.000550 / 44
3 6 8 9	0.008576	8	0.147244 / 0	1500	0.005230 / 22	10366	0.000564 / 150
3 6 7 10	0.006711	2	3.701364 / 0	504	0.006408 / 8	3764	0.000312 / 64
3 6 7 9	0.009961	0	– / 0	670	0.000535 / 8	5028	0.000535 / 76
3 6 7 8	0.004560	12	0.139728 / 0	1978	0.000518 / 14	15194	0.000358 / 112
3 5 9 10	0.003483	6	0.501480 / 0	1088	0.004527 / 4	8688	0.000207 / 42
3 5 8 10	0.073216	0	– / 0	42	0.036907 / 4	340	0.005861 / 36
3 5 8 9	0.003520	28	0.078382 / 0	3190	0.000515 / 16	22328	0.000028 / 134
3 5 7 10	0.004850	2	3.575284 / 0	536	0.002898 / 2	4036	0.002898 / 18
3 5 7 9	0.003303	16	0.172656 / 0	1788	0.004330 / 12	13374	0.000594 / 64
3 5 7 8	0.005272	10	0.341268 / 0	1268	0.002294 / 8	9946	0.002294 / 82
3 5 6 10	0.002464	8	0.858450 / 0	1424	0.007792 / 2	11212	0.001202 / 20
3 5 6 9	0.002746	0	– / 0	204	0.015809 / 0	1688	0.000954 / 2
3 5 6 8	0.002476	28	0.020322 / 0	3240	0.000796 / 8	24742	0.000100 / 86
3 5 6 7	0.002433	14	0.830086 / 0	2018	0.007562 / 4	15060	0.000325 / 40
3 4 9 10	0.001590	10	0.746618 / 0	1324	0.002292 / 4	10358	0.000279 / 24
3 4 8 10	0.006994	0	– / 0	224	0.004392 / 2	1788	0.001778 / 18
3 4 8 9	0.001580	36	0.077372 / 0	3960	0.000779 / 10	27712	0.000447 / 74
3 4 7 10	0.003705	2	3.808672 / 0	328	0.010508 / 2	2570	0.000330 / 12
3 4 7 9	0.001687	12	0.672678 / 0	1946	0.000057 / 4	14420	0.000057 / 32
3 4 7 8	0.006339	2	3.561523 / 0	506	0.003293 / 4	4098	0.003293 / 36
3 4 6 10	0.001366	18	0.879176 / 0	1418	0.000393 / 2	10720	0.000393 / 14
3 4 6 9	0.011295	0	– / 0	84	0.015879 / 2	628	0.015879 / 8
3 4 6 8	0.001343	30	0.085780 / 0	3388	0.000118 / 10	25982	0.000118 / 46
3 4 6 7	0.001452	18	0.811181 / 0	1892	0.008612 / 0	14244	0.000604 / 22
3 4 5 10	0.002606	8	0.895984 / 0	600	0.005608 / 4	4644	0.000162 / 16
3 4 5 9	0.002192	4	2.686098 / 0	378	0.007699 / 2	3042	0.007699 / 4
3 4 5 8	0.002698	14	0.178989 / 0	1362	0.011271 / 2	10494	0.000505 / 40
3 4 5 7	0.003146	6	0.747757 / 0	716	0.002221 / 2	5488	0.001705 / 20
3 4 5 6	0.002105	8	0.862308 / 0	404	0.006415 / 2	2898	0.006415 / 4
2 8 9 10	0.004831	4	1.541743 / 0	266	0.009398 / 2	1854	0.002277 / 14

Table 3.2: Number of ambiguity points for all possible pulsar combinations

2 7 9 10	0.006569	6	0.474306 / 0	214	0.070538 / 0	1548	0.000388 / 14
2 7 8 10	0.007255	2	3.127843 / 0	230	0.009915 / 6	1794	0.003444 / 14
2 7 8 9	0.015797	8	0.780401 / 0	166	0.026890 / 4	1160	0.003739 / 30
2 6 9 10	0.015372	0	– / 0	44	0.069051 / 2	326	0.000412 / 6
2 6 8 10	0.002886	4	0.881775 / 0	330	0.043132 / 0	2450	0.000394 / 20
2 6 8 9	0.010887	2	0.192153 / 0	184	0.060804 / 0	1216	0.005063 / 28
2 6 7 10	0.003246	2	2.097008 / 0	336	0.011696 / 2	2472	0.001914 / 8
2 6 7 9	0.009373	0	– / 0	114	0.028978 / 2	808	0.002125 / 10
2 6 7 8	0.005469	0	– / 0	344	0.018026 / 2	2664	0.001500 / 20
2 5 9 10	0.020640	0	– / 0	24	0.216456 / 0	196	0.029446 / 6
2 5 8 10	0.006118	0	– / 0	142	0.010154 / 2	1094	0.010154 / 10
2 5 8 9	0.023383	0	– / 0	68	0.049461 / 4	460	0.010021 / 26
2 5 7 10	0.010081	2	0.738609 / 0	112	0.042394 / 2	796	0.002147 / 10
2 5 7 9	0.024162	0	– / 0	42	0.103535 / 2	288	0.023227 / 12
2 5 7 8	0.057558	0	– / 0	38	0.107120 / 4	240	0.013064 / 28
2 5 6 10	0.007942	2	2.916897 / 0	60	0.306427 / 0	530	0.033726 / 2
2 5 6 9	0.012302	0	– / 0	2	2.554955 / 0	46	0.120105 / 0
2 5 6 8	0.007002	8	0.086056 / 0	146	0.086056 / 0	1344	0.000400 / 20
2 5 6 7	0.006608	2	2.813060 / 0	94	0.172303 / 0	864	0.013683 / 2
2 4 9 10	0.008923	0	– / 0	126	0.007651 / 2	1000	0.007651 / 10
2 4 8 10	0.004786	2	2.252878 / 0	294	0.013205 / 2	2334	0.000445 / 16
2 4 8 9	0.011449	2	2.815851 / 0	268	0.025570 / 2	1888	0.001269 / 36
2 4 7 10	0.007852	2	3.721996 / 0	154	0.094905 / 0	1202	0.006291 / 14
2 4 7 9	0.011342	2	2.754090 / 0	134	0.093734 / 0	998	0.004018 / 14
2 4 7 8	0.076623	0	– / 0	32	0.076380 / 2	292	0.034784 / 32
2 4 6 10	0.003742	6	2.366221 / 0	246	0.010466 / 2	1858	0.001757 / 8
2 4 6 9	0.005099	0	– / 0	40	0.388861 / 0	322	0.043186 / 0
2 4 6 8	0.003928	8	2.304681 / 0	508	0.020400 / 0	3940	0.001372 / 24
2 4 6 7	0.003939	2	2.948063 / 0	284	0.005468 / 2	2106	0.005468 / 6
2 4 5 10	0.019066	0	– / 0	46	0.050701 / 2	406	0.050701 / 4
2 4 5 9	0.030315	0	– / 0	6	0.365737 / 0	56	0.010737 / 2
2 4 5 8	0.031413	2	3.012448 / 0	68	0.027332 / 2	510	0.000856 / 20
2 4 5 7	0.030048	0	– / 0	30	0.084817 / 2	306	0.001585 / 8
2 4 5 6	0.004757	2	2.883243 / 0	26	0.266325 / 0	236	0.021937 / 2
2 3 9 10	0.004348	2	0.894553 / 0	250	0.023620 / 0	1940	0.003203 / 8
2 3 8 10	0.036797	0	– / 0	32	0.120593 / 2	264	0.004405 / 10
2 3 8 9	0.004386	10	0.084849 / 0	710	0.001583 / 10	4980	0.000641 / 58
2 3 7 10	0.005356	0	– / 0	208	0.046282 / 0	1636	0.003683 / 10
2 3 7 9	0.004093	8	0.785294 / 0	416	0.017332 / 2	3000	0.002831 / 18
2 3 7 8	0.004982	4	0.850904 / 0	570	0.004451 / 4	4610	0.000452 / 40
2 3 6 10	0.002278	6	2.277387 / 0	404	0.028760 / 0	3250	0.004215 / 6
2 3 6 9	0.002115	0	– / 0	50	0.091170 / 0	396	0.013055 / 0
2 3 6 8	0.002276	10	0.008368 / 2	896	0.008368 / 2	6826	0.000876 / 28
2 3 6 7	0.002292	4	2.273177 / 0	562	0.018250 / 0	4040	0.001300 / 8
2 3 5 10	0.005508	0	– / 0	168	0.019502 / 2	1334	0.006382 / 8
2 3 5 9	0.042195	0	– / 0	2	2.317904 / 0	24	0.439447 / 0
2 3 5 8	0.005547	6	0.071481 / 0	362	0.010023 / 4	2888	0.003492 / 20
2 3 5 7	0.005229	2	2.817605 / 0	240	0.007792 / 6	1850	0.006911 / 10
2 3 5 6	0.002122	2	2.815522 / 0	26	0.281405 / 0	216	0.002089 / 2
2 3 4 10	0.001639	8	0.710184 / 0	338	0.054110 / 0	2746	0.000673 / 6
2 3 4 9	0.002661	4	0.818581 / 0	94	0.036184 / 0	754	0.006652 / 2
2 3 4 8	0.001610	28	0.118898 / 0	768	0.001002 / 2	6412	0.001002 / 14
2 3 4 7	0.001798	10	0.587338 / 0	426	0.009335 / 0	3546	0.000429 / 6
2 3 4 6	0.002446	0	– / 0	76	0.135882 / 0	634	0.009648 / 2
2 3 4 5	0.003538	0	– / 0	56	0.013102 / 2	446	0.013102 / 2

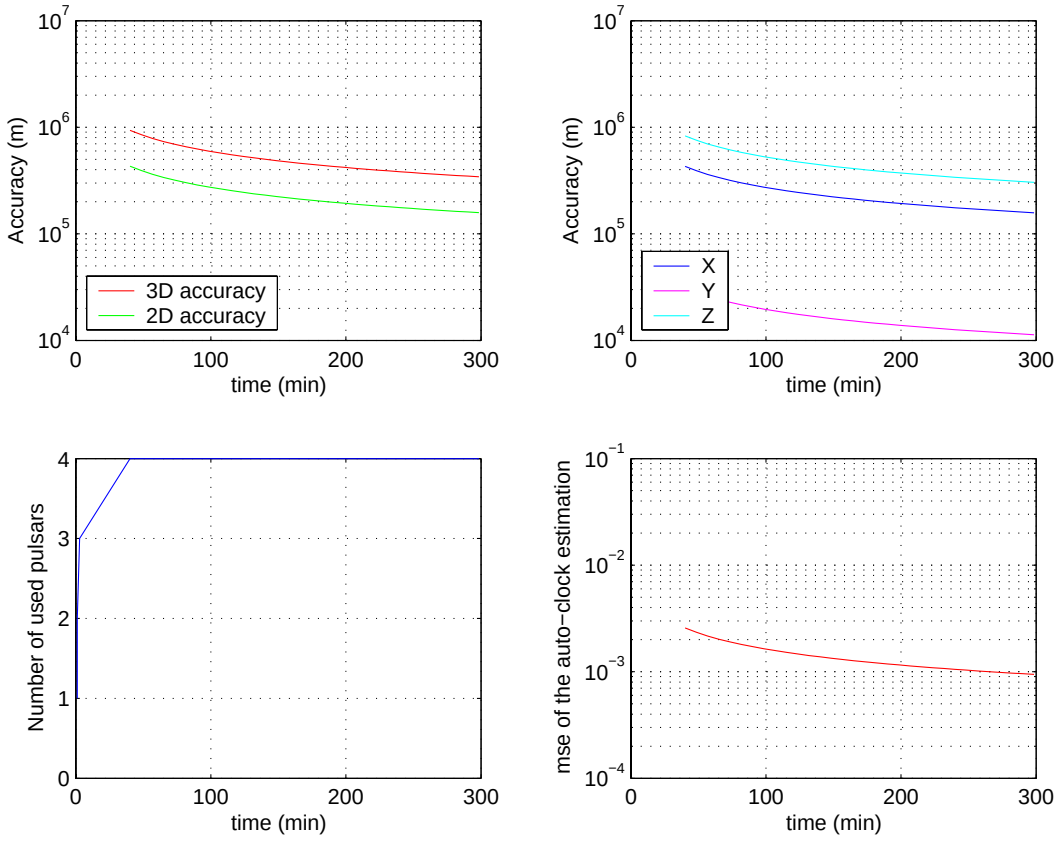

Figure 3.5: Performances with the best 4 Pulsars (in accuracy)

3.6 Appendix A

This appendix shows the development needed to compute the success and fail probabilities of ambiguity resolution. This is basically the performance of the second technique previously presented for resolving ambiguity. This appendix is organized as follows: first, a general signal model is presented for single and multiple observation windows; second, the ML function is presented and evaluated at the correct $\mathbf{m}$ and at a hypothetically incorrect value; finally, a closed-form expression for the ambiguity error is presented.

3.6.1 General signal model for single and multiple observation windows

There are two interesting scenarios to evaluate the ambiguity problem. First, in a single observation window, a set of N phase and PATD estimates will be available (this case is interesting for evaluating the magnitude of the ambiguity problem); secondly, a generic scenario with L consecutive observation windows and additional previous measurements constitutes the general framework needed to extract valid conclusions. It will become clear in this first subsection that both problems can be analyzed mathematically with the same expressions by means of defining a common signal model. The general signal model proposed for both cases can be expressed as follows,

$$\mu = \mathbf{A} \cdot \widetilde{\mathbf{x}} + \mathbf{F}_m \cdot \mathbf{m} + \mathbf{w}_\mu \tag{3.60}$$

where μ is the general sampling vector containing all available measurements, $\mathbf{A}$ is a generic model matrix, $\widetilde{\mathbf{x}}$ is the vector containing the unknown terms (as position, speed, etc), $\mathbf{m}$ is the integer ambiguity vector and $\mathbf{w}_\mu$ is the vector containing the noise terms associated with the samples included in μ.

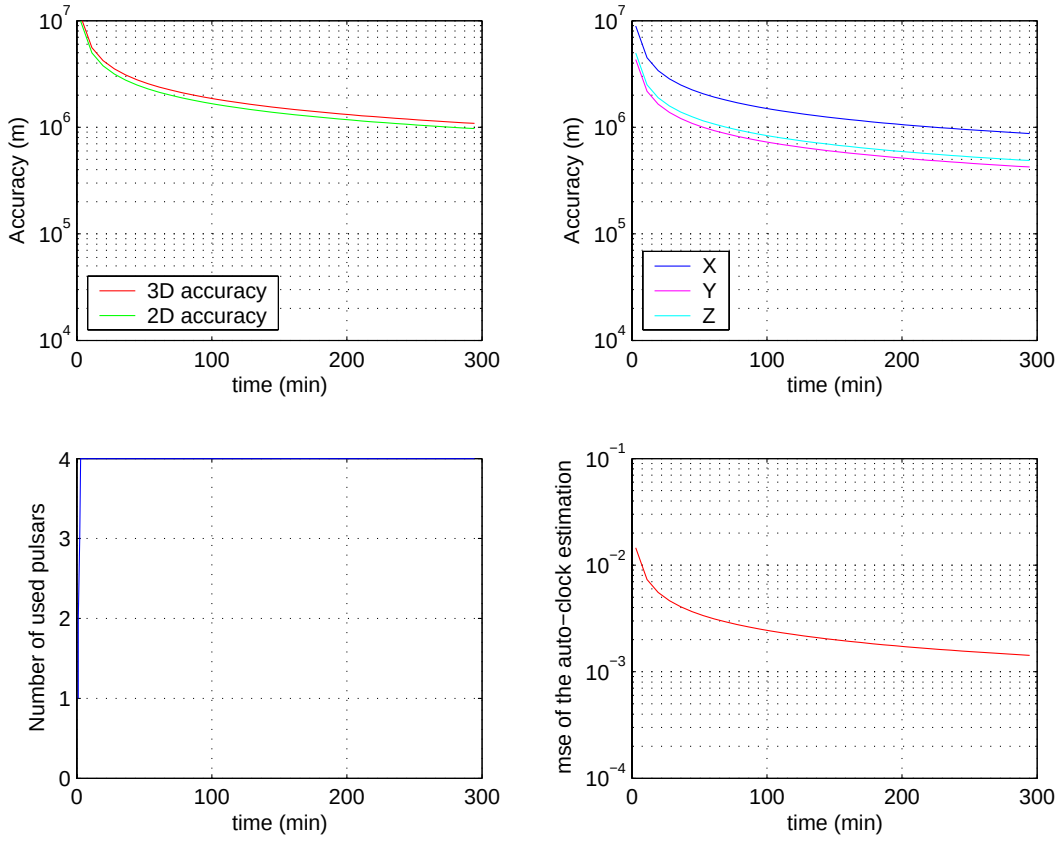

Figure 3.6: Performances with the best 4 Pulsars (in latency)

Single observation window

In this specific case, the spacecraft is assumed to be static during the observation window. Additionally, the PATD estimates are only related with the speed of the spacecraft, not with its position. The only available measurements in this scenario are the phase estimates. The unknowns are position and the time offset (not speed). It can be seen that the signal model proposed in (3.18) perfectly fits in the general signal model proposed in (3.60) assuming the following definitions,

$$\mu = \lambda \qquad \mathbf{A} = \begin{bmatrix} \mathbf{1}_N & \mathbf{U} \end{bmatrix} \qquad \widetilde{\mathbf{x}} = \begin{bmatrix} t \\ \mathbf{x} \end{bmatrix} \qquad \mathbf{F}_m = \mathbf{F} \qquad \mathbf{w}_\mu = \mathbf{w}_\lambda \tag{3.61}$$

Finally, the covariance matrix for the noise vector can be expressed in this case as,

$$\mathbf{R}_\mu = E\left[\mathbf{w}_\mu \mathbf{w}_\mu^T\right] = \mathbf{R}_\lambda \tag{3.62}$$

Multiple observation windows

For the sake of generality, we will assume that L consecutive observation windows are used to estimate the N phase evolutions and the N PATDs associated to the N available pulsars. We will also assume that a previous position and speed estimate are available. If these two last estimates are not available, high variances are used for both estimates in the equations. Let us define the previous position and speed estimates as follows,

$$\widehat{\mathbf{x}}_p = \mathbf{x} + \mathbf{w}_{\widehat{\mathbf{x}}_p} \tag{3.63}$$

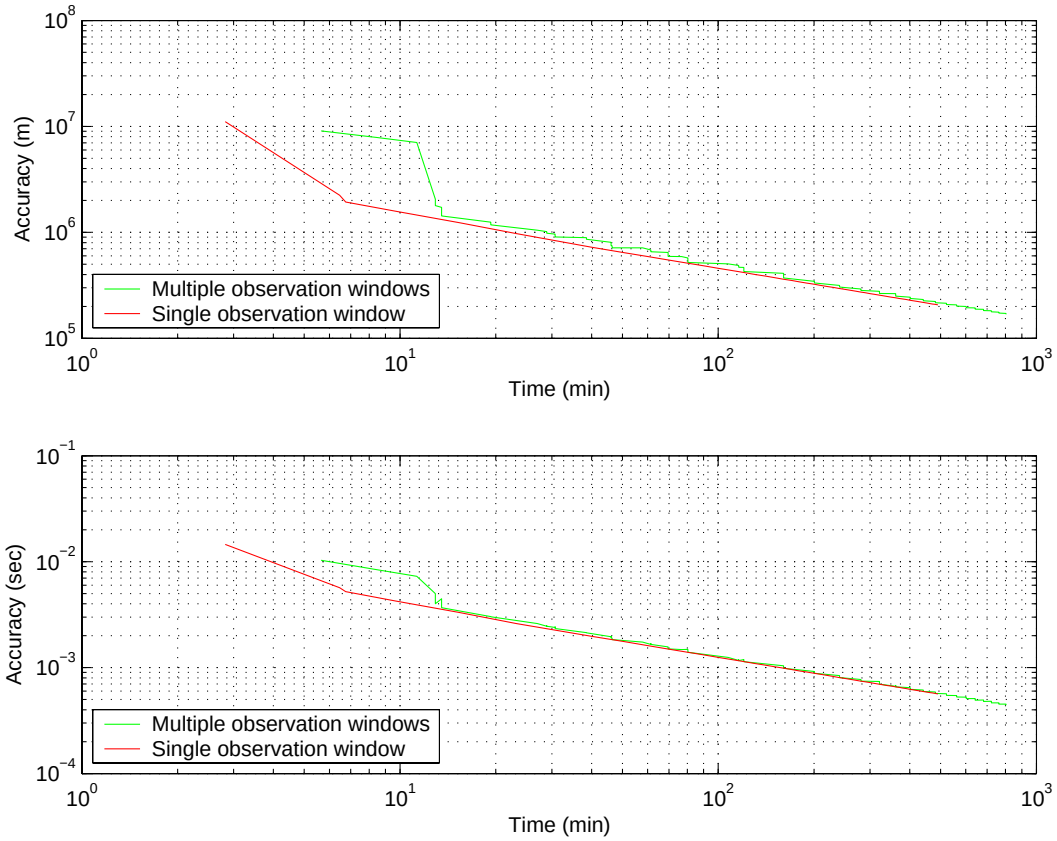

Figure 3.7: Performances with multiple observation windows (5 pulsars)

$$\widehat{\mathbf{s}}_p = \mathbf{s} + \mathbf{w}_{\widehat{\mathbf{s}}_p} \tag{3.64}$$

where the covariance matrices of both previous estimates are considered known,

$$\mathbf{R}_{\widehat{\mathbf{x}}_p} = E\left[\mathbf{w}_{\widehat{\mathbf{x}}_p}\mathbf{w}_{\widehat{\mathbf{x}}_p}^T\right] \tag{3.65}$$

$$\mathbf{R}_{\widehat{\mathbf{s}}_p} = E\left[\mathbf{w}_{\widehat{\mathbf{s}}_p}\mathbf{w}_{\widehat{\mathbf{s}}_p}^T\right] \tag{3.66}$$

Note again that if one or both of these measurements is not really available, we only have to replace the associated covariance matrix with: $R = \infty\mathbf{I}$. Now, fusing the signal model for these previous estimates and the signal model shown in (3.25) and (3.27), we have,

$$\begin{bmatrix} \widetilde{\lambda} \\ \widetilde{\gamma} \\ \widehat{\mathbf{x}}_p \\ \widehat{\mathbf{s}}_p \end{bmatrix} = \begin{bmatrix} \mathbf{A}_\lambda \\ \mathbf{A}_\gamma \\ [\mathbf{0}_{P,1}\mathbf{I}_P, \mathbf{0}_{P,P}] \\ [\mathbf{0}_{P,1}\mathbf{0}_{P,P}, \mathbf{I}_P] \end{bmatrix} \cdot \begin{bmatrix} t \\ \mathbf{x} \\ \mathbf{s} \end{bmatrix} + \begin{bmatrix} \widetilde{\mathbf{F}} \\ \mathbf{0} \\ \mathbf{0} \\ \mathbf{0} \end{bmatrix} \cdot \mathbf{m} + \begin{bmatrix} \mathbf{w}_{\widetilde{\lambda}} \\ \mathbf{w}_{\widetilde{\gamma}} \\ \mathbf{w}_{\widehat{\mathbf{x}}_p} \\ \mathbf{w}_{\widehat{\mathbf{s}}_p} \end{bmatrix} \tag{3.67}$$

where, it is easy to identify all terms presented in equation (3.60) as follows,

$$\mu = \begin{bmatrix} \widetilde{\lambda} \\ \widetilde{\gamma} \\ \widehat{\mathbf{x}}_p \\ \widehat{\mathbf{s}}_p \end{bmatrix} \qquad \mathbf{A} = \begin{bmatrix} \mathbf{A}_\lambda \\ \mathbf{A}_\gamma \\ [\mathbf{0}_{P,1}\mathbf{I}_P, \mathbf{0}_{P,P}] \\ [\mathbf{0}_{P,1}\mathbf{0}_{P,P}, \mathbf{I}_P] \end{bmatrix} \qquad \widetilde{\mathbf{x}} = \begin{bmatrix} t \\ \mathbf{x} \\ \mathbf{s} \end{bmatrix} \tag{3.68}$$

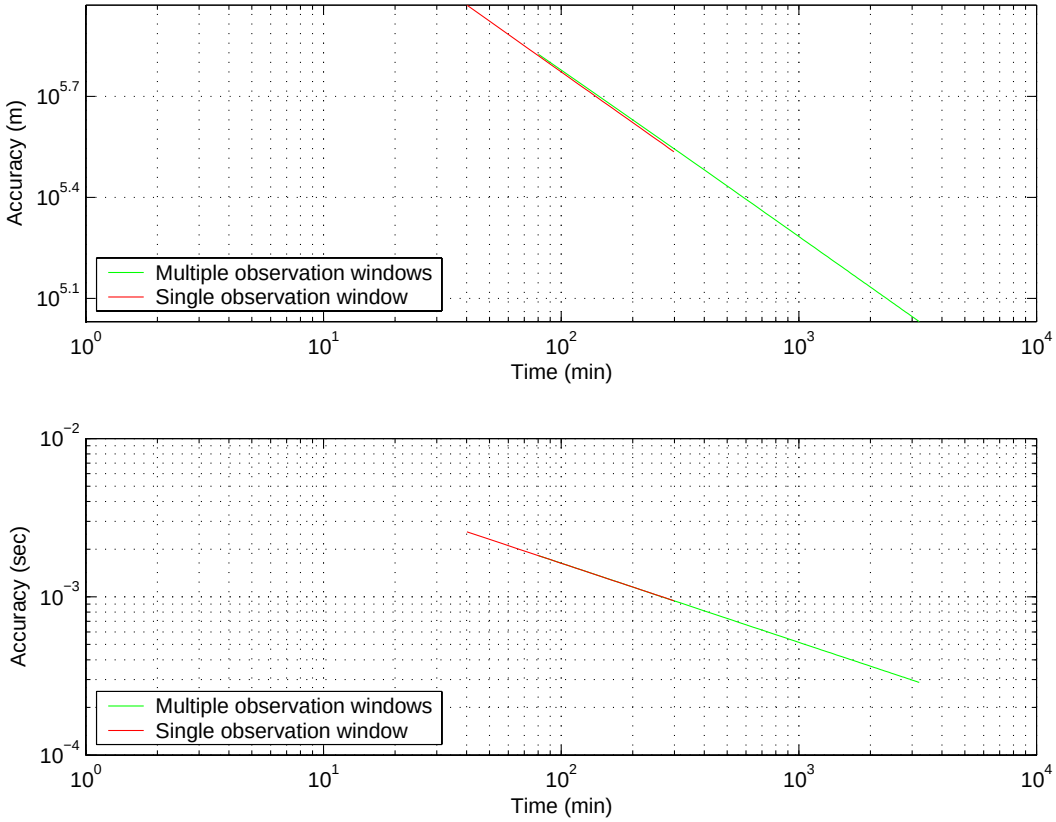

Figure 3.8: Performances with multiple observation windows (4 pulsars)

$$\mathbf{F}_m = \begin{bmatrix} \widetilde{\mathbf{F}} \\ \mathbf{0} \\ \mathbf{0} \\ \mathbf{0} \end{bmatrix} \qquad \mathbf{w}_\mu = \begin{bmatrix} \mathbf{w}_{\widetilde{\lambda}} \\ \mathbf{w}_{\widetilde{\gamma}} \\ \mathbf{w}_{\widehat{\mathbf{x}}_p} \\ \mathbf{w}_{\widehat{\mathbf{s}}_p} \end{bmatrix} \tag{3.69}$$

Finally, the covariance matrix for the noise vector can be expressed in this case as,

$$\mathbf{R}_\mu = E\left[\mathbf{w}_\mu \mathbf{w}_\mu^T\right] = \begin{bmatrix} \mathbf{R}_{\widetilde{\lambda}} & \mathbf{0} & \mathbf{0} & \mathbf{0} \\ \mathbf{0} & \mathbf{R}_{\widetilde{\gamma}} & \mathbf{0} & \mathbf{0} \\ \mathbf{0} & \mathbf{0} & \mathbf{R}_{\widehat{\mathbf{x}}_p} & \mathbf{0} \\ \mathbf{0} & \mathbf{0} & \mathbf{0} & \mathbf{R}_{\widehat{\mathbf{s}}_p} \end{bmatrix} \tag{3.70}$$

3.6.2 ML function

From the common signal model shown in (3.60), it becomes clear that the ML function to be minimized can be formulated as,

$$\Psi_{ML}\left(\widetilde{\mathbf{x}}, \mathbf{m}\right) = \left(\mu - \mathbf{A} \cdot \widetilde{\mathbf{x}} - \mathbf{F}_m \cdot \mathbf{m}\right)^T \mathbf{R}_\mu^{-1} \left(\mu - \mathbf{A} \cdot \widetilde{\mathbf{x}} - \mathbf{F}_m \cdot \mathbf{m}\right) \tag{3.71}$$

The ML estimate of the unknown parameters included in $\widetilde{\mathbf{x}}$ can be obtained as follows,

$$\widehat{\widetilde{\mathbf{x}}} = \left(\mathbf{A}^T \mathbf{R}_\mu^{-1} \mathbf{A}\right)^{-1} \mathbf{A} \mathbf{R}_\mu^{-1} \left(\mu - \mathbf{F}_m \cdot \mathbf{m}\right) \tag{3.72}$$

Now, we can compress the ML function shown in (3.71) with the parameter estimate shown in (3.72).

$$\Psi_{ML,c}\left(\mathbf{m}\right) = \left[\left(\mathbf{A}^T \mathbf{R}_\mu^{-1} \mathbf{A}\right)^{-1} \mathbf{A} \mathbf{R}_\mu^{-1} \left(\mu - \mathbf{F}_m \cdot \mathbf{m}\right)\right]^T \mathbf{R}_\mu^{-1} \left[\left(\mathbf{A}^T \mathbf{R}_\mu^{-1} \mathbf{A}\right)^{-1} \mathbf{A} \mathbf{R}_\mu^{-1} \left(\mu - \mathbf{F}_m \cdot \mathbf{m}\right)\right] \tag{3.73}$$

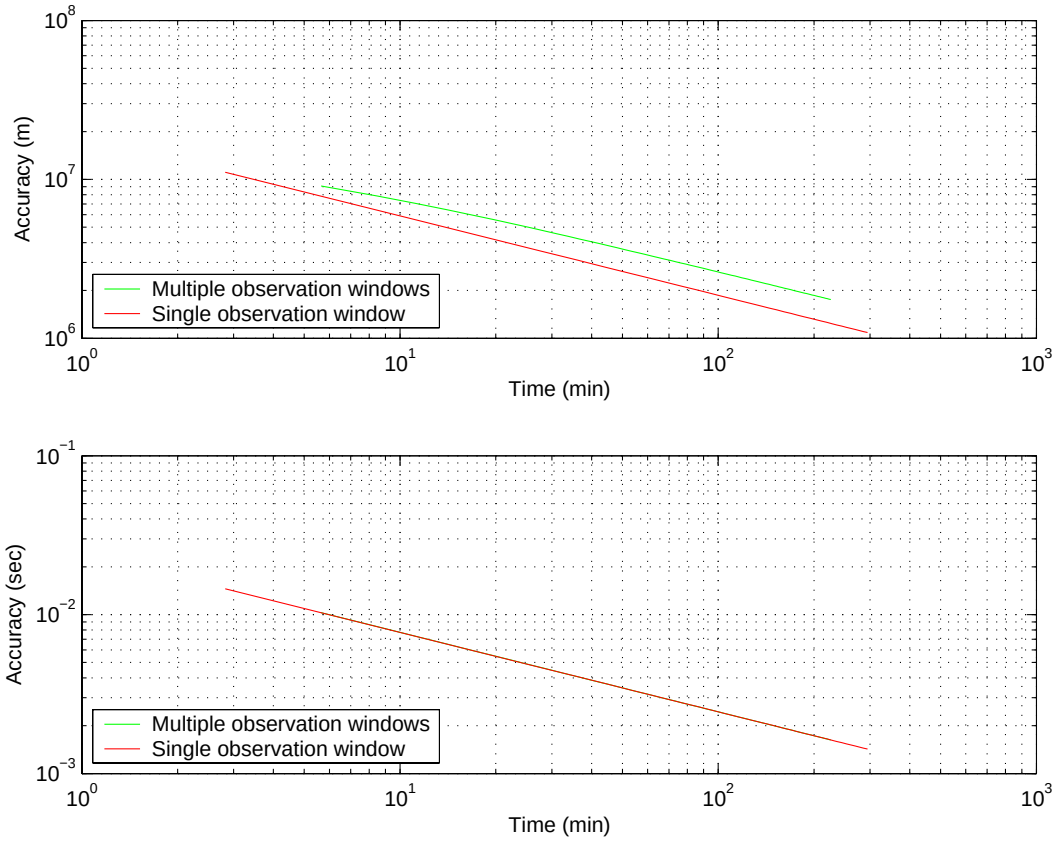

Figure 3.9: Performances with multiple observation windows (best 4 pulsars in terms of time threshold)

After several straightforward mathematical manipulations , we obtain,

$$\Psi_{ML,c}(\mathbf{m}) = (\mu - \mathbf{F}_m \cdot \mathbf{m})^T \left[\mathbf{R}_\mu^{-1} - \mathbf{R}_\mu^{-1}\mathbf{A}\left(\mathbf{A}^T\mathbf{R}_\mu^{-1}\mathbf{A}\right)^{-1}\mathbf{A}^T\mathbf{R}_\mu^{-1}\right](\mu - \mathbf{F}_m \cdot \mathbf{m}) \tag{3.74}$$

3.6.3 Ambiguity error probability

The ambiguity error probability is defined as the probability of not estimating $\mathbf{m}$ correctly. This can be expressed as,

$$p_{amb}(\Delta\mathbf{m}) = p\left(\Psi_{ML,c}(\mathbf{m} = \mathbf{m}_0 + \Delta\mathbf{m}) < \Psi_{ML,c}(\mathbf{m} = \mathbf{m}_0)\right) = p\left(\Delta\Psi_{ML,c}(\Delta\mathbf{m}) < 0\right) \tag{3.75}$$

where $\Delta\Psi_{ML,c}(\Delta\mathbf{m}) = \Psi_{ML,c}(\mathbf{m} = \mathbf{m}_0 + \Delta\mathbf{m}) - \Psi_{ML,c}(\mathbf{m} = \mathbf{m}_0)$. Note that if the value of the ML function using an incorrect estimate for $\mathbf{m}$ is lower than using the correct one, this will produce an ambiguity error. Now, assuming that measurements μ are obtained at the correct $\mathbf{m}$, this is $\mu = \mathbf{A} \cdot \widetilde{\mathbf{x}} + \mathbf{F}_m \cdot \mathbf{m}_0 + \mathbf{w}_\mu$. The ML function shown in (3.74) can be rewritten as follows,

$$\Psi_{ML,c}(\mathbf{m}) = (\mathbf{w}_\mu - \mathbf{F}_m \cdot \Delta\mathbf{m})^T \left[\mathbf{R}_\mu^{-1} - \mathbf{R}_\mu^{-1}\mathbf{A}\left(\mathbf{A}^T\mathbf{R}_\mu^{-1}\mathbf{A}\right)^{-1}\mathbf{A}^T\mathbf{R}_\mu^{-1}\right](\mathbf{w}_\mu - \mathbf{F}_m \cdot \Delta\mathbf{m}) \tag{3.76}$$

Finally, the difference of the ML function between the correct and the incorrect estimates of $\mathbf{m}$ is obtained,

$$\Delta\Psi_{ML,c}(\Delta\mathbf{m}) = (\mathbf{w}_\mu - \mathbf{F}_m \cdot \Delta\mathbf{m})^T \left[\mathbf{R}_\mu^{-1} - \mathbf{R}_\mu^{-1}\mathbf{A}\left(\mathbf{A}^T\mathbf{R}_\mu^{-1}\mathbf{A}\right)^{-1}\mathbf{A}^T\mathbf{R}_\mu^{-1}\right](\mathbf{w}_\mu - \mathbf{F}_m \cdot \Delta\mathbf{m}) - \tag{3.77}$$

$$(\mathbf{w}_\mu)^T \left[\mathbf{R}_\mu^{-1} - \mathbf{R}_\mu^{-1}\mathbf{A}\left(\mathbf{A}^T\mathbf{R}_\mu^{-1}\mathbf{A}\right)^{-1}\mathbf{A}^T\mathbf{R}_\mu^{-1}\right](\mathbf{w}_\mu) \tag{3.78}$$

which, after several mathematical manipulations, can be expressed as,

$$\Delta\Psi_{ML,c}\left(\Delta\mathbf{m}\right) = \left(\mathbf{F}_m \cdot \Delta\mathbf{m}\right)^T \left[\mathbf{R}_\mu^{-1} - \mathbf{R}_\mu^{-1}\mathbf{A}\left(\mathbf{A}^T\mathbf{R}_\mu^{-1}\mathbf{A}\right)^{-1}\mathbf{A}^T\mathbf{R}_\mu^{-1}\right]\left(\mathbf{F}_m \cdot \Delta\mathbf{m}\right) \tag{3.79}$$

$$-2\left(\mathbf{w}_\mu\right)^T \left[\mathbf{R}_\mu^{-1} - \mathbf{R}_\mu^{-1}\mathbf{A}\left(\mathbf{A}^T\mathbf{R}_\mu^{-1}\mathbf{A}\right)^{-1}\mathbf{A}^T\mathbf{R}_\mu^{-1}\right]\left(\mathbf{F}_m \cdot \Delta\mathbf{m}\right) \tag{3.80}$$

It is easy to see that as the random term $\mathbf{w}_\mu$ appears only in the second term and in a linear way, the term $\Delta\Psi_{ML,c}\left(\Delta\mathbf{m}\right)$ is also a random Gaussian variable.

Individual ambiguity probability

It is well-known that for a random variable distributed as $\psi\ \mathcal{N}\left(\Updownarrow, \sigma^{\in}\right)$, we have,

$$p(\psi < 0) = Q\left(\frac{m}{\sigma}\right) \tag{3.81}$$

where function Q is defined as,

$$Q\left(t\right) = \frac{1}{\sqrt{2\pi}}\int_t^\infty e^{-\left(\frac{1}{2}\zeta^2\right)}d\zeta \tag{3.82}$$

Then, the ambiguity probability defined in (3.75) can be also expressed as,

$$p_{amb}\left(\Delta\mathbf{m}\right) = p\left(\Delta\Psi_{ML,c}\left(\Delta\mathbf{m}\right) < 0\right) \tag{3.83}$$

$$= Q\left(\frac{E[\Psi_{ML,c}\left(\mathbf{m} = \mathbf{m}_0 + \Delta\mathbf{m}\right)]}{E[\Psi_{ML,c}\left(\mathbf{m} = \mathbf{m}_0 + \Delta\mathbf{m}\right) - E[\Psi_{ML,c}\left(\mathbf{m} = \mathbf{m}_0 + \Delta\mathbf{m}\right)]]^2}\right) \tag{3.84}$$

where it can be shown that,

$$E[\Psi_{ML,c}\left(\mathbf{m} = \mathbf{m}_0 + \Delta\mathbf{m}\right)] = \Delta\mathbf{m}^T\mathbf{F}_m^T\left[\mathbf{R}_\mu^{-1} - \mathbf{R}_\mu^{-1}\mathbf{A}\left(\mathbf{A}^T\mathbf{R}_\mu^{-1}\mathbf{A}\right)^{-1}\mathbf{A}^T\mathbf{R}_\mu^{-1}\right]\mathbf{F}_m\Delta\mathbf{m} \tag{3.85}$$

$$E[\Psi_{ML,c}\left(\mathbf{m} = \mathbf{m}_0 + \Delta\mathbf{m}\right) - E[\Psi_{ML,c}\left(\mathbf{m} = \mathbf{m}_0 + \Delta\mathbf{m}\right)]]^2 = 4E[\Psi_{ML,c}\left(\mathbf{m} = \mathbf{m}_0 + \Delta\mathbf{m}\right)] \tag{3.86}$$

So, the final ambiguity error probability becomes,

$$p_{amb}\left(\Delta\mathbf{m}\right) = Q\left(\frac{\left\|\mathbf{R}_\mu'^{1/2}\mathbf{F}_m\Delta\mathbf{m}\right\|}{2}\right) \tag{3.87}$$

where,

$$\mathbf{R}_\mu' = \left[\mathbf{R}_\mu^{-1} - \mathbf{R}_\mu^{-1}\mathbf{A}\left(\mathbf{A}^T\mathbf{R}_\mu^{-1}\mathbf{A}\right)^{-1}\mathbf{A}^T\mathbf{R}_\mu^{-1}\right]^{-1} \tag{3.88}$$

Some conclusions about this expression (3.87) are:

- The term $\mathbf{F}_m\Delta\mathbf{m}$ shows the time-offsets produced by the ambiguity given a certain $\Delta\mathbf{m}$. This can be considered the time-offset that allows to detect that this is an ambiguity point and not the real spacecraft position.
- These time-offsets are "filtered" through the projection matrix $\mathbf{R}_\mu'^{-1/2}$. This is why these time-offsets are sometimes difficult to detect. The closer the result of $\mathbf{R}_\mu'^{-1/2}\mathbf{F}_m\Delta\mathbf{m}$ is to zero, so much difficult is ambiguity to detect.

Common ambiguity error probability

The previous subsection has shown the exact expression of ambiguity probability given an individual $\Delta\mathbf{m}$. Obviously, we are interested in the common ambiguity probability given a certain set of possible ambiguity points. This is not as simple as desired due to the fact that the individual probabilities are indeed correlated. Although the exact expression for the ambiguity probability can be found defining the non-ambiguity N-dimensional space for the values of $\mathbf{w}_\mu$, we will present now an upper bound in order to show some results in the simulations section. The exact expressions are really tedious and they will be not presented for clarity reasons.

The used upper bound consists in assuming independence between ambiguities. This can be also understood as the union bound of all individual ambiguity probabilities. The final expression of this approach can be formulated from (3.87) as,

$$p_{amb}\left(\Delta\mathbf{m}\right) = 1 - \sum_{\Delta\mathbf{m}\in[\Delta\mathbf{m}]_\Upsilon} Q\left(\frac{1}{2}\left\|\mathbf{R}_\mu'^{-1/2}\mathbf{F}_m\Delta\mathbf{m}\right\|\right) \tag{3.89}$$

Chapter 4

Stochastic Signal Model

The understanding of the signal model and the establishment of a useful notation to characterize the pulsar signal is the prior step to the formulation of algorithms and associated performance bounds. In this chapter, broadband and narrow-band models for pulsar signals are elaborated in terms of stochastic cyclo-stationary processes. Cyclo-stationarity refers to the periodic variation in the pulsar signal statistics, which completely captures the stable pulsating nature of the source. The complete scheme is shown in figure (4.1).

The following conventions shall be used for radio and X-ray pulsars:

- Radio Pulsars: signal processing for radio pulsars is all performed in baseband, after down-conversion from the filtered passband signal at the antenna output. Signals are represented in terms of the in-phase and in-quadrature components, $x_i(t)$ and $x_q(t)$ of the pulsar passband signal at the center frequency f_c. The pulsar passband signal is represented as $x(t) = x_i(t)\cos(2\pi f_c t) - x_q(t)\sin(2\pi f_c t) = \mathrm{Re}\left(b_x(t)e^{j2\pi f_c t}\right)$, with the baseband equivalent signal $b_x(t)$ corresponding to the receiver output and containing the in-phase and in-quadrature components expressed as $b_x(t) = x_i(t) + jx_q(t)$. This representation allows to reconstruct the original passband signal $x(t)$ and hence preserves all information of interest. The structure of the receiver is shown in figure (4.1).
- X-Ray Pulsars: due to the nature of the detector, only real number notation is necessary.

It will be shown that complete experimental information is not available to characterize the second-order statistics of the pulsar signal. To this purpose, a detailed study on the correlation matrix of the pulsar cyclo-stationary process has been carried out. This will lead later to reasonable simplifications in the evaluation of timing estimation algorithms based on the available experimental data.

The second part of this chapter considers, in lesser extension, X-ray pulsars. Similar analyses as found in the correlation matrix of radio-pulsars carry over to the cyclo-stationary emission probability of X-ray pulsars.

4.1 Broadband Model of the Pulsar Signal

We examine the experimental model of the pulsar signal and the theoretical model of cyclo-stationary processes used to match the experimental data.

4.1.1 Experimental Model

Physical measurements of pulsar signals have established the following features:

- Let $x(t)$ be the received noiseless pulsar signal, with $x(t)$ a cyclo-stationary[1] stochastic process in-

[1] cyclo-stationarity refers to the periodic variation of the signal statistics. As an example, for stationary processes, the autocorrelation function $r_{xx}(t,\tau) = Ex^*(t)x(t+\tau) = r_{xx}(\tau)$, is a function of the delay τ only, while for cyclo-stationary processes, $r_{xx}(t,\tau)$ depends on τ and is periodic in t. This will be developed henceforth in more detail.

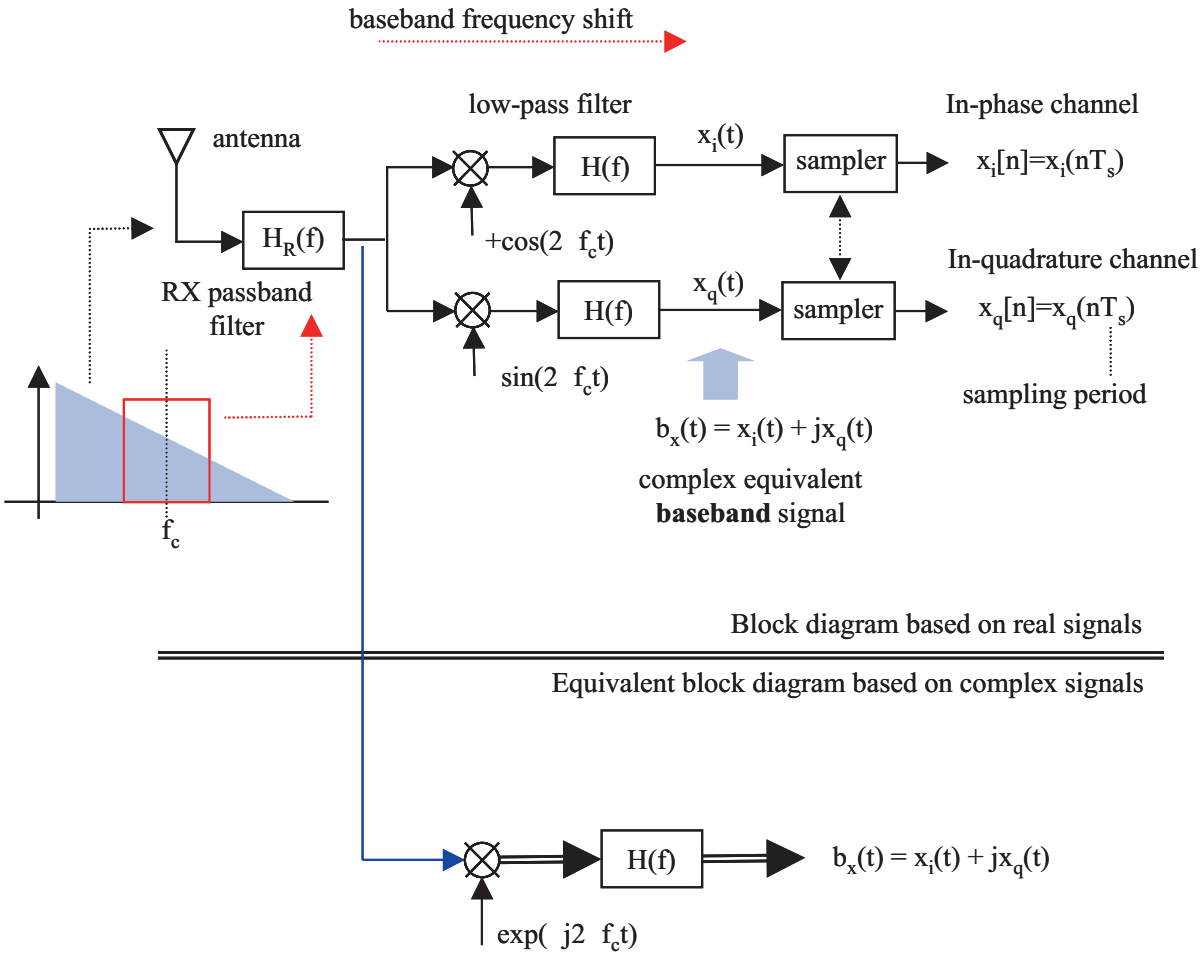

Figure 4.1: (Above) Depiction of the signal processing scheme for generating the in-phase and in-quadrature components of a passband radio signal at the central frequency f_c. (Below) Equivalent representation in complex notation as used in this report. This scheme, known as IQ-sampling, is conceptually useful as background for understanding the operation of the receiver. In a technological implementation, IF-sampling (not shown) would be used.

duced by the pulsar rotation. We will denote the inverse of this rotation frequency as the pulse repetition period (PRP). Frequencies associated with periodic variations of signal statistics are denoted cyclo-frequencies. At this stage, we are not yet considering effects such as slow-down or orbital perturbations on the pulsar signal. These effects will be incorporated later on as modifications to the cyclo-stationary model of $x(t)$.

Let T be the PRP. Then, each period $p_k(t) = x(t+kT)\Pi(t/T)$ describes[2] a broadband pulse so that $x(t)$ can be expressed as,

$$x(t) = \sum_{k=-\infty}^{+\infty} p_k(t - kT)$$

where each random $p_k(t)$ is constituted by sub-pulses. The mean power profile of $p_k(t)$, typically known as the pulsar pulse profile, is defined as,

$$\sigma_p^2(t) = E|x(t+kT)|^2 \cdot \Pi(t/T) \quad (4.1)$$

$$= E_{(k)}|p_k(t)|^2 \quad (4.2)$$

[2] $\Pi(t)$ is the unitary pulse: $\Pi(t) = 1$ in $|t| \leq \frac{1}{2}$ and $\Pi(t) = 0$ in $|t| > \frac{1}{2}$

The term $\sigma_p^2(t)$ depends on t but not on the index k due to the cyclo-stationary nature of the process. This is still defined on the noiseless broadband signal $x(t)$, rather than on the corresponding analyzed sub-band component.

- modifications to the model in (4.1.1) may be expressed as,

$$x(t) = \sum_{k=-\infty}^{+\infty} p_k(t - kT - \varrho(t))$$

with $\varrho(t)$ incorporating perturbations of whatever nature, as orbital motion. As only solitary pulsars are considered in this study, $\varrho(t)$ only incorporates slow-down and other effects.

- due to dispersion in the interstellar medium, the propagation channel introduces a delay at each component frequency defined as,

$$T(f) = T_\infty - D(r)f^{-2}$$

with $D(r)$ a dispersion constant depending on the distance r from the pulsar. After propagation and for each analyzed band of $x(t)$, the cyclo-stationary model is still valid. This effect will motivate later the consideration of a narrow-band model of the pulsar signal and multiband analysis, where $T(f)$ may be considered constant within each sub-band.

4.1.2 Generic Theoretical Model

The generic broadband model of the (real) pulsar signal is expressed as,

$$\begin{aligned} x(t) &= \sum_{k=-\infty}^{+\infty} a_k(t)e^{j2\pi k\alpha t} \\ r_{a,k,k'}(t, t+\tau) &= r_{a,k,k'}(\tau) = E\{a_{k'}(t+\tau)a_k^*(t)\} \end{aligned} \tag{4.3}$$

with $\{a_k(t)\}$ a set of jointly stationary correlated processes and $\alpha = 1/T$ the cycle frequency. Each $a_k(t)$ can be generated by spectral shaping of a white process $w_k(t)$, where the members of $\{w_k(t)\}$ are also jointly stationary correlated,

$$\begin{aligned} a_k(t) &= w_k(t) * h(t) \\ r_{w,k,k'}(t, t+\tau) &= r_{w,k,k'}(\tau) = E\{w_{k'}(t+\tau)w_k^*(t)\} \\ h(t) &= \alpha\frac{\sin(\pi\alpha t)}{\pi\alpha t} \\ H(f) &= \Pi(f/\alpha) \end{aligned} \tag{4.4}$$

The spectral shaping filter $H(f)$ is a frequency rectangular function common to all $w_k(t)$. The pulsar profile $\sigma_p^2(t)$ is determined by the set of correlation functions $\{r_{w,k,k'}(\tau)\}$.

4.2 Subband analysis of $x(t)$

We derive here the signal structure of a receiver tuned to a generic central frequency f_c which analyzes a given subband of the broadband signal $x(t)$. As a particular case, it will be shown how the $a_k(t)$ can be recovered from $x(t)$. The generation of the in-phase and in-quadrature components from a central frequency f_c of the analysis band is performed as,

$$b(t) = (x(t)e^{-j2\pi f_c t}) * g(t)$$

with $g(t)$ the impulse response of the analysis filter and $*$ the convolution operator. Then,

$$\begin{aligned} b(t) &= \int_{-\infty}^{+\infty} g(\tau)x(t-\tau)e^{-j2\pi f_c(t-\tau)}d\tau \\ &= \int_{-\infty}^{+\infty} g(\tau)e^{-j2\pi f_c(t-\tau)} \sum_{k=-\infty}^{+\infty} a_k(t-\tau)e^{j2\pi k\alpha(t-\tau)}d\tau \\ &= \sum_{k=-\infty}^{+\infty} e^{j2\pi(-f_c+k\alpha)t} \int_{-\infty}^{+\infty} \left(g(\tau)e^{-j2\pi(-f_c+k\alpha)\tau}\right) a_k(t-\tau)d\tau \\ &= \sum_{k=-\infty}^{+\infty} e^{j2\pi(-f_c+k\alpha)t} \cdot \left(g(t)e^{-j2\pi(-f_c+k\alpha)t}\right) * a_k(t) \end{aligned} \tag{4.5}$$

Now, setting $a_k(t) = w_k(t) * h(t)$, we have,

$$\begin{aligned} b(t) &= \sum_{k=-\infty}^{+\infty} b_k(t)e^{j2\pi(-f_c+k\alpha)t} \\ b_k(t) &= \left(g(t)e^{-j2\pi(-f_c+k\alpha)t}\right) * a_k(t) \\ &= \left(\left(g(t)e^{-j2\pi(-f_c+k\alpha)t}\right) * h(t)\right) * w_k(t) \\ &= h'(t) * w_k(t) \end{aligned} \tag{4.6}$$

which is stationary, where the filter $h'(t)$ has a frequency response $H'(f)$,

$$H'(f) = G(f - f_c + k\alpha)H(f) \tag{4.7}$$

Equation (4.5) expresses that, in general, $b(t)$ has components at frequencies $-f_c + k\alpha$. This expression provides the baseband signal structure observed by a receiver tuned to the central frequency f_c.

As a particular case, to proceed to show how the components $a_k(t)$ can be recovered: setting $f_c = k_c\alpha = k_c/T$ and $g(t) = h(t)$, we get,

$$H'(f) = \Pi^2(Tf)\delta_{k,k_c} \tag{4.8}$$

in terms of the Kronecker delta, which means that only a filtered version of the component of interest is recovered when $k = k_c$,

$$b(t) = b_{k_c}(t) = h(t) * a_{k_c}(t)$$

But as $\Pi^2(Tf) = \Pi(Tf)$, we have that $h(t) * h(t) = h(t)$. Hence,

$$b(t) = b_{k_c}(t) = h(t) * h(t) * w_{k_c}(t) = h(t) * w_{k_c}(t) = a_{k_c}(t)$$

4.2.1 Sampling

The analog signal $b(t)$ within the analysis band is sampled at the sampling frequency $f_s = 1/T_s$ to obtain the discrete time (quantized) signal $b[n]$,

$$b[n] = b(nT_s) \tag{4.9}$$

Oversampling is performed to avoid aliasing: $f_s \geq 2B$, with B the bandwidth of $b(t)$. The sampling procedure herein described corresponds to IQ sampling, but suffices for the feasibility analysis. IF sampling would be used in a real implementation.

4.3 Model of Correlation Matrix: Pulsar Signal

Synchronization algorithms (Phase and Pulse Arrival Time Drift (PATD) Estimation) for the pulsar signal $x(t)$ will be shown to require a model for the pulsar correlation matrix corresponding to different samples of $x(t)$. We will provide first a generic model for the correlation matrix of an analog cyclo-stationary vector process $\mathbf{x}(t)$, to be used for deriving the correlation matrix of the discrete (sampled) cyclo-stationary process $x[n] = x(nT_s)$, with T_s the sampling period. We will consider the case when the sampling frequency is a multiple of the cycle period T, and the case where due to the spacecraft speed, the sampling frequency is not a multiple of the cycle period.

4.3.1 Analog Fourier expansion of the correlation matrix

A Fourier model for the correlation matrix of a cyclo-stationary vector process is derived in this section. In accordance with the previous section, a cyclo-stationary vector process $\mathbf{x}(t)$ of cycle frequency α can be expressed from a set of stationary vector processes $\mathbf{a}_k(t)$ as,

$$\begin{aligned} \mathbf{x}(t) &= \sum_{k=-\infty}^{+\infty} \mathbf{a}_k(t) e^{j2\pi k\alpha t} \\ \mathbf{R}_{a,k,k',t,t+\tau} &= \mathbf{R}_{a,k,k',\tau} = E\{\mathbf{a}_{k'}(t+\tau)\mathbf{a}_k^{\mathrm{H}}(t)\} \end{aligned} \tag{4.10}$$

with $\mathbf{R}_{a,k,k',\tau}$ the corresponding correlation matrices. We construct the correlation matrix of the process,

$$\begin{aligned} \mathbf{R}_x(t) = E\{\mathbf{x}(t)\mathbf{x}^{\mathrm{H}}(t)\} &= E\sum_{k,k'} \mathbf{a}_{k'}(t)\mathbf{a}_k^{\mathrm{H}}(t) e^{j2\pi(k'-k)\alpha t} \\ &= \sum_{k,k'} \mathbf{R}_{a,k,k',0} e^{j2\pi(k'-k)\alpha t} \\ &= \sum_{l=-\infty}^{+\infty} e^{j2\pi l\alpha t} \sum_{k'-k=l} \mathbf{R}_{a,k,k',0} \\ &= \sum_{l=-\infty}^{+\infty} \mathbf{R}_{a_l} e^{j2\pi l\alpha t} \end{aligned} \tag{4.11}$$

$$\mathbf{R}_{a_l} = \sum_{k'-k=l} \mathbf{R}_{a,k,k',0} \tag{4.12}$$

In equation (4.11), matrices $\mathbf{R}_{a_l}$ are precisely the Fourier coefficients in the expansion of $\mathbf{R}_x(t)$ at the cycle frequency $l\alpha = l/T$,

$$\mathbf{R}_{a_l} = \frac{1}{T}\int_{-T/2}^{+T/2} \mathbf{R}_x(t) e^{-j2\pi l\alpha t} dt = \frac{1}{T}\mathcal{F}[\mathbf{R}_x(t)]_{f=l/T} \tag{4.13}$$

with $\mathcal{F}[\cdot]$ denoting the component-wise Fourier transform of the corresponding matrix.

4.3.2 Discrete Fourier expansion of the correlation matrix

When the analog complex baseband signal $x(t)$ is sampled at the frequency $f_s = 1/T_s$, with T_s the sampling period, a vector process $\mathbf{x}[n]$ can be defined by stacking N consecutive samples of $x(t)$ as,

$$\begin{aligned} \mathbf{x}(t) &= [x(t), x(t-T_s), \cdots, x(t-(N-1)T_s]^T \\ \mathbf{x}[n] &= \mathbf{x}(nT_s) \end{aligned} \tag{4.14}$$

Setting $\alpha = 1/T = 1/N_T T_s$, with N_T the number of samples per period (the length N of $\mathbf{x}[n]$ does not necessarily correspond to an integer number of periods), we get,

$$\mathbf{R}_x[n] = \sum_{l=-\infty}^{+\infty} \mathbf{R}_{a_l} e^{j2\pi l\frac{nT_s}{T}} = \sum_{l=-\infty}^{+\infty} \mathbf{R}_{a_l} e^{j2\pi\frac{n}{N_T}l} \tag{4.15}$$

Setting $l = l_1 N_T + l_2$, with $-\infty < l_1 < +\infty$ and $0 \leq l_2 \leq N_T - 1$, we get,

$$\begin{aligned}
\mathbf{R}_x[n] &= \sum_{l_2=0}^{N_T-1} \sum_{l_1=-\infty}^{+\infty} \mathbf{R}_{a_{l_1 N_T + l_2}} e^{j2\pi \frac{n}{N_T}(l_1 N_T + l_2)} \\
&= \sum_{l_2=0}^{N_T-1} \left(\sum_{l_1=-\infty}^{+\infty} \mathbf{R}_{a_{l_1 N_T + l_2}} \right) e^{j2\pi \frac{n}{N_T} l_2} \\
&= \sum_{l_2=0}^{N_T-1} \mathbf{R}_a[l_2] e^{j2\pi \frac{n}{N_T} l_2} \\
\mathbf{R}_a[l_2] &= \sum_{l_1=-\infty}^{+\infty} \mathbf{R}_{a_{l_1 N_T + l_2}}
\end{aligned} \tag{4.16}$$

Therefore, once the process has been sampled, only a finite number of terms is required to express $\mathbf{R}_x[n]$. The matrices $\mathbf{R}_a[l_2]$ can be obtained from $\mathbf{R}_x[n]$ using the Discrete Fourier Transform (DFT) as,

$$\mathbf{R}_a[l_2] = \frac{1}{N} \sum_{n=0}^{N-1} \mathbf{R}_x[n] e^{-j2\pi \frac{l_2}{N} n}$$

which is applied component-wise on the matrix elements.

4.3.3 Detailed structure of the discrete correlation matrix

The detailed structure of the correlation matrix for the broadband signal cannot be completely determined from the available experimental data. Traditionally, radio-astronomy measurements have only provided information on the average power profile of the pulsar signal and on its average spectral power density ratio. These measurements, which have been performed via sub-band analysis of the pulsar signal, are envelope-based measurements. The envelope of a passband signal of a given bandwidth, $e(t)$, is defined as the modulus of the equivalent baseband signal: $e^2(t) = x_i^2(t) + x_q^2(t) = |b_x(t)|^2$, in terms of its in-phase and in-quadrature components $x_i(t)$ and $x_q(t)$. As we have seen, complete characterization of the correlation matrix requires evaluation of expectations of the type $E\{b_x(t+\tau)b_x^*(t)\}$, which are not available. The approach taken in the timing estimation chapter consists of modeling correlation matrices as diagonal matrices. This is reasonable if the examined bandwidth is sufficiently narrow to guarantee that the spectral power density is approximately constant. Variations in the spectral power density within the band of interest always appear as off-diagonal terms in the correlation matrix of the process. The procedure to extrapolate results when processing wider bands is justified later in the timing estimation chapter (see section (5.1.7)). Under these conditions, the correlation matrix $\mathbf{R}_x[n]$ and its spectral coefficient matrices $\mathbf{R}_a[l_2]$ in equation (4.3.2), become diagonal when considering a narrow-band sub-channel of the pulsar signal. In particular, the diagonal coefficients of $\mathbf{R}_x[n]$ correspond to correlative samples of the average power profile $\sigma_p^2(t)$.

4.3.4 Conclusions

Apparently, it seems that not enough experimental data is available to establish the broadband cyclostationary model of the pulsar signal. Hence, we will try to assess synchonization algorithms in the presence of imperfect knowledge of the signal model (full characterization of the signal model would lead to increased performance). In spite of this, for multiband processing, the pulsar spectral variation may be considered negligible within each subband, so that the subband correlation matrix is approximately diagonal. This fact will be used in the assessment of timing algorithms.

4.4 Model of the Noise Correlation Matrix

4.4.1 System Noise

The correlation matrix of Gaussian system noise can be inferred from the system temperature provided in the previous chapter. A non-uniform trend in frequency is expressed as off-diagonal terms in the correlation matrix of the noise. For the considered central frequency and bandwidth, 1 GHz and 200 MHz respectively, it is reasonable to assume that system noise is white (its correlation matrix is diagonal). This will lead to simplifications in the timing estimation algorithms.

4.4.2 Solar and Jovian Radiation

The Sun and Jupiter constitute strong sources of RF interference, which further degrade reception SNR through antenna sidelobes. The level of interference is dependent on the location within the solar system, so that in the vicinity of the sources the receiver is expected to enter a 'blind' region in terms of positioning. This type of interference points to the need of a multibeam antenna capable of adaptive sidelobe cancellation. In a more detailed study location algorithms should be extended to spatial processing. This study will solely provide the degradation SNR expected from both sources in terms of distance. A suitable dB margin will be considered to account for residual Solar/Jovian RF interference after cancellation, so that overall system noise is still considered white for the band of interest.

4.5 Signal Model for X-Ray Pulsars

X-Ray pulsars are characterized by a cyclo-stationary probability of emission. The nature of the received signal is expressed in terms of a Poisson point process as described in the following sections. The cyclo-stationary characterization of the Poisson process is dealt with in the chapter on timing estimation for X-ray pulsars.

4.5.1 Poisson Point Processes

A stationary Poisson point process is characterized by its mean event density as,

$$\lambda = \lim_{T \to \infty} \frac{n(T)}{T}$$

with T the observation time and $n(T)$ the number of events in T. The event duration is always assumed to be zero. The addition of two independent Poisson point processes (X-Ray pulsar single photon arrival and Galaxy X-Ray Background) has an equivalent arrival density $\lambda = \lambda_p + \lambda_n$. In an ideal setting, each event (Poisson point) has zero duration. The time resolution of the X-Ray detector is such that if more than one photon arrives within a given time-bin, it is detected as a single photon.

The probability that k Poisson points occur in an interval of time T_b is provided by the relationship,

$$\Pr(k) = \frac{(\lambda T_b)^k}{k!} \cdot e^{-\lambda T_b}$$

Hence, we have to distinguish two cases:

1. no photon has arrived in a given time-bin of duration T_b
2. more than one photon has arrived in the given time-bin.

The respective probabilities are,

$$\mathrm{P}_0 = e^{-\lambda T_b} \tag{4.17}$$

$$\mathrm{P}_1 = 1 - e^{-\lambda T_b} \tag{4.18}$$

Depending on λ, a sufficiently low T_b has to be considered not to saturate the detector. In our case, the arrival density λ is cyclic: $\lambda \to \lambda(\tau)$.

4.5.2 X-Ray detector description

X-Ray sources have a photon arrival time density spectrum in terms of the frequency ν/energy ϵ of individual photons: $\epsilon = h\nu$, with h Planck's constant. Either of the following definitions is possible, although the latter is commoner,

$$S_\lambda(\nu) = \frac{d\lambda}{d\nu} \qquad , \qquad S_\lambda(\epsilon) = \frac{d\lambda}{d\epsilon}$$

The X-ray detector is tuned to a given band (measured in KeV), so that the photons arrival density is evaluated as,

$$\lambda = \int_{\epsilon_c - E/2}^{\epsilon_c + E/2} S_\lambda(\epsilon) d\epsilon$$

around a central energy ϵ_c and an energy bandwidth E. Photon counting is performed using a time base of resolution T_b. Therefore, T_b has to be sufficiently low so that the detector is not saturated. Typically, $T_b\lambda < \ln P_{0,\mathrm{th}}^{-1}$, with $P_{0,\mathrm{th}}$ a suitable threshold probability of non-event (not to saturate the detector: a photon is always detected). In its turn, $S_\lambda(\epsilon)$ can be obtained in terms of a directional density per solid angle as,

$$S_\lambda(\epsilon) = \int_{4\pi} S_\lambda(\epsilon, \theta, \phi) F(\theta, \phi) d\Omega \tag{4.19}$$

with $F(\theta, \phi)$ modeling the focalization properties of the X-ray detector. In establishing the photon arrival density spectrum of the pulsar and the X-ray background, the pulsar is considered a point source with,

$$S_\lambda(\epsilon, \theta, \phi) = \Lambda(\epsilon)\delta(\theta - \theta_p)\delta(\phi - \phi_p)$$

with (θ_p, ϕ_p) the angular coordinates of the pulsar and $\delta(\cdot)$ Dirac's delta. On the contrary, the X-ray background is considered a distributed source with a continuous $S_\lambda(\epsilon, \theta, \phi)$ (in fact, a spatial distribution of point sources).

Chapter 5

Timing Estimation for Radio Pulsars

This section analyzes synchronization algorithms and associated performance bounds for radio pulsars. Phase or Time-of-Arrival (TOA) estimation and Doppler or Pulse Arrival Time Drift (PATD) estimation are considered. The low signal-to-noise-ratio (low-SNR) regime is assumed to be consistent with the small antenna assumption: increasingly larger antennas can boost the reception SNR but are not feasible for location on small to medium-sized spacecraft. In this low-SNR regime, it is found that the performance of algorithms is controlled solely by the second order statistics (correlation matrix) of the pulsar signal, which can be (partially) inferred from experimental results. Hence, the average power profile within the pulsar period is used as the only available information on the signal of interest. Noise appears as the dominant factor of degradation of timing estimates, so that for small antennas, a large bandwidth and a long observation time (many pulsar periods) are necessary to recover useful timing information. Knowledge on the micro-structure of individual pulsar pulses, which averaged constitute the power profile, is not necessary in the low-SNR regime, as it is related with statistics of order higher than two. Only for large antennas does this micro-structure constitute a factor of importance in the evaluation of the timing error, which adds to the effect of additive noise (less important for large antennas). The equations derived in this chapter are not applicable therefore for large antennas. Rather, they are optimistic as they do not consider the timing jitter of individual pulsar pulses, irrelevant in the low-SNR regime. In general, it is found that algorithms and performance bounds for the high-SNR regime are mathematically more complex to analyze.

5.1 TOA Estimation

This section applies the Maximum Likelihood (ML) Criterion[1] to the estimation of the pulsar TOA. We assume that the signal model is a cyclo-stationary signal immersed in Gaussian noise. In a first simplified approximation, the following considerations are made:

- both polarizations of the pulsar signal are sampled in a given bandwidth at an integer number of samples per period. Processing both polarizations is necessary as pulsars are polarized.
- the pulse repetition period (PRP) is assumed known.
- the 2nd order statistics, or average power profile, of the sampled pulsar signal is assumed known. Partial knowlege results in some performance degradation, adding to the loss budget.
- the signal to noise power ratio is very low (small antenna assumption). As will be shown, this only requires knowledge of the second order statistics of the signal of interest.
- only one pulsar signal is present. It is assumed that other pulsars are equivalent to noise as synchronous averaging is done for the pulsar of interest.

[1] The ML criterion was already introduced in the geometry chapter for the linear case, where measurements and parameters are related through a linear equation. In the timing estimation case, the relationship is non-linear, which complicates the analysis and introduces degradations at very low signal-to-noise ratios.

- the acquisition regime (no prior knowledge on parameters) is assumed.

It is assumed that all sampled data is stacked into vector $\mathbf{x}$, optionally using the upper and lower halves for each polarization, and each half including all periods of the pulsar signal in a given time span. Then, the signal model can be expressed as,

$$\mathbf{x} = \mathbf{p} + \mathbf{n} \qquad \begin{aligned} \mathbf{R}_x &= E\{\mathbf{x}\mathbf{x}^{\mathrm{H}}\} \\ \mathbf{R}_p(\tau) &= E\{\mathbf{p}\mathbf{p}^{\mathrm{H}}\} \\ \mathbf{R}_n &= E\{\mathbf{n}\mathbf{n}^{\mathrm{H}}\} \end{aligned} \qquad \mathbf{R}_x(\tau) = \mathbf{R}_p(\tau) + \mathbf{R}_n \tag{5.1}$$

with $\mathbf{p}$ and $\mathbf{n}$ the pulsar and noise vectors, $\mathbf{R}_p(\tau)$ the cyclic autocorrelation matrix of the pulsar signal vector and $\mathbf{R}_n$ the stationary autocorrelation matrix of the noise vector.

The data vector $\mathbf{x}$ may contain:

- one, or both polarizations. In the latter case, $\mathbf{x}^T = [\mathbf{x}_1^T, \mathbf{x}_2^T]^T$, with $\mathbf{x}_i$ the vector containing samples of one polarization.
- a wideband signal sampled at a high sampling frequency, or sub-vectors corresponding to several sub-bands of the pulsar signal. In the first case, it should be taken into account that the pulse profile has experimented interstellar dispersion and is broader than when observed in smaller bands. In the latter case, $\mathbf{x}^T = [\mathbf{x}_1^T, \mathbf{x}_2^T, \cdots, \mathbf{x}_{N_c}^T]^T$, with $\mathbf{x}_i$ the vector containing samples of one out of N_c non-overlapping channels.

In the first sections of this chapter, it will be assumed that a channel of sufficiently narrow bandwidth (in terms of variations of the spectral power density and negligible interstellar dispersion) is processed. Extension to larger bandwidths and consideration of interstellar dispersion will be considered later.

5.1.1 Establishment of Performance Bounds

It is known that the ML criterion asymptotically (for large data records) approaches the performance of the Minimum Variance Unbiased Estimator[2] of a parameter vector. A bound to the variance of the ML parameter estimates, the Cramér-Rao Lower Bound (CRLB), is the inverse of the Fisher Information matrix, which is achieved in the small error region (high SNR). For a fixed data record length, and when the signal to noise power ratio (SNR) decreases, the variance of the ML estimates departs from the performance predicted by the CRLB (threshold effect). Tighter bounds, as Barankin's Bound (BB), exist for the low-SNR region, but are computationally expensive and difficult to derive. Barankin's Bound is reachable (there exists an estimator whose performance matches BB) and constitutes the largest reachable lower bound to the variance of unbiased estimators.

Provided that the data record length is sufficiently long, the CRLB will be a close measure to the true performance, and the parameter estimates will be Gaussian distributed with correlation matrix equal to the CRLB. The asymptotic Gaussianity of the estimates justifies the assumption of Gaussian phase noise adopted for location algorithms in the geometry chapter. A criterion to establish for a given data record length L or SNR if the CRLB is tight or not, i.e. the evaluation of the corresponding L or SNR threshold, is of interest and has also been addressed in this chapter.

5.1.2 Statistical Characterization of the Pulsar Signal

For the formulation of the ML criterion, the exact statistical characterization of the pulsar signal is required. At this point, two possibilities arise:

- the pulsar signal is Gaussian with cyclic statistics. This may seem reasonable but to our knowledge it has not been experimentally verified. In this case, the likelihood function of the data is expressed as,

$$p(\mathbf{x}|\tau) = \frac{1}{\pi^L \det\left(\mathbf{R}_n + \mathbf{R}_p(\tau)\right)} e^{-\mathbf{x}^{\mathrm{H}}(\mathbf{R}_n + \mathbf{R}_p(\tau))^{-1}\mathbf{x}}$$

[2] An estimator $\hat{\theta}(\mathbf{x})$ of a parameter θ operating on the data vector $\mathbf{x}$ is unbiased when its expectation fulfils $E_{\mathbf{x}}\hat{\theta}(\mathbf{x}) = \theta$. The estimator is of minimum variance when all other unbiased estimators $\hat{\theta}'$ fulfil that $E_{\mathbf{x}}|\hat{\theta}'(\mathbf{x}) - \theta|^2 \geq E_{\mathbf{x}}|\hat{\theta}_{\mathrm{MV}}(\mathbf{x}) - \theta|^2$

- the pulsar signal is non-Gaussian with cyclic statistics. In this case, we will apply a more robust approach: the low-SNR ML approximation.

We show that similar results in terms of the covariance of the timing estimates are found in both cases, so that the Gaussian assumption for the pulsar signal is not critical at low SNR. Hence, when more convenient, the Gaussian assumption has been used in deriving some results.

5.1.3 Cyclic Gaussian case

The ML estimate is produced by maximizing the probability density function of the signal conditioned on the unknown parameters and evaluated at the current data vector $\mathbf{x}$. The ML estimator for the Gaussian case can be obtained as the following maximization,

$$\begin{aligned} \hat{\tau} &= \text{argmax}_{\tau} \quad \ln p(\mathbf{x}|\tau) \\ &= \text{argmin}_{\tau} \quad \ln\det\left(\mathbf{R}_n + \mathbf{R}_p(\tau)\right) + \mathbf{x}^{\mathrm{H}}\left(\mathbf{R}_n + \mathbf{R}_p(\tau)\right)^{-1}\mathbf{x} \end{aligned} \tag{5.2}$$

In the previous equation, we can distinguish two cases:

- true ML estimate: the data vector $\mathbf{x}$ is fixed and a value of τ is sought to minimize the previous expression.
- running ML estimate: the model variable τ is fixed and the data vector $\mathbf{x}$ is time-shifted according to a delay variable τ'. In this case, only the second term is necessary.

Only true ML estimates are analyzed in this report, for which the Cramer-Rao bound applies. Note in the previous equation that the first term is specific to the Gaussian statistics and is independent of τ, while the second term alone can be considered itself an ML estimator $\tilde{\tau}$ such that,

$$\tilde{\tau} = \text{argmin}_{\tau} \quad Z(\mathbf{x}|\tau) = \mathbf{x}^{\mathrm{H}}\left(\mathbf{R}_n + \mathbf{R}_p(\tau)\right)^{-1}\mathbf{x}$$

We are not considering power estimation. If this were the case, the first term should be incorporated into the ML formulation.

Cramér-Rao Lower Bound

We provide a general expression for the Cramér-Rao Lower Bound (CRLB) in the low-SNR range, where τ_s refers to time units in samples,

$$\begin{aligned} \text{CRLB}(\tau_s) &= \frac{1}{E_{\mathbf{x}}\left|\nabla_{\tau_s}\ln p(\mathbf{x}|\tau_s)\right|^2} = \frac{-1}{E_{\mathbf{x}}\nabla^2_{\tau_s}\ln p(\mathbf{x}|\tau_s)} \\ &= \frac{1}{\text{tr}\left(\left(\mathbf{R}_x^{-1}(\tau_s)\cdot\nabla_{\tau_s}\mathbf{R}_p(\tau_s)\right)^2\right)} \end{aligned} \tag{5.3}$$

where the trace operator[3] is used. It should be understood that the previous expression is evaluated at the true parameter. In this case we will assume that the correlation matrix of the data is perfectly known except for the true delay τ_s'. Otherwise, noise power and pulsar power should also be incorporated into the estimation procedure. This might be of interest in more refined procedures where the pulsar signal is subject to slow power variations. For a sufficiently narrow channel, the correlation matrix of the pulsar signal, $\mathbf{R}_p(\tau_s)$, can be assumed diagonal, with diagonal elements delayed sampled versions of the average power profile $\sigma_p^2(t)$,

$$[\mathbf{R}_p(\tau_s = n)]_{k,k'} = \sigma_p^2((n-k)T_s)\cdot\delta(k-k') \tag{5.4}$$

with $\delta(\cdot)$ Kronecker's delta. To derive a more specific expression for the CRLB, we introduce now the cyclic model of the correlation matrix into the calculations,

$$\mathbf{R}_p(\tau_s) = \sum_{k=0}^{N_T-1}\mathbf{R}_A[k]e^{j2\pi\frac{k}{N_T}\tau_s} \tag{5.5}$$

[3]The following property is used: $\mathbf{a}^T\mathbf{B}\mathbf{c} = \text{tr}(\mathbf{B}\mathbf{c}\mathbf{a}^T)$, with $\mathbf{a}$ and $\mathbf{c}$ vectors and $\mathbf{B}$ a matrix.

where the Fourier matrix coefficients are $\mathbf{R}_A[k] = S[k]\mathbf{D}^k$, with $\mathbf{D}$ a diagonal matrix of components $[\mathbf{D}]_{i,i} = e^{-j2\pi\frac{i}{N_T}}$ corresponding to the frequency-domain equivalent of the delay operation of each element in the diagonal of $\mathbf{R}_p(\tau_s)$, and $S[k]$ the discrete Fourier transform coefficients of the sampled power profile $\sigma_p^2(t)$.

An approximate computation of the CRLB for the low-SNR range and white noise case $\mathbf{R}_n = \sigma_n^2\mathbf{I}$ yields,

$$\begin{aligned}
\mathrm{tr}\left(\left(\mathbf{R}_x^{-1}\nabla_\tau\mathbf{R}_p(\tau)\right)^2\right) &\simeq \mathrm{tr}\left(\left(\mathbf{R}_n^{-1}\nabla_\tau\mathbf{R}_p(\tau)\right)^2\right) \\
&= \sum_{k,k'}\mathrm{tr}\left(\mathbf{R}_n^{-1}\mathbf{R}_A[k]\mathbf{R}_n^{-1}\mathbf{R}_A[k']\right)\left(-4\pi^2\frac{k\cdot k'}{N_T^2}\right)e^{j2\pi\frac{k+k'}{N_T}\tau} \\
&= \sum_{k,k'}\frac{1}{\sigma_n^4}S[k]S[k']\mathrm{tr}\left(\mathbf{D}^{k+k'}\right)\left(-4\pi^2\frac{k\cdot k'}{N_T^2}\right)e^{j2\pi\frac{k+k'}{N_T}\tau} \\
&= \sum_{k,k'}\frac{L}{\sigma_n^4}S[k]S[k']\delta[k+k']\left(-4\pi^2\frac{k\cdot k'}{N_T^2}\right)e^{j2\pi\frac{k+k'}{N_T}\tau} \\
&= \frac{L}{\sigma_n^4}\sum_k S[k]S[-k]4\pi^2\frac{k^2}{N_T^2} \qquad (5.6)
\end{aligned}$$

where the notation $\sum_k$ is over the interval $-\frac{1}{2}N_T \le k < \frac{1}{2}N_T$. As $S[k]S[-k] = |S[k]|^2$, we finally get the CRLB,

$$\mathrm{CRLB}(\tau_s) \simeq \frac{1}{4\pi^2 L}\frac{\sigma_n^4}{\frac{1}{N_T^2}\sum_k |S[k]|^2k^2} \qquad (5.7)$$

A slight modification in terms of previously introduced parameters yields,

$$\mathrm{CRLB}(\tau_s) \simeq \frac{1}{4\pi^2 T_o B}\left(\frac{\sigma_n^2}{\sigma_{p,T}^2}\right)^2\gamma_p^2 \qquad (5.8)$$

$$\gamma_p^2 = \frac{\sigma_{p,T}^4}{\frac{1}{N_T^2}\sum_k |S[k]|^2k^2} = \frac{1}{\sum_k\left|\frac{S[k]}{S[0]}\right|^2\frac{k^2}{N_T^2}} \qquad (5.9)$$

with γ_p a shape factor of the pulsar pulse, independent of its power, and $\sigma_{p,T}^2$ the average power over the pulsar period. The number of samples L can be expressed from the observation time T_o and bandwidth B as $L = T_oB$. We have used the property,

$$\begin{aligned}
S[0] &= \sigma_{p,T}^2 = \frac{1}{N_T}\sum_k\sigma_p^2[k] \\
\sigma_p^2[k] &= [\mathbf{R}_p(k)]_{1,1} \qquad (5.10)
\end{aligned}$$

The usefulness of equation (5.9) will be clear later when establishing the equivalence with the CRLB at low SNR for a non-Gaussian pulsar statistic. An expression to the CRLB more related to the pulsar database parameters is established in the following section.

The CRLB and the Pulsar Quality Factor

In this section, we will define a quality factor to measure the goodness of a given pulsar in terms of the equivalent positioning error, which corresponds to the previous $Q(f)$ plots found in the Pulsar Chapter. This quality measure is dependent on the exact power profile of the pulsar. As a simplified model is taken for this profile, the quality factor results we derive should be considered an approximation to the true value. To this purpose, we will assume an approximate pulsar profile $\sigma_p^2(t)$ in terms of the parameters

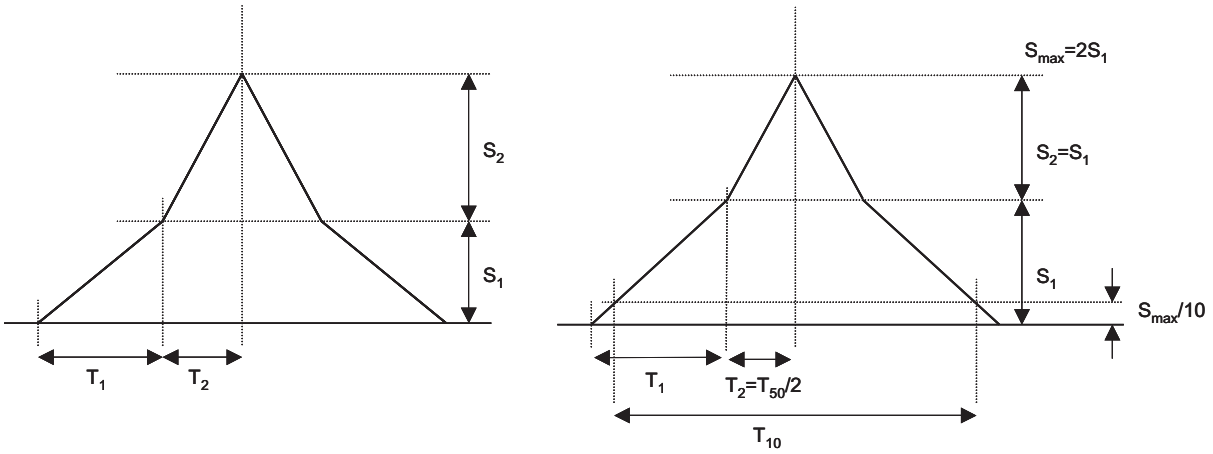

Figure 5.1: Definition of the pulsar profile.

available in the database (see figure): the pulse durations at 10 % and 50 % peak intensities, respectively. The expression of the CRLB is valid for the low-SNR range where $\sigma_n^2 >> \sigma_p^2(t)$,

$$\begin{aligned} \mathrm{tr}\left(\left(\mathbf{R}_x^{-1}(\tau)\cdot\nabla_\tau\mathbf{R}_p(\tau)\right)^2\right) &\simeq \sum_{i=0}^{N_I N_T-1}\left(\frac{\nabla_t\sigma_p^2(t)}{\sigma_n^2}\right)^2_{t=iT_s} \\ &= N_I\frac{1}{\sigma_n^4}2\left(\left(\frac{S_1}{T_1}\right)^2 N_1+\left(\frac{S_2}{T_2}\right)^2 N_2\right) \end{aligned} \tag{5.11}$$

where $N_1 = T_1/T_s = T_1 B$ is the number of samples in T_1 and $T_s = 1/f_s = 1/B$ is the sampling period or inverse of the sampling bandwidth B. Then, using $N_I = T_o/T$, with T_o the observation time and T the pulsar period, the expression for the CRLB becomes,

$$\mathrm{CRLB}^{-1}(\tau) = \frac{2T_oB}{T\sigma_n^4}\left(\frac{S_1^2}{T_1}+\frac{S_2^2}{T_2}\right) \tag{5.12}$$

Finally, the CRLB can be expressed as,

$$\mathrm{CRLB}(\tau) = \frac{1/2}{T_oB}\left(\frac{\sigma_n^2}{\sigma_p^2}\right)^2\cdot T\frac{\sigma_p^4}{\frac{S_1^2}{T_1}+\frac{S_2^2}{T_2}} \tag{5.13}$$

Now, according to the definitions of the pulsar database, we set $T_1 = \frac{5}{8}(T_{10}-T_{50})$ and $T_2 = \frac{1}{2}T_{50}$, and $S_1 = S_2$,

$$\begin{aligned} \mathrm{CRLB}(\tau) &= \frac{1/2}{T_oB}\left(\frac{\sigma_n^2}{\sigma_p^2}\right)^2\cdot TT_{\mathrm{ef}}\frac{\sigma_p^4}{S_1^2} \\ T_{\mathrm{ef}} &= \frac{1}{T_1^{-1}+T_2^{-1}} \end{aligned} \tag{5.14}$$

As $2S_1$ is the peak intensity, its relationship with σ_p^2 (average over the pulse duration) and $\sigma_{p,T}^2$ (average over the pulsar period) is,

$$\sigma_p^2 = \frac{S_1T_1+2S_1T_2+S_2T_2}{2T_1+2T_2} \tag{5.15}$$

$$\sigma_{p,T}^2 = \sigma_p^2\cdot\frac{2T_1+2T_2}{T} = \sigma_p^2\cdot\frac{T_p}{T} \tag{5.16}$$

with $T_p = 2T_1 + 2T_2$ the complete pulse duration,

$$T_p = \frac{1}{4}(5T_{10} - T_{50})$$

Hence, for $S_1 = S_2$, the term σ_p^4/S_1^2 becomes,

$$\frac{\sigma_p^4}{S_1^2} = \left(\frac{T_1 + 3T_2}{2T_1 + 2T_2}\right)^2 \tag{5.17}$$

Finally, as $L = T_o B$ is the number of processed samples in an observation window T_o and bandwidth B. The CRLB can be defined in terms of the per-sample CRLB, $\mathrm{CRLB_s}(\tau)$, as,

$$\begin{aligned} \mathrm{CRLB}(\tau) &= \frac{1}{T_o B}\mathrm{CRLB_s}(\tau) \\ \mathrm{CRLB_s}(\tau) &= \frac{1}{2}\left(\frac{\sigma_n^2}{\sigma_p^2}\right)^2 \cdot T T_{\mathrm{ef}} \frac{\sigma_p^4}{S_1^2} \end{aligned} \tag{5.18}$$

and pulsars can be selected according to the quality factor $Q_s = \sqrt{\mathrm{CRLB_s^{-1}}(\tau)}$. For the parameters provided in the pulsar data-base, we get,

$$\log_{10} Q = \frac{\sigma_p^2}{\sigma_n^2}\Big|_{\mathrm{dB}} \cdot \frac{1}{10} + \frac{1}{2}\log_{10}\frac{1}{T T_{\mathrm{ef}}} + \log_{10}\frac{S_1\sqrt{2}}{\sigma_p^2}$$

$$\frac{1}{T T_{\mathrm{ef}}} = \frac{1}{T}\left(\frac{8/5}{T_{10} - T_{50}} + \frac{2}{T_{50}}\right) \tag{5.19}$$

$$\frac{S_1}{\sigma_p^2} = 2 \cdot \frac{5T_{10} - T_{50}}{5T_{10} + 7T_{50}} \tag{5.20}$$

or, in terms of the average pulsar power,

$$\log_{10} Q = \frac{\sigma_{p,T}^2}{\sigma_n^2}\Big|_{\mathrm{dB}} \cdot \frac{1}{10} + \log_{10}\frac{\sqrt{T/T_{\mathrm{ef}}}}{T_p} + \log_{10}\frac{S_1\sqrt{2}}{\sigma_p^2} \tag{5.21}$$

It has been found more useful to refer the quality factor to the position error normalized to $\sigma_x = 10^6$ m. for $L = 10^9$ samples. Then,

$$Q = Q_s \frac{\sigma_x\sqrt{L}}{c} \tag{5.22}$$

The resulting expression is that which appeared in the Pulsar Database chapter.

The definition of this quality factor is asymptotically valid for large values of L, when the CRLB applies and the timing error is practically unbiased and Gaussian distributed. Hence, for any L or SNR, position accuracy results obtained from Q shall have to be checked for compliance with the threshold. The procedure is examined later in the Performance Evaluation section.

5.1.4 Cyclic non-Gaussian case

In the non-Gaussian case, we will derive an estimator independent from the statistics of the pulsar signal. It will be shown that at low SNR, results are equivalent to the assumption of Gaussian statistics for the pulsar, requiring statistical moments only up to second order. The likelihood function of the data $\mathbf{x}$ conditioned on the pulsar signal and the unknown phase can be expressed as,

$$p(\mathbf{x}|\tau, \mathbf{p}) = \frac{1}{\pi^L \det\mathbf{R}_n} e^{-(\mathbf{x}-\mathbf{p})^{\mathrm{H}}\mathbf{R}_n^{-1}(\mathbf{x}-\mathbf{p})}$$

In this application, the pulsar signal is unknown but not its statistics. Therefore, the likelihood function is modified to,

$$p(\mathbf{x}|\tau) = E_{\mathbf{p}} p(\mathbf{x}|\tau, \mathbf{p}) = \frac{1}{\pi^L \det \mathbf{R}_n} E_{\mathbf{p}} e^{-(\mathbf{x}-\mathbf{p})^{\mathrm{H}} \mathbf{R}_n^{-1} (\mathbf{x}-\mathbf{p})}$$

in terms of $E_{\mathbf{p}}$, the expectation with respect to the pulsar signal. Now, the low-SNR assumption is applied up to second order,

$$\begin{aligned} p(\mathbf{x}|\tau) &\simeq \frac{1}{\pi^L \det \mathbf{R}_n} E_{\mathbf{p}} \left(f(\mathbf{x}) - \nabla_{\mathbf{x}} f(\mathbf{x}) \cdot \mathbf{p} - \mathbf{p}^{\mathrm{H}} \nabla_{\mathbf{x}^{\mathrm{H}}} f(\mathbf{x}) + \mathbf{p}^{\mathrm{H}} \cdot \nabla_{\mathbf{x}^{\mathrm{H}}} \nabla_{\mathbf{x}} f(\mathbf{x}) \cdot \mathbf{p} \right) \quad (5.23) \\ f(\mathbf{x}) &= e^{-\mathbf{x}^{\mathrm{H}} \mathbf{R}_n^{-1} \mathbf{x}} \\ \nabla_{\mathbf{x}} f(\mathbf{x}) &= -e^{-\mathbf{x}^{\mathrm{H}} \mathbf{R}_n^{-1} \mathbf{x}} \cdot \mathbf{x}^{\mathrm{H}} \mathbf{R}_n^{-1} \\ \nabla_{\mathbf{x}^{\mathrm{H}}} \nabla_{\mathbf{x}} f(\mathbf{x}) &= e^{-\mathbf{x}^{\mathrm{H}} \mathbf{R}_n^{-1} \mathbf{x}} \cdot \left(\mathbf{R}_n^{-1} \mathbf{x} \mathbf{x}^{\mathrm{H}} \mathbf{R}_n^{-1} - \mathbf{R}_n^{-1} \right) \quad (5.24) \end{aligned}$$

Hence,

$$\begin{aligned} p_2(\mathbf{x}|\tau) &= \frac{1}{\pi^L \det \mathbf{R}_n} e^{-\mathbf{x}^{\mathrm{H}} \mathbf{R}_n^{-1} \mathbf{x}} \cdot M(\mathbf{x}|\tau) \simeq p(\mathbf{x}|\tau) \\ M(\mathbf{x}|\tau) &= 1 - \mathrm{tr}\left(\mathbf{R}_n^{-1} \mathbf{R}_p(\tau) \right) + \mathbf{x}^{\mathrm{H}} \mathbf{R}_n^{-1} \mathbf{R}_p(\tau) \mathbf{R}_n^{-1} \mathbf{x} \quad (5.25) \end{aligned}$$

as $E_{\mathbf{p}} \mathbf{p} = \mathbf{0}$. If the other parameters are known, $M(\mathbf{x}|\tau)$ has to be maximized. Note that the term $\mathrm{tr}\left(\mathbf{R}_n^{-1} \mathbf{R}_p(\tau) \right)$ does not depend on τ for a cyclic model of $\mathbf{R}_p(\tau)$ (assuming $\mathbf{R}_p(\tau)$ diagonal and white noise). To prove this, we consider $L \times L$-matrices, with $L = N_T N_I$.

$$\begin{aligned} \mathbf{R}_p(\tau) &= \sum_{k=0}^{N_T-1} \mathbf{R}_A[k] e^{j2\pi \frac{k}{N_T} \tau} \\ \mathrm{tr}\left(\mathbf{R}_n^{-1} \mathbf{R}_p(\tau) \right) &= \sum_{k=0}^{N_T-1} \mathrm{tr}\left(\mathbf{R}_n^{-1} \mathbf{R}_A[k] \right) e^{j2\pi \frac{k}{N_T} \tau} \\ &= \sum_{k=0}^{N_T-1} S[k] \mathrm{tr}\left(\mathbf{R}_n^{-1} \mathbf{D}^k \right) e^{j2\pi \frac{k}{N_T} \tau} \\ \mathbf{R}_A[k] = S[k] \mathbf{D}^k \quad , \quad [\mathbf{D}]_i &= e^{-j2\pi \frac{1}{N_T} i} \\ &= \sum_{k=0}^{N_T-1} S[k] \mathrm{tr}\left(\sigma_n^{-2} \mathbf{D}^k \right) e^{j2\pi \frac{k}{N_T} \tau} \\ &= L \cdot S[0] / \sigma_n^2 \quad (5.26) \\ \mathrm{tr}\left(\mathbf{D}^k \right) &= L \cdot \delta[k] \quad (5.27) \end{aligned}$$

In the case of stationary noise, the term $\mathrm{tr}\left(\mathbf{R}_n^{-1} \mathbf{R}_p(\tau) \right)$ is asymptotically independent of τ as $\mathbf{R}_n^{-1}$ is asymptotically Toeplitz.

CRLB Evaluation

It is more suitable in this case to evaluate the low-SNR CRLB approximation in terms of the second derivatives,

$$\begin{aligned} \mathrm{CRLB}(\tau_{\mathbf{s}}) &\simeq \frac{-1}{E_{\mathbf{x}} \nabla_{\tau_{\mathbf{s}}}^2 \ln p_2(\mathbf{x}|\tau_{\mathbf{s}})} = \frac{-1}{E_{\mathbf{x}} \nabla_{\tau_{\mathbf{s}}}^2 \ln M(\mathbf{x}|\tau_{\mathbf{s}})} \\ &= \frac{-1}{\mathrm{tr}\left(\mathbf{R}_n^{-1} \mathbf{R}_p(\tau_{\mathbf{s}}) \mathbf{R}_n^{-1} \nabla_{\tau_{\mathbf{s}}}^2 \mathbf{R}_p(\tau_{\mathbf{s}}) \right)} \quad (5.28) \end{aligned}$$

Using here the Fourier model of the correlation matrix,

$$\begin{aligned}\mathbf{R}_p(\tau_\mathbf{s}) &= \sum_{k=0}^{N_T-1} \mathbf{R}_A[k] e^{j2\pi \frac{k}{N_T}\tau_\mathbf{s}} \\ \nabla^2_{\tau_\mathbf{s}} \mathbf{R}_p(\tau_\mathbf{s}) &= \sum_k \mathbf{R}_A[k] \left(-4\pi^2 \frac{k^2}{N_T^2}\right) e^{j2\pi \frac{k}{N_T}\tau_\mathbf{s}} \end{aligned} \tag{5.29}$$

as well as the white noise assumption $\mathbf{R}_n = \sigma_n^2 \mathbf{I}$, we obtain exactly the same result for the CRLB as was derived before in the cyclic Gaussian case,

$$\mathrm{CRLB}(\tau_\mathbf{s}) \simeq \frac{1}{4\pi^2 T_o B} \left(\frac{\sigma_n^2}{\sigma_{p,T}}\right)^2 \gamma_p^2$$

Both CRLB's coincide (asymptotically for large L) even if the white noise assumption is not used. This result is expected as the matrix used in the Gaussian metric can be aproximated in the low SNR region as,

$$(\mathbf{R}_n + \mathbf{R}_p)^{-1} \simeq \mathbf{R}_n^{-1} - \mathbf{R}_n^{-1}\mathbf{R}_p\mathbf{R}_n^{-1}$$

In the following, the metric for the non Gaussian case shall be used.

Discrimination of the pulsar from noise

Now we examine the mean and variance of the new metric $Z(\mathbf{x}|\tau) = \mathbf{x}^\mathrm{H}\mathbf{A}(\tau)\mathbf{x}$, with $\mathbf{A} = \mathbf{R}_n^{-1}\mathbf{R}_p(\tau)\mathbf{R}_n^{-1}$. This will help determine the necessary integration time where the pulsar signal starts to be distinguishable from noise. As is also commented later in more detail, the distinguishability threshold approximately determines the operating region where the previously derived CRLB is applicable. Note that for this metric, knowledge of noise and signal power is not necessary but it will be for generating reliability information. For this term, we have $\mathbf{x} = \mathbf{p} + \mathbf{n}$, and,

$$Z(\mathbf{x}|\tau) = \mathbf{x}^\mathrm{H}\mathbf{A}(\tau)\mathbf{x} \tag{5.30}$$

$$= \mathbf{p}^\mathrm{H}\mathbf{A}(\tau)\mathbf{p} + \mathbf{n}^\mathrm{H}\mathbf{A}(\tau)\mathbf{n} + 2\mathrm{Re}\left(\mathbf{p}^\mathrm{H}\mathbf{A}(\tau)\mathbf{n}\right) \tag{5.31}$$

We assume there is some synchronization error, so that the true delay is τ'. Therefore, as the noise and pulsar signal are not correlated, the expectation of $Z(\mathbf{x}|\tau)$ is,

$$\begin{aligned} Z(\tau,\tau') &= E_\mathbf{x} Z(\mathbf{x}|\tau) \\ &= \mathrm{tr}\left(\mathbf{R}_n^{-1}\mathbf{R}_p(\tau)\mathbf{R}_n^{-1}\mathbf{R}_p(\tau')\right) + \mathrm{tr}\left(\mathbf{R}_n^{-1}\mathbf{R}_p(\tau)\right) \qquad (5.32) \\ Z_p(\tau,\tau') &= \mathrm{tr}\left(\mathbf{R}_n^{-1}\mathbf{R}_p(\tau)\mathbf{R}_n^{-1}\mathbf{R}_p(\tau')\right) \qquad (5.33) \end{aligned}$$

As we have shown before, the second term in (5.32) is independent of τ. Hence, only the first term, $Z_p(\tau,\tau')$ can provide timing discrimination. Further, when $|\tau - \tau'| > T_p$, with T_p the duration of the pulse, we have $Z_p(\tau,\tau') \simeq 0$. To evaluate the quality of the metric, this discrimination has to be compared with the level of equivalent metric noise. The equivalent noise covariance is evaluated as,

$$\begin{aligned} R_Z(\tau,\tau') &= E_\mathbf{x}\left|Z(\mathbf{x}|\tau) - Z(\tau,\tau')\right|^2 \\ &= E_\mathbf{x}\left|Z(\mathbf{x}|\tau)\right|^2 - \left|Z(\tau,\tau')\right|^2 \end{aligned} \tag{5.34}$$

where,

$$\begin{aligned} E_\mathbf{x}\left|Z(\mathbf{x}|\tau)\right|^2 &= E_\mathbf{x}\mathrm{tr}^2\left(\mathbf{R}_n^{-1}\mathbf{R}_p(\tau)\mathbf{R}_n^{-1}\mathbf{x}\mathbf{x}^\mathrm{H}\right) \\ &= E_\mathbf{x}\mathrm{tr}\left(\left(\mathbf{R}_n^{-1}\mathbf{R}_p(\tau)\mathbf{R}_n^{-1}\mathbf{x}\mathbf{x}^\mathrm{H}\right) \otimes \left(\mathbf{R}_n^{-1}\mathbf{R}_p(\tau)\mathbf{R}_n^{-1}\mathbf{x}\mathbf{x}^\mathrm{H}\right)\right) \\ &= \mathrm{tr}\left(\left(\mathbf{R}_n^{-1}\mathbf{R}_p(\tau)\mathbf{R}_n^{-1} \otimes \mathbf{R}_n^{-1}\mathbf{R}_p(\tau)\mathbf{R}_n^{-1}\right) E_\mathbf{x}\left(\mathbf{x}\mathbf{x}^\mathrm{H} \otimes \mathbf{x}\mathbf{x}^\mathrm{H}\right)\right) \\ &= \mathrm{tr}\left(\left(\mathbf{R}_n^{-1}\mathbf{R}_p(\tau)\mathbf{R}_n^{-1} \otimes \mathbf{R}_n^{-1}\mathbf{R}_p(\tau)\mathbf{R}_n^{-1}\right)\mathbf{R}_{4,p}(\tau')\right) \end{aligned} \tag{5.35}$$

with $\mathbf{R}_{4,p}$ containing all fourth-order moments of the pulsar signal and $\otimes$ denoting the Kronecker product. As this expression is rather awkward, we have assumed Gaussian statistics for the pulsar signal to arrive

at a more informative expression. To evaluate $E_{\mathbf{x}}\left|Z(\mathbf{x}|\tau)\right|^2 = E_{\mathbf{x}}\left|\mathbf{x}^{\mathrm{H}}\mathbf{A}(\tau)\mathbf{x}\right|^2$, we shall use the following property: for a normally distributed random variable $\mathbf{v}$ and a positive definite matrix $\mathbf{\Omega}$, the following equation is true,

$$E(\mathbf{v}^{\mathrm{H}}\mathbf{\Omega}\mathbf{v})^2 = \mathrm{tr}^2\mathbf{\Omega} + (K-1)\mathrm{tr}\mathbf{\Omega}^2$$

where $K = 2, 3$ for complex or real data, respectively. Hence, setting $\mathbf{x} = \mathbf{R}_x^{\frac{1}{2}}(\tau')\mathbf{v}$, we obtain,

$$E_{\mathbf{x}}\left|Z(\mathbf{x}|\tau)\right|^2 = \mathrm{tr}^2\left(\mathbf{A}(\tau)\mathbf{R}_x(\tau')\right) + (K-1)\mathrm{tr}\left(\left(\mathbf{A}(\tau)\mathbf{R}_x(\tau')\right)^2\right)$$

and,

$$R_Z(\tau,\tau') = \frac{1}{K-1}\cdot\frac{\mathrm{tr}^2\left(\mathbf{A}(\tau)\mathbf{R}_p(\tau')\right)}{\mathrm{tr}\left(\left(\mathbf{A}(\tau)\mathbf{R}_x(\tau')\right)^2\right)}$$

which, expressing the traces in terms of the eigenvalues, it is easy to see that this ratio goes to infinity for large L. The asymptotic trend is examined by way of an example.

Example: we consider the white noise case, $\mathbf{R}_n = \sigma_n^2\mathbf{I}$, a diagonal $\mathbf{R}_p$ and low SNR. We consider that $\tau = \tau'$ to evaluate the quality of the discrimination at the optimum time and therefore we drop the dependence of matrices on time variables. Then,

$$\begin{aligned}
\mathrm{tr}\left(\left(\mathbf{A}\mathbf{R}_x\right)^2\right) &\simeq \mathrm{tr}\left(\left(\mathbf{A}\mathbf{R}_n\right)^2\right) = \mathrm{tr}\left(\left(\mathbf{R}_n^{-1}\mathbf{R}_p\right)^2\right) \\
\mathrm{tr}^2\left(\mathbf{A}\mathbf{R}_p\right) &= \mathrm{tr}^2\left(\left(\mathbf{R}_n^{-1}\mathbf{R}_p\right)^2\right) \\
R_Z(\tau,\tau) &= \frac{1}{K-1}\mathrm{tr}\left(\left(\mathbf{R}_n^{-1}\mathbf{R}_p\right)^2\right)
\end{aligned} \tag{5.36}$$

Therefore, for the white noise case and making explicit the dependence on the integration length L, we get,

$$\begin{aligned}
\Gamma_L &= R_Z(\tau,\tau) \\
&= \frac{1}{(K-1)\sigma_n^4}\mathrm{tr}\mathbf{R}_p^2 \\
&= \frac{1}{(K-1)\sigma_n^4}N_I\sum_{k=0}^{N_T-1}\sigma_p^4[k]
\end{aligned} \tag{5.37}$$

with $N_I = T_o/T$ the number of pulsar integration periods, T_o the observation time and T the pulsar period. The number of samples per period, N_T, fulfils $N_T = T/T_s = TB$, with T_s the sampling period and B the corresponding bandwidth. The number of samples is $L = N_I N_T = T_o B$. Hence,

$$\begin{aligned}
\Gamma_L &= \frac{1}{(K-1)\sigma_n^2}N_I N_T\frac{1}{N_T}\sum_{k=0}^{N_T-1}\sigma_p^4[k] \\
&= \frac{1}{(K-1)}L\left(\frac{\sigma_{p,T}^2}{\sigma_n^2}\right)^2\frac{1}{N_T}\sum_{k=0}^{N_T-1}\frac{\sigma_p^4[k]}{\sigma_{p,T}^4}
\end{aligned} \tag{5.38}$$

Hence, the pulsar will be distinguishable when Γ_L exceeds a given threshold, Γ_{th} (Other type of criteria may be established in terms of hypotheses testing theory). Then, the final equation is expressed in terms of the number of integration samples and the average SNR as,

$$\begin{aligned}
L\cdot\left(\frac{\sigma_{p,T}^2}{\sigma_n^2}\right)^2 &\geq (K-1)\Gamma_{\mathrm{th}}\xi_p \\
\xi_p &= \frac{\sigma_{p,T}^4}{\frac{1}{N_T}\sum_{k=0}^{N_T-1}\sigma_p^4[k]}
\end{aligned} \tag{5.39}$$

and ξ_p a factor depending on the pulse shape. A more detailed analysis shows that this factor is proportional to the duty cycle of the pulsar.

5.1.5 Performance Evaluation: Regions of Operation

We consider the timing error behaviour of the ML algorithm with respect to the predicted CRLB. Several regions can be distinguished in the corresponding timing error plots (see figures (5.2) and (5.3)):

- saturation region: the probability density function of the timing error is practically uniform over the pulsar period and equal to its apriori value $\sigma_\tau = \frac{1}{\sqrt{12}}T$.
- sub-threshold region: the variance estimation error departs substantially from the CRLB at SNR below the threshold. The threshold decreases with longer integration times.
- CRLB region: the CRLB is a tight lower bound to the performance of the ML estimator, improving at larger SNR's. Within this region we can distinguish two sub-regions:
  1. the low-SNR region where the previously derived CRLB applies.
  2. the high-SNR region where the signal of interest is more powerful than noise. Here a lower saturation is observed due to pulsar self-noise (random individual pulses). The timing error in this region decreases for longer integration times.

The CRLB and the Threshold Effect

The CRLB is a valid, and tight, lower bound to the performance of the ML algorithm in the small error region. When the ML function is maximized, equating its derivative to zero, it is assumed that noise is located in the vicinity of the zero-crossing, where the derivative is approximately linear (small error assumption). When noise is sufficiently high, or integration time is too low, noise causes the data to enter the non-linear region of the ML derivative. Hence, we provide here an estimate of the threshold of operation of the CRLB based on this assumption. It will be shown that the criterion is sensitive to the pulse shape. In this context, we will use the S-curve defined as the derivative of the expected metric with respect to the timing parameter τ. For a metric of the type $Z(\mathbf{x}|\tau) = \mathbf{x}^{\mathrm{H}}\mathbf{A}(\tau)\mathbf{x}$ we get,

$$\begin{aligned} S(\tau) &= E_{\mathbf{x}}\nabla_\tau Z(\mathbf{x}|\tau) \\ &= \mathrm{tr}(\mathbf{R}_n^{-1}\mathbf{R}_p(\tau')\mathbf{R}_n^{-1}\nabla_\tau \mathbf{R}_p(\tau')) \end{aligned} \tag{5.40}$$

Now, to evaluate the above expression at the zero crossing, we assume $\tau' = 0$, without loss of generality. Hence, its Taylor expansion yields,

$$S(\tau) = S_0^{(1)}\tau + \frac{1}{3!}S_0^{(3)}\tau^3 + o(\tau^5)$$

we assume as value for the threshold, τ_{th}, that point where the cubic term exceeds a given percentage of the linear term. A more fundamental justification of this procedure is interpreting the threshold as that point where the estimation error is no longer Gaussian, as the Gaussianity of the estimation error is a fundamental property in the region of operation of the CRLB for a given integration time and SNR. In comparing the variance of the estimation error with the S-curve, it seems reasonable to set as threshold that point where the CRLB reaches a given value (which will depend on the S-curve and hence on the pulse shape). This point may be calibrated for each pulse shape. Then, to determine the threshold of the operation of the ML algorithm, we set $\tau_{\mathrm{th}}^2 = \mathrm{CRLB}(\tau)$. As an approximation, we establish an ad-hoc percentage η such that,

$$\begin{aligned} S_0^{(1)}\tau_{\mathrm{th}} + \frac{1}{3!}S_0^{(3)}\tau_{\mathrm{th}}^3 &= S_0^{(1)}(1-\eta)\tau_{\mathrm{th}} \\ \tau_{\mathrm{th}}^2 &= -6\eta\frac{S_0^{(1)}}{S_0^{(3)}} \end{aligned} \tag{5.41}$$

Both derivatives may be calculated as,

$$\begin{aligned} S_0^{(1)} &= \mathrm{tr}(\mathbf{R}_n^{-1}\mathbf{R}_p(\tau')\mathbf{R}_n^{-1}\nabla_\tau^2\mathbf{R}_p(\tau')) \\ S_0^{(3)} &= \mathrm{tr}(\mathbf{R}_n^{-1}\mathbf{R}_p(\tau')\mathbf{R}_n^{-1}\nabla_\tau^4\mathbf{R}_p(\tau')) \end{aligned} \tag{5.42}$$

In terms of the previously defined spectral coefficients $S[k]$, we establish for the white noise case,

$$\begin{aligned} S_0^{(1)} &= \frac{L}{\sigma_n^2}\frac{4\pi^2}{N_T^2}\sum_k |S[k]|^2 k^2 \\ S_0^{(3)} &= \frac{L}{\sigma_n^2}\frac{16\pi^4}{N_T^4}\sum_k |S[k]|^2 k^4 \end{aligned} \tag{5.43}$$

where in these derivatives, time units have now been expressed in samples: τ_s. Hence, the threshold time in samples, $\tau_{s,\mathrm{th}}$ is expressed as,

$$\tau_{s,\mathrm{th}}^2 = \frac{6\eta}{4\pi^2}\frac{\frac{1}{N_T^2}\sum_k |S[k]|^2 k^2}{\frac{1}{N_T^4}\sum_k |S[k]|^2 k^4} \tag{5.44}$$

Setting this value equal to the CRLB: $\tau_{s,\mathrm{th}}^2 = \mathrm{CRLB}(\tau_s)$ yields the threshold condition for the integration time and SNR,

$$\mathrm{CRLB}(\tau_s) = \frac{1}{4\pi^2 L}\left(\frac{\sigma_n^2}{\sigma_{p,T}^2}\right)^2 \frac{1}{\sum_k \left|\frac{S[k]}{S[0]}\right|^2 \frac{k^2}{N_T^2}} \tag{5.45}$$

and,

$$L\cdot\left(\frac{\sigma_n^2}{\sigma_{p,T}^2}\right)^2 \geq \phi_p = \frac{1}{6\eta}\frac{\sum_k \left|\frac{S[k]}{S[0]}\right|^2 \frac{k^4}{N_T^4}}{\left(\sum_k \left|\frac{S[k]}{S[0]}\right|^2 \frac{k^2}{N_T^2}\right)^2} \tag{5.46}$$

which is a similar threshold as that derived for pulsar distinguishability from noise.

Comments: One consideration is important here. The above derivation has assumed derivability of the S-curve, with continuity beyond the third derivative. The corresponding value for the threshold is reasonable if higher order derivatives are not abnormally high. The double triangular profile used in the derivation of the Quality factor does not fulfil this condition. Hence, in deriving an estimate of the threshold, without resorting to calibration, we can either apply a smoothing function to the double triangular pulse, preserving a similar shape as much as possible, or use the alternative equation based on the minimum discrimination of the pulsar from noise, or the most conservative of both predictions. In either case, both methods are ad-hoc. Nevertheless the threshold constant ϕ_p may be calibrated for any pulse using a numerical simulation, and extrapolating the result to other values of L and SNR. Although an approximated profile has been used in deriving results, the CRLB and its threshold are sensitive to the true pulse shape and a more detailed analysis should use the true digitized pulsar profiles.

Gaussian Pulse: Evaluation of the timing error covariance is highly dependent on the pulsar profile. For the sake of comparison with results obtained with the double triangular pulse, the CRLB and threshold condition have also been evaluated for a Gaussian profile using the 50 % intensity duration T_{50} in the pulsar tables. The CRLB is provided by the approximate expression,

$$\mathrm{CRLB}(\tau) \simeq \frac{1}{T_o B}\left(\frac{\sigma_n^2}{\sigma_{p,T}^2}\right)^2 \frac{2\sqrt{\pi}}{(2\ln 2)^{3/2}}\frac{T_{50}}{T}T_{50}^2$$

and the threshold condition has been calibrated to,

$$\mathrm{CRLB}(\tau) \leq \frac{0.23^2}{2\ln 2}T_{50}^2$$

which establishes the necessary lower bound on $L\cdot \mathrm{SNR}^2$.

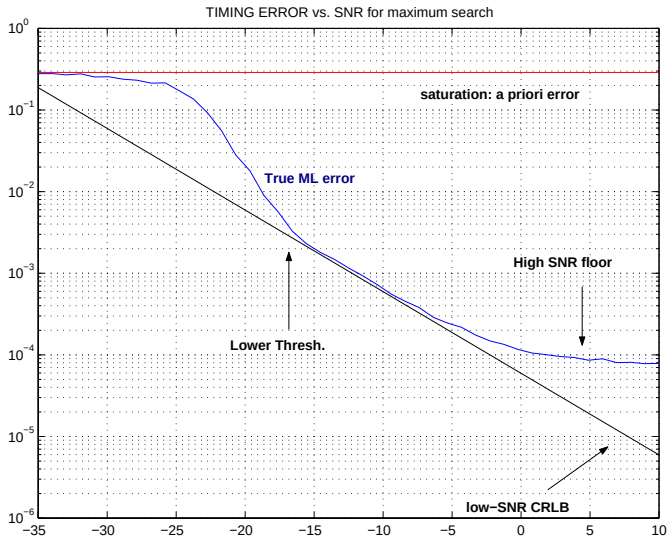

Figure 5.2: Depiction of the low-SNR CRLB (low-SNR approximation used in this study to the true CRLB) versus the true performance of the ML algorithm for timing estimation, obtained for a rectangular pulse profile at 25% duty cycle. The units of root mean square timing error correspond to the normalization with respect to the pulsar period T, plotted versus the average pulsar SNR in dB. The saturation region to the a priori error at $1/\sqrt{12}$ and the high SNR floor determine the operating range of the ML algorithm. At the lower threshold, the true performance departs from the low-SNR CRLB, and rises to the saturation. In the sub-threshold region, timing error is no longer Gaussian and unbiased. The operating region of the low-SNR CRLB is valid above the threshold and before the floor effect starts to be important at high SNR. Taking into account the SNR's listed in the database for the effective antenna area $A_e = 10$ square m., timing estimation algorithms will never operate in the floor (high SNR) region.

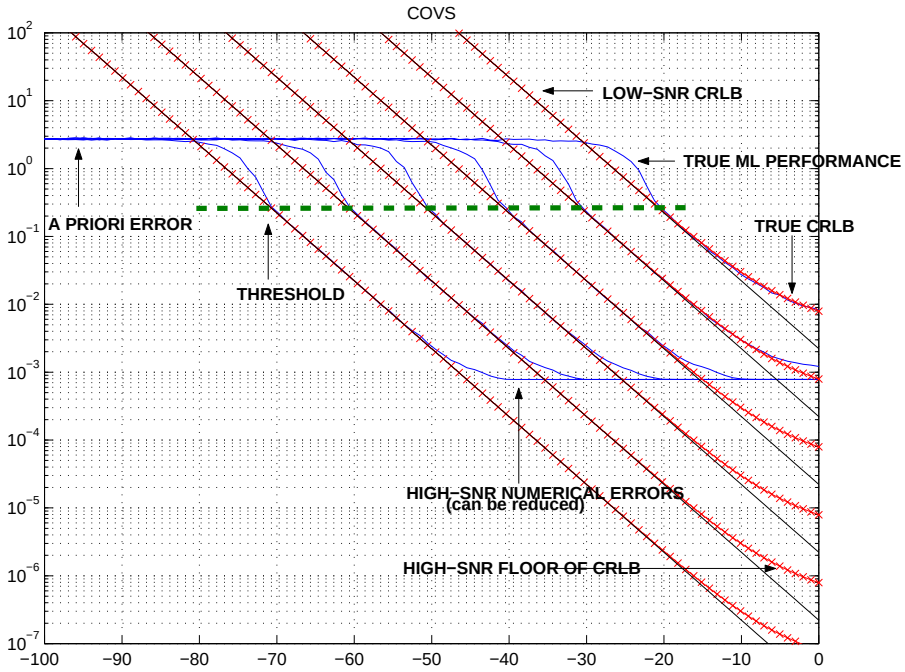

Figure 5.3: Depiction of timing error performance of the ML algorithm for a Gaussian power profile and several integration lengths (different in factors of 100). The standard deviation of the timing error normalized to the standard deviation of the Gaussian pulse is depicted versus the average SNR (dB) of the pulsar signal. The signal statistics has been considered Gaussian. Several effects can be observed: (**a**) the threshold occurs at the same timing error variance in all cases, which constitues an experimental verification of the theoretical threshold equations. It can be observed how the timing error rises steeply below the threshold SNR ; (**b**) above the threshold, the true CRLB coincides with the performance of the ML timing estimation algorithm (for a low integration length); (**c**) the true CRLB reaches a floor at high SNR for a finite integration length due to the intrinsic stochastic nature of the signal; (**d**) only a finite grid of timing hypotheses is searched, so that a numerical floor occurs for all sufficiently high integration lengths (this can be reduced or eliminated by refining the search algorithm using gradient methods), where the numerical error is larger than the final noise-induced timing error; (**e**) the operation region of the derived equations is contained between the high-SNR floor and the low-SNR threshold; (**f**) at very low SNR, the timing error variance saturates to its a priori value. (**g**) note the influence of the 100 factors between different integration lengths (number of processed samples): each time the integration length is increased by a factor of 100, the corresponding timing error standard deviation decreases by a factor of 10.

5.1.6 Square Timing Recovery

It has been shown previously that pulsar phase estimation can be carried out from maximization of metrics of the type $Z(\mathbf{x}|\tau_\mathbf{s}) = \mathbf{x}^\mathrm{H}\mathbf{A}(\tau_\mathbf{s})\mathbf{x}$ in the time domain, where the correlation matrix $\mathbf{A}(\tau_\mathbf{s})$ incorporates knowledge on the pulsar and noise signals, and $0 \leq \tau_\mathbf{s} < N_T$ models an appropriate pulsar timing offset in samples. Here, pulsar phase estimation $\tau_\mathbf{s}/N_T$ will be considered in the frequency domain to obtain sub-sample resolution for the timing offset estimate. This will be precise if the pulsar profile is band-limited, i.e. can be interpolated by a finite number of complex exponentials. If the pulsar pulse duration is small w.r.t. T and the noise spectral density variations are not too large in the band under analysis, matrix $\mathbf{A}(\tau_\mathbf{s})$ is reasonably approximated to a block-diagonal matrix of $N_T \times N_T$ blocks $\mathbf{A}_n(\tau_\mathbf{s})$, with the discrete time n evaluated at multiples of the pulsar period: $n = n_1 N_T$. So that, in terms of the corresponding subvectors $\mathbf{x}_n$ of $\mathbf{x}$, each containing a single pulsar period out of N_I periods, we have,

$$Z(\mathbf{x}|\tau_\mathbf{s}) = \mathbf{x}^\mathrm{H}\mathbf{A}(\tau_\mathbf{s})\mathbf{x} = \sum_{n_1=0}^{N_I-1} \mathbf{x}^\mathrm{H}_{n_1\cdot N_T}\mathbf{A}_{n_1\cdot N_T}(\tau_\mathbf{s})\mathbf{x}_{n_1\cdot N_T}$$

Now, matrix $\mathbf{A}_{n_1\cdot N_T}(\tau_\mathbf{s})$ admits a Fourier expansion as it stems from the correlation matrix of a cyclo-stationary process,

$$\begin{aligned}\mathbf{A}_{n_1\cdot N_T}(\tau_\mathbf{s}) &= \sum_{k=0}^{N_T-1} \mathbf{R}_A[k] e^{j2\pi\frac{k}{N_T}(n_1\cdot N_T - \tau_\mathbf{s})} \\ &= \sum_{k=0}^{N_T-1} \mathbf{R}_A[k] e^{-j2\pi\frac{k}{N_T}\tau_\mathbf{s}} \end{aligned} \tag{5.47}$$

Therefore, substitution into the metric equation yields,

$$\begin{aligned} Z(\mathbf{x}|\tau_\mathbf{s}) &= \sum_{n_1=0}^{N_I-1} \mathbf{x}^\mathrm{H}_{n_1\cdot N_T} \left(\sum_{k=0}^{N_T-1} \mathbf{R}_A[k] e^{-j2\pi\frac{k}{N_T}\tau_\mathbf{s}} \right) \mathbf{x}_{n_1\cdot N_T} \\ &= \sum_{k=0}^{N_T-1} e^{-j2\pi\frac{k}{N_T}\tau_\mathbf{s}} \sum_{n_1=0}^{N_I-1} \mathbf{x}^\mathrm{H}_{n_1\cdot N_T} \mathbf{R}_A[k] \mathbf{x}_{n_1\cdot N_T} \\ &= \sum_{k=0}^{N_T-1} y_k \cdot e^{-j2\pi\frac{k}{N_T}\tau_\mathbf{s}} \end{aligned} \tag{5.48}$$

$$y_k = \sum_{n_1=0}^{N_I-1} \mathbf{x}^\mathrm{H}_{n_1\cdot N_T} \mathbf{R}_A[k] \mathbf{x}_{n_1\cdot N_T} \tag{5.49}$$

with $y_k, 0 \leq k \leq N_T - 1$ a compressed data sequence of N_T samples from the original $L = N_T N_I$ samples, which can be used in the previous equation to maximize $Z(\mathbf{x}|\tau_\mathbf{s})$ in terms of $\tau_\mathbf{s}$. In the white noise case, $\mathbf{R}_A[k]$ is found to be a diagonal matrix expressed as,

$$\begin{aligned}\mathbf{R}_A[k] &= S[k] \cdot \mathbf{D}^k \\ [\mathbf{D}]_i &= e^{-j2\pi\frac{1}{N_T}i} \end{aligned} \tag{5.50}$$

So that the operation $\mathbf{x}^\mathrm{H}_{n_1\cdot N_T}\mathbf{R}_A[k]\mathbf{x}_{n_1\cdot N_T}$ is in fact the $S[k]$-weighted DFT at the discrete normalized frequency k/N_T of the modulus squared components of each subvector $\mathbf{x}_{n_1\cdot N_T}$, and,

$$\begin{aligned}\mathbf{x}^\mathrm{H}_{n_1\cdot N_T}\mathbf{R}_A[k]\mathbf{x}_{n_1\cdot N_T} &= S[k] \sum_{i=0}^{N_T-1} |x(n_1 N_T - i)|^2 e^{-j2\pi\frac{k}{N_T}i} \\ y_k &= S[k] \sum_{i=0}^{N_T-1} \left(\sum_{n_1=0}^{N_I-1} |x(n_1 N_T - i)|^2 \right) e^{-j2\pi\frac{k}{N_T}i} \end{aligned} \tag{5.51}$$

As an example, let matrix $\mathbf{A}(\tau_\mathbf{s})$ be defined as $\mathbf{A}(\tau_\mathbf{s}) = \mathbf{R}_n^{-1}\mathbf{R}_p(\tau_\mathbf{s})\mathbf{R}_n^{-1}$, and let the true correlation of the pulsar signal be $\mathbf{R}_p(\tau'_\mathrm{s})$, where we want to estimate τ'_s by varying $\tau_\mathbf{s}$ in the correlation model.

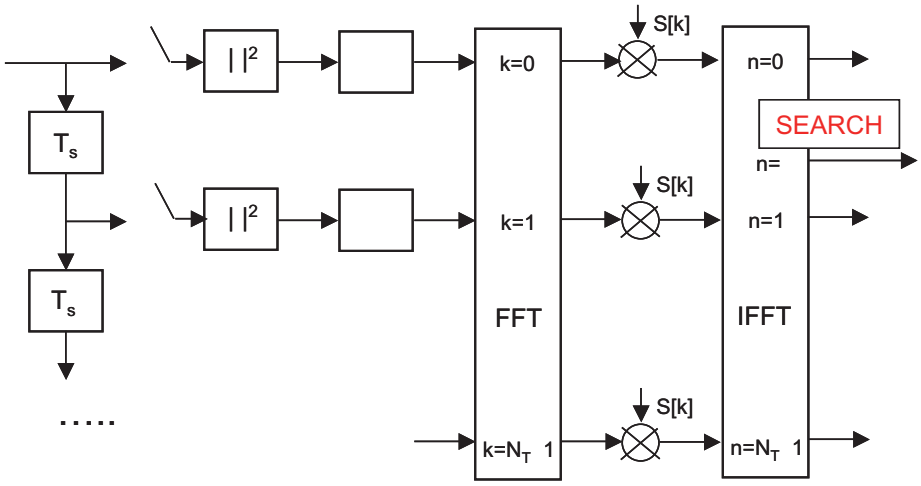

Figure 5.4: Phase estimation based on square timing recovery. The scheme generates an average profile before performing a single correlation with the pulsar profile template. Correlation has been performed in the frequency domain for sub-sample resolution, although other correlation-interpolation approaches may be formulated in the time domain.

Expectation of the metric

We will analyze an estimator $\hat{\tau}'_{\mathrm{s}}$ from the expression of $Z(\mathbf{x}|\tau_{\mathbf{s}})$. We first evaluate the expectation, so that,

$$\begin{aligned} E_{\mathbf{x}} Z(\mathbf{x}|\tau_{\mathbf{s}}) &= \sum_{k=1}^{N_T-1} (E_{\mathbf{x}} y_k) e^{-j2\pi \frac{k}{N_T}\tau_{\mathbf{s}}} \\ E_{\mathbf{x}} y_k &= \mathrm{tr}(\mathbf{R}_A[k](\mathbf{R}_p(\tau'_{\mathrm{s}}) + \mathbf{R}_n)) \end{aligned} \tag{5.52}$$

But we note that for the white noise case where $\mathbf{R}_n = \sigma_n^2 \mathbf{I}$, we have that $\mathrm{tr}(\mathbf{R}_A[k]\mathbf{R}_n) = S[k]\sigma_n^2 \mathrm{tr}(\mathbf{D}^k) = 0$. Hence, for $k \neq 0$,

$$\begin{aligned} E_{\mathbf{x}} y_k &= S[k] \mathrm{tr}\left(\mathbf{D}^k \mathbf{R}_p(\tau'_{\mathrm{s}})\right) \\ &= S[k] \sum_{k'=0}^{N_T-1} \mathrm{tr}\left(\mathbf{D}^k \mathbf{R}_A[k']\right) e^{-j2\pi \frac{k'}{N_T}\tau'_{\mathrm{s}}} \\ &= S[k] \sum_{k'=0}^{N_T-1} \mathrm{tr}\left(\mathbf{D}^k \mathbf{R}_A[k']\right) e^{-j2\pi \frac{k'}{N_T}\tau'_{\mathrm{s}}} \\ &= S[k] \sum_{k'=0}^{N_T-1} \mathrm{tr}\left(\mathbf{D}^k S[k'] \mathbf{D}^{k'}\right) e^{-j2\pi \frac{k'}{N_T}\tau'_{\mathrm{s}}} \\ &= S[k] \sum_{k'=0}^{N_T-1} (S[k']\delta[k+k']) e^{-j2\pi \frac{k'}{N_T}\tau'_{\mathrm{s}}} \\ &= S[k]S[-k] e^{-j2\pi \frac{k}{N_T}\tau'_{\mathrm{s}}} \\ &= |S[k]|^2 e^{-j2\pi \frac{k}{N_T}\tau'_{\mathrm{s}}} \end{aligned} \tag{5.53}$$

Clearly, Z is maximized for $\tau_{\mathbf{s}} = -\tau'_{\mathrm{s}}$, which corresponds to maximal ratio combining of the components at multiples of the cycle frequency.

5.1.7 Multi-band Analysis and Interstellar Dispersion

In the previous sections, general equations have been derived assuming knowledge of the pulsar correlation matrix $\mathbf{R}_p(\tau)$. In some cases, particular expressions as CRLB's are obtained assuming a diagonal structure

for $\mathbf{R}_p(\tau)$. This is only valid when the reception bandwidth is sufficiently small. For larger bandwidths, non-negligible components appear in the sub-diagonals of $\mathbf{R}_p(\tau)$. Unfortunately, it has been shown that experimental data does not provide sufficient information to derive the detailed structure of $\mathbf{R}_p(\tau)$. As larger B's are considered, the dispersion of the interstellar medium starts to appear, spreading the duration of the pulsar pulse (up to a limit, as the delay in inversely proportional to $1/f^2$). This would be irrelevant for processing if $\mathbf{R}_p(\tau)$ were known, as the shape of the broadened profile would be available. Nevertheless, experimental data is limited to small B.

An alternative to use the derived framework is to consider that the data vector $\mathbf{x}$ contains data sub-vectors corresponding to different narrow bands of the large band B, but sufficiently large to preserve the pulse shape. Then, processing combines several bands, where for each i-th band, the sub-correlation matrix $\mathbf{R}_p^{(i)}(\tau)$ is known. The difference between consecutive $\mathbf{R}_p^{(i)}(\tau)$'s can be inferred from the dispersion model of the interstellar medium and amounts to a frequency-dependent time delay and a scaling factor. This time-delay is known from the dispersion coefficient of each pulsar and can be compensated over all sub-bands (in fact, the dispersion measure is varying slowly and should be tracked). Nevertheless, it should be taken into account that signals extracted from contiguous bands are correlated due to cyclo-stationarity. The value of the cross-correlation of signals from differents sub-bands is not known. At least it is reasonable to assume that for N_s sub-bands of bandwidth $B_s = B/N_s$ each, frequency components more than $2B_s$ apart can be already considered uncorrelated.

Assuming uncorrelated sub-bands, the global correlation matrix is block-diagonal with block-elements corresponding to the (diagonal) correlation matrix over each sub-band. Then, an estimate of the timing error, $\hat{\sigma}_\tau^2$, can be obtained, which will not differ substantially from the true timing error in presence of the sub-band cross-correlation induced by cyclo-stationarity (it is limited to basically the first sub-diagonal). This small difference can be incorporated to a safety margin to guarantee fulfilment of specifications. We have then that,

$$\hat{\sigma}_\tau^2 = \frac{\gamma_p^2}{4\pi^2 T_o B_s}\left(\sum_{i=0}^{N_s-1}\frac{N_p^2(i)}{N_0^2(i)}\right)^{-1} = \frac{\gamma_p^2}{4\pi^2 T_o B}\left(\frac{1}{N_s}\sum_{i=0}^{N_s-1}\frac{N_p^2(i)}{N_0^2(i)}\right)^{-1} \tag{5.54}$$

in terms of the pulsar and noise spectral power density ratios N_p and N_0 at each sub-channel, which is basically the same single-channel equation where the square SNR average over all sub-bands is used. The shape factor γ_p^2 of the pulsar pulse is considered uniform over the sub-bands (no shape distortion). In the numerical evaluation of the position error we will simply take the SNR at 1 GHz as this average value, assuming suitable lower and upper limits of the band B.

5.2 PATD Estimation

Spacecraft speed introduces a Doppler effect which changes the observed PRP. Period to period integration will thus be affected by pulse arrival time drift (PATD) when the averaging period does not coincide with the true period, and degradation will occur. Therefore, the pulsar PRP should be known to a high degree of accuracy and PATD estimation should also be considered. By way of an example, let us consider that the spacecraft is travelling at speed v, and let us compute the drift-time, normalized to the pulsar duration at 10% peak intensity T_{10}, during an observation time T_o,

$$\frac{\Delta t}{T_{10}} = \frac{v}{c}\frac{1}{T}\frac{T_o}{T_{10}} \tag{5.55}$$

For the millisecond pulsar B1937+21, a speed of 50000 kmph. in the pulsar direction and one minute of observation, we have a value of 13.95 T_{10} time-units.

We formulate the ML algorithm by making the pulsar correlation model dependent on the PATD so

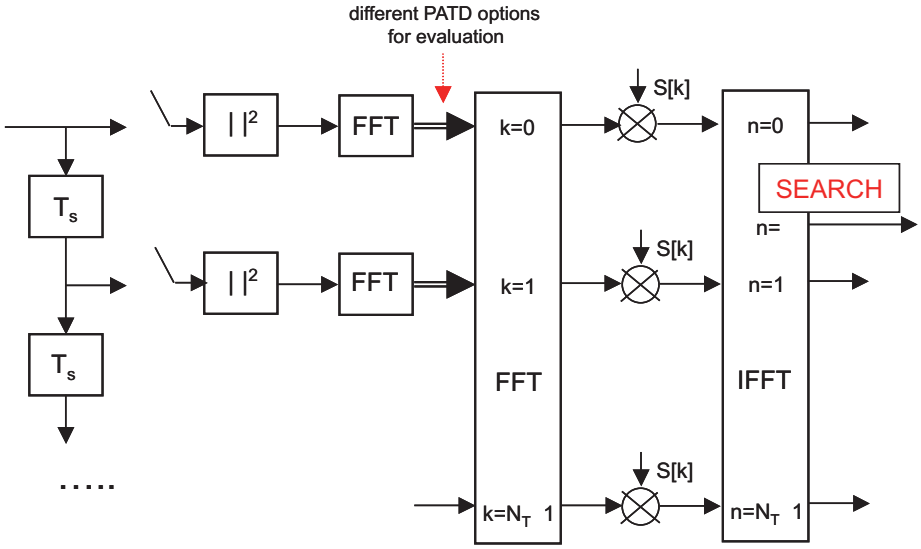

Figure 5.5: Joint phase and PATD estimation based on square timing recovery. The FFT blocks in the polyphase branches are not full, only the lower bins of the FFT are checked within the PATD range.

that $\mathbf{R}_p(\tau', \delta\tau')$ is included in the metric. The model for $\mathbf{A}$ is expressed as,

$$\begin{aligned}\mathbf{A}_{n_1 \cdot N_T - n_1 \delta_T}(\tau_\mathbf{s}) &= \sum_{k=0}^{N_T-1} \mathbf{R}_A[k] e^{j2\pi \frac{k}{N_T}(n_1 \cdot N_T - n_1 \delta_T - \tau_\mathbf{s})} \\ &= \sum_{k=0}^{N_T-1} \mathbf{R}_A[k] e^{-j2\pi \frac{k}{N_T/\delta_T} n_1} e^{-j2\pi \frac{k}{N_T}\tau_\mathbf{s}} \end{aligned} \tag{5.56}$$

with δ_T a small value to account for the PATD. Then, substitution into the metric equation yields,

$$\begin{aligned} Z(\mathbf{x}|\tau_\mathbf{s}, \delta_T) &= \sum_{n_1=0}^{N_I-1} \mathbf{x}^{\mathrm{H}}_{n_1 \cdot N_T} \left(\sum_{k=0}^{N_T-1} \mathbf{R}_A[k] e^{-j2\pi \frac{k}{N_T/\delta_T} n_1} e^{-j2\pi \frac{k}{N_T}\tau_\mathbf{s}} \right) \mathbf{x}_{n_1 \cdot N_T} \\ &= \sum_{k=0}^{N_T-1} e^{-j2\pi \frac{k}{N_T}\tau_\mathbf{s}} \sum_{n_1=0}^{N_I-1} \mathbf{x}^{\mathrm{H}}_{n_1 \cdot N_T} \mathbf{R}_A[k] \mathbf{x}_{n_1 \cdot N_T} \cdot e^{-j2\pi \frac{k}{N_T/\delta_T} n_1} \\ &= \sum_{k=0}^{N_T-1} y_k(\delta_T) \cdot e^{-j2\pi \frac{k}{N_T}\tau_\mathbf{s}} \end{aligned} \tag{5.57}$$

$$y_k(\delta_T) = \sum_{n_1=0}^{N_I-1} \left(\mathbf{x}^{\mathrm{H}}_{n_1 \cdot N_T} \mathbf{R}_A[k] \mathbf{x}_{n_1 \cdot N_T} \right) \cdot e^{-j2\pi \frac{k}{N_T/\delta_T} n_1} \tag{5.58}$$

Then, several hypotheses of δ_T need to be tracked: a two-dimensional search over $(\tau_\mathbf{s}, \delta_T)$ has to be performed. In the white noise case, the expression for $y_k(\delta_T)$ becomes,

$$\begin{aligned} \mathbf{x}^{\mathrm{H}}_{n_1 \cdot N_T} \mathbf{R}_A[k] \mathbf{x}_{n_1 \cdot N_T} &= S[k] \sum_{i=0}^{N_T-1} |x(n_1 N_T - i)|^2 e^{-j2\pi \frac{k}{N_T} i} \\ y_k(\delta_T) &= S[k] \sum_{i=0}^{N_T-1} \left(\sum_{n_1=0}^{N_I-1} |x(n_1 N_T - i)|^2 e^{-j2\pi \frac{k}{N_T/\delta_T} n_1} \right) e^{-j2\pi \frac{k}{N_T} i} \end{aligned} \tag{5.59}$$

5.2.1 Joint pulsar phase and PATD bounds

We show that in the presence of PATD, the presented scheme generates a pulsar phase estimate uncorrelated with the PATD estimate. The phase estimate corresponds to the pulsar phase in the mid-point of the observation window.

The components of the Fisher Information matrix and the corresponding joint CRLB for this problem are given by,

$$[\mathbf{J}_{\tau_\mathbf{s},\delta_T}]_{1,1} = -\mathrm{tr}\left(\mathbf{R}_n^{-1}\mathbf{R}_p(\tau_\mathbf{s},\delta_T)\mathbf{R}_n^{-1}\nabla^2_{\tau_s}\mathbf{R}_p(\tau_\mathbf{s},\delta_T)\right) \tag{5.60}$$

$$[\mathbf{J}_{\tau_\mathbf{s},\delta_T}]_{1,2} = [\mathbf{J}_{\tau_\mathbf{s},\delta_T}]_{2,1} = -\mathrm{tr}\left(\mathbf{R}_n^{-1}\mathbf{R}_p(\tau_\mathbf{s},\delta_T)\mathbf{R}_n^{-1}\nabla_{\delta_T}\nabla_{\tau_\mathbf{s}}\mathbf{R}_p(\tau_\mathbf{s},\delta_T)\right) = 0 \tag{5.61}$$

$$[\mathbf{J}_{\tau_\mathbf{s},\delta_T}]_{2,2} = -\mathrm{tr}\left(\mathbf{R}_n^{-1}\mathbf{R}_p(\tau_\mathbf{s},\delta_T)\mathbf{R}_n^{-1}\nabla^2_{\delta_T}\mathbf{R}_p(\tau_\mathbf{s},\delta_T)\right) \tag{5.62}$$

and the corresponding CRLB is expressed as the inverse of the Fisher information matrix,

$$\mathrm{CRLB}(\tau_\mathbf{s},\delta_T) = \mathbf{J}^{-1}_{\tau_\mathbf{s},\delta_T} \tag{5.63}$$

where due to the diagonality of $\mathbf{J}_{\tau_\mathbf{s},\delta_T}$, the phase and PATD estimates are not correlated, and asymptotically Gaussian.

References

Steven M. Kay, "Fundamentals of Statistical Signal Processing - Estimation Theory", Prentice-Hall 1993, ISBN 0-13-345711-7.

Chapter 6

Timing Estimation for X-Ray Pulsars

6.1 Timing Estimation for X-Ray Pulsars

This section analyzes synchronization algorithms and associated performance bounds for time-of-arrival (TOA) estimation in the case of X-ray pulsars.

6.1.1 Signal Model

As introduced in Sec. 4.5, the X-ray pulsar density of arrival is *cyclic* in time and will be denoted hereafter as

$$\lambda(t) = \lambda_p(t) + \lambda_n = \lambda(t+T) \tag{6.1}$$

where T is the pulsar PRP, $\lambda_p(t)$ its characteristic periodic signature in counts per second and λ_n the density of arrival for the stationary background noise. The bandwidth of $\lambda_p(t)$ is limited to $1/2T_b$ with T_b the detector temporal resolution ($T_b = 100\mu s$ for the ROSAT detector). Hereafter $\lambda_p(t)$ and λ_n are assumed to be perfectly known.

The detector provides the indicator function $I(n_1, n_2)$ that asserts whether an event has been detected ($I = 1$) or not ($I = 0$) for the time-bin recorded at time

$$t_{n_1,n_2} = n_1 T + n_2 T_b = (n_1 N_b + n_2)\, T_b \tag{6.2}$$

with $N_b = T/T_b$ the number of bins per period. For simplicity we will consider that N_b is an integer number. Accordingly, $I(n_1, n_2)$ is known to follow a Bernouilli distribution described by the following two probabilities

$$P_0(n_2 T_b) = \Pr\left\{I\left(n_1, n_2\right) = 0\right\} = e^{-T_b \lambda(n_2 T_b)} \tag{6.3}$$

$$P_1(n_2 T_b) = 1 - P_0(n_2 T_b) \tag{6.4}$$

which were derived in Sec. 4.5 from the Poisson distribution.

The pulsar averaged density of arrival over the whole pulsar period T (see Table 2.4) is computed as

$$\lambda_p = \frac{1}{T}\int_0^T \lambda_p(t)dt = \frac{1}{N_b}\sum_{n_2=0}^{N_b-1} \lambda_p\left(n_2 T_b\right) \tag{6.5}$$

and the signal-to-noise ratio (SNR) is defined in the following way for X-ray pulsars:

$$SNR = \frac{\lambda_p}{\lambda_n} \tag{6.6}$$

The simplified pulsar profile introduced in section 5.1.3. (Fig. 5.1) will be adopted in the sequel when evaluating $\lambda_p(t)$. In that case the pulsar duration T_p and the maximum value of $\lambda_p(t)$ are given by

$$T_p = \frac{5T_{10} - T_{50}}{4} \tag{6.7}$$

$$\lambda_{\max} = \frac{16\lambda_p T}{7T_{10} + 5T_{50}}, \tag{6.8}$$

respectively.

6.1.2 Maximum Likelihood TOA estimation

From the above signal model, the ML criterion consists in maximizing the log-likelihood function $\ln \mathrm{f}_I\,(I;\tau)$ with respect to the wanted TOA τ. After trivial manipulations, and assuming the temporal independence of $I(n_1, n_2)$, we have that

$$\ln p_I\,(I/\tau) = \sum_{n_1=0}^{N_I-1}\sum_{n_2=0}^{N_b-1} I(n_1,n_2)\ln P_1(n_2T_b-\tau) + (1-I(n_1,n_2))\ln P_0(n_2T_b-\tau) = \\ = N_I \sum_{n_2=0}^{N_b-1}\left(\widehat{P}_0(n_2)\ln P_0(n_2T_b-\tau) + \widehat{P}_1(n_2)\ln P_1(n_2T_b-\tau)\right), \tag{6.9}$$

where N_I is the number of processed pulsar periods and,

$$\widehat{P}_1(n_2) = \frac{1}{N_I}\sum_{n_1=0}^{N_I-1} I(n_1,n_2) \tag{6.10}$$

$$\widehat{P}_0(n_2) = 1-\hat{P}_1(n_2) \tag{6.11}$$

are the ergodic estimates of $P_1(n_2T_b-\tau)$ and $P_0(n_2T_b-\tau)$, respectively. Since $I(n_1,n_2)$ are independent Bernouilli random variables, $\widehat{P}_1(n_2)$ is distributed following a binomial distribution of mean P_1 and variance P_1P_0/N_I, respectively. The central limit theorem states that $\widehat{P}_1(n_2)$ would become Gaussian if $N_IP_1 >> 1$. Thus, a long sample is required to have Gaussian statistics in case of a low density of arrival ($T_b\lambda(t) << 1$). Therefore, the Gaussian assumption is precluded in most situations and the true statistics of $\widehat{P}_1(n_2)$ must be dealt with. Elaborating further, we obtain that

$$\ln p_I\,(I/\tau) = N_I\sum_{n_2=0}^{N_b-1}\left(-\hat{P}_0(n_2)T_b\lambda(n_2T_b-\tau) + \hat{P}_1(n_2)\ln\left(1-e^{-T_b\lambda(n_2T_b-\tau)}\right)\right) = \\ = N_I\sum_{n_2=0}^{N_b-1}\left(-(1-\hat{P}_1(n_2))T_b\lambda(n_2T_b-\tau) + \hat{P}_1(n_2)\ln\left(1-e^{-T_b\lambda(n_2T_b-\tau)}\right)\right) = \\ = C_1 + N_I\sum_{n_2=0}^{N_b-1}\hat{P}_1(n_2)P(n_2T_b-\tau) \tag{6.12}$$

where $C_1 = -N_IT_b\sum_{n_2=0}^{N_b-1}\lambda(n_2T_b-\tau)$ is independent of τ provided that the bandwidth of $\lambda_p(t)$ is less than $0.5/T_b$ and, $P(t)$ is defined as

$$P(t) = T_b\lambda(t) + \ln\left(1-e^{-T_b\lambda(t)}\right) = \ln\left(e^{T_b\lambda(t)}-1\right) \tag{6.13}$$

Low-SNR approximation

In this section the ML estimator derived previously is particularized for the studied low-SNR scenario in which λ_n is usually several orders of magnitude greater than λ_p. Thus, we can expand $P(t)$ into a Taylor series at $\lambda_p(t)/\lambda_n = 0$, obtaining that

$$P(t) = C_2 + \frac{T_b}{1-\exp\left(-T_b\lambda_n\right)}\lambda_p(t) \tag{6.14}$$

with $C_2 = \ln\left(e^{T_b\lambda_n}-1\right)$ an irrelevant term. Plugging this approximation into $\ln p_I\,(I/\tau)$, the ML estimator is found to be the maximizer of

$$\ln p_I\,(I/\tau) = C_3 + \frac{N_IT_b}{1-\exp\left(-T_b\lambda_n\right)}\sum_{n_2=0}^{N_b-1}\hat{P}_1(n_2)\lambda_p(n_2T_b-\tau) \tag{6.15}$$

that can be seen as the output of a filter matched to the pulsar density of arrival $\lambda_p(t)$. Thus, the ML estimator is the one maximizing the following cost function:

$$\Lambda(\tau) = \sum_{n_2=0}^{N_b-1} \hat{P}_1(n_2)\lambda_p(n_2T_b - \tau) \tag{6.16}$$

Based on the sampling theorem, it is sufficient to compute N_s samples of $\Lambda(\tau)$ and interpolate to recover $\Lambda(\tau)$. Simulations revealed that $N_s = 8$ samples per period are enough for the studied SNR range whereas $N_s < 8$ yields yields some losses at high SNRs. The sampling cost function will be denoted $\Lambda(n)$ in the following.

Square Timing Estimation

Having in mind that $\lambda_p(t)$ is cyclic, we obtain that $\Lambda(\tau)$ is also periodic and therefore it can be expanded into a Fourier series

$$\Lambda(\tau) = \sum_{k=-\infty}^{\infty} c_k \exp\left(j2\pi\frac{k}{T}\tau\right) \tag{6.17}$$

with the k-th coefficient given by

$$c_k = \int_0^T \Lambda(\tau)\exp\left(-j2\pi\frac{k}{T}\tau\right)d\tau = \sum_{n=0}^{N_s-1}\Lambda(n)\exp\left(-j2\pi\frac{k}{N_s}n\right) \tag{6.18}$$

Following the same reasoning than in Sec. 5.1.6 for the radio pulsars, an approximated closed-form ML estimator can be derived considering uniquely the first harmonic ($k = 1$) of the Fourier series:

$$\Lambda(\tau) \simeq c_0 + 2\,\mathrm{Re}\{c_1\exp(j2\pi\tau/T)\} \tag{6.19}$$

In that case, the ML estimator is approximately given by

$$\widehat{\tau} = -\frac{T}{2\pi}\arg\{c_1\} = -\frac{T}{2\pi}\arg\left\{\sum_{n=0}^{N_s-1}\Lambda(n)\exp\left(-j2\pi\frac{n}{N_s}\right)\right\} \tag{6.20}$$

6.1.3 Crámer-Rao Bound

The ML estimator will yield unbiased estimates if the maximum of $\ln p_I(I/\tau)$ yields the true TOA on the average, that is[1]:

$$\begin{aligned} E\left\{\frac{d}{d\tau}\ln p_I(I/\tau)\right\} &= -N_I\sum_{n_2=0}^{N_b-1}E\left\{\widehat{P}_1(n_2)\right\}P'(n_2T_b-\tau) = \\ &= -N_I\sum_{n_2=0}^{N_b-1}P_1(n_2T_b-\tau)P'(n_2T_b-\tau) = -N_IT_b\sum_{n_2=0}^{N_b-1}\lambda_p'(n_2T_b-\tau) = 0 \end{aligned} \tag{6.21}$$

using that

$$\begin{aligned} P'(t) = \frac{d}{dt}P(t) = \frac{d}{dt}\ln\left(e^{T_b\lambda(t)}-1\right) &= \frac{T_b\lambda_p'(t)e^{T_b\lambda(t)}}{e^{T_b\lambda(t)}-1} = \\ = \frac{T_b\lambda_p'(t)}{1-e^{-T_b\lambda(t)}} &= \frac{T_b\lambda_p'(t)}{P_1(t)} \end{aligned} \tag{6.22}$$

Under the above regularity condition, the Crámer-Rao bound for the TOA estimation problem is given by the inverse of

[1] Notice that this condition is exactly the same that we imposed to consider that C_1 was independent of τ.

$$CRB^{-1}(\tau) = E\left\{\left(\frac{d}{d\tau}\ln p_I(I/\tau)\right)^2\right\} = N_I^2\sum_{n_2=0}^{N_b-1} E\left(\widehat{P}_1(n_2) - P_1(n_2T_b-\tau)\right)^2 P'^2(n_2T_b-\tau) =$$

$$= N_I\sum_{n_2=0}^{N_b-1} P_0(n_2T_b-\tau)P_1(n_2T_b-\tau)P'^2(n_2T_b-\tau) =$$

$$= N_IT_b^2\sum_{n_2=0}^{N_b-1}\frac{P_0(n_2T_b-\tau)}{P_1(n_2T_b-\tau)}\lambda_p'^2(n_2T_b-\tau) = N_IT_b^2\sum_{n_2=0}^{N_b-1}\frac{\lambda_p'^2(n_2T_b)}{e^{T_b\lambda(n_2T_b)}-1} \tag{6.23}$$

having in mind again that $\widehat{P}_1(n_2)$ follows a binomial distribution of variance P_0P_1/N_I. Notice that in the last equality we have taken into account that the result is independent of the actual value of τ because the function inside the summation is periodic. The CRB can be particularized to the studied low SNR scenario obtaining that

$$CRB_{low}^{-1}(\tau) = \frac{N_IT_b^2}{e^{T_b\lambda_n}-1}\sum_{n_2=0}^{N_b-1}\lambda_p'^2(n_2T_b) \simeq \frac{N_IT_b}{e^{T_b\lambda_n}-1}\int_0^T\lambda_p'^2(t)dt \leq N_I\lambda_n^{-1}\int_0^T\lambda_p'^2(t)dt \tag{6.24}$$

where the last upper bound correspond to $T_b \to 0$ taking into account that $x/(e^x-1)$ is strictly decreasing for $x>0$. Therefore, the detector should guarantee that $T_b << \lambda_n^{-1}$ in order to provide optimal estimates at low SNRs. Otherwise, the background noise saturates the detector output and the performance is degraded dramatically. The above integral can be evaluated for the simplified pulsar profile considered in Sec. 5.1.3 (Fig. 5.1) obtaining the following upper bound

$$CRB_{low}(\tau) \geq \frac{\xi}{N_ISNR} \tag{6.25}$$

with

$$\xi = \frac{5T_{50}(7T_{10}+5T_{50})(T_{10}-T_{50})}{16\lambda_{\max}T(5T_{10}-T_{50})} \tag{6.26}$$

the pulsar-dependent performance figure.

On the other hand, the CRB suffers a significant floor at high SNRs when $T_b\lambda_p << 1$. Unfortunately, this is the actual situation when we deal with X-Ray pulsars because $\lambda_pT << 1$ (see Tables 2.3-2.4.). It is for this reason that the sufficient statistic $\widehat{P}_1(n_1)$ remains noisy even when $\lambda_n \to 0$ since

$$E^2\{\widehat{P}_1\}/var\left(\widehat{P}_1\right) = N_IP_1/P_0 \propto N_I\left(e^{T_b\lambda_p}-1\right) << 1. \tag{6.27}$$

and therefore the sample size N_I must be increased to overcome this limitation.

The asymptotic CRB for high-SNRs has not been derived yet but the following approximate bound predicts correctly the referred high-SNR floor and converges to $CRB_{low}(\tau)$ at low SNRs:

$$\widetilde{CRB}(\tau) = \frac{\xi\left(1+SNR^{-1}\right)}{N_I} \tag{6.28}$$

Finally, the quality factor for the X-ray pulsar (Sec. 2.2) can be computed using the following expression:

$$Q = \frac{\sigma_x}{c\sqrt{CRB}} \tag{6.29}$$

with the CRB evaluated considering $L = N_IN_b = 10^9$ and $\sigma_x = 10^6$ the target standard deviation for the positioning error.

6.1.4 Simulations

In this section some simulations are provided with the aim of assessing the feasibility of using X-ray pulsars in spacecraft navigation applications. The figure of merit is the spatial standard deviation, i.e., $\sigma_x = c\sqrt{var\,\{\widehat{\tau}\}}$. X-Ray millisecond pulsars are considered with $T = 5 \times 10^{-3}$ and $\lambda_p = 0.025$ corresponding to the J0437-47 pulsar (Table 2.4). The detector resolution is $T_b = 10^{-4}$ and the field of view is set to 2 degrees from the ROSAT specifications. Regarding again the pulsars database in Table 2.4, the received $SNR = \lambda_p/\lambda_n$ varies from -40dB to -10dB. The observation time is set to $N_I = 10^7$, 2×10^7, or 10^8 periods yielding an observation time equal to $T_0 \simeq 14$, 28, or 140 hours, respectively. This observation time is coherent with the one predicted in Sec. 2.5.3 by means of the formula $T_0 > 25\lambda_n/\lambda_p^2$.

Notice that long observation times are required to work above the SNR threshold for those SNRs of interest (Fig. 6.1). Otherwise, the ML estimator variance departs from the CRB and, eventually, the estimator performance collapses at low SNRs due to the periodicity of $\lambda_p(t)$. Taking into account that $E\left(\widehat{\tau} - \tau\right)^2 \leq T^2/12$, the estimator spatial accuracy is upper-bounded by $\sigma_x \leq 4.33 \times 10^5$ meters in the case of the studied millisecond pulsars (see Figs. 6.1 and 6.2). Finally, we observe in figure 6.1 that the SNR threshold occurs *approximately* at SNR=-20dB ($N_I = 10^8$) and SNR=-10dB ($N_I = 10^7$). A longer sample would be required to work below this point (-20dB). Indeed, the threshold is known to be inversely proportional to the observation time and, thus, $N_I \simeq 10^{10}$ pulses should be averaged to yield efficient TOA estimates for any SNR greater than -40dB. Anyway, it is worth noting that the position of the studied X-ray pulsars (J0030, J2124, J0437) can be estimated without *noticeable* bias although the SNR is *slightly* below the referred thresholds.

Regarding the performance of the proposed ML-based estimators, we observe in figure 6.1 that both the optimal low-SNR ML estimator and its approximation (square timing) attain the CRB for moderate SNRs whereas the low-SNR approximation yields minor losses at high SNRs. However, the square timing is found to be slightly outperformed at high SNRs by the exact ML solution. On the other hand, the approximated CRB deduced in equation (6.28), which is not plotted for the sake of clarity, is found to predict the ML estimator performance for any SNR.

In figure 6.2 the performance of the triangular pulsar profile simulated in Fig. 6.1 is compared with the one provided by a narrower pulsar profile. As it is shown in Fig. 6.2, the temporal resolution is improved by increasing the signal bandwidth. Nonetheless, the detector finite resolution limits the observed bandwidth to $1/T_b$. On the other hand, figure 6.2 shows that the square timing estimator is degraded for the medium SNR range due to an insufficient oversampling ($N_s = 10$) of the log-likelihood function when the pulsar profile is narrower.

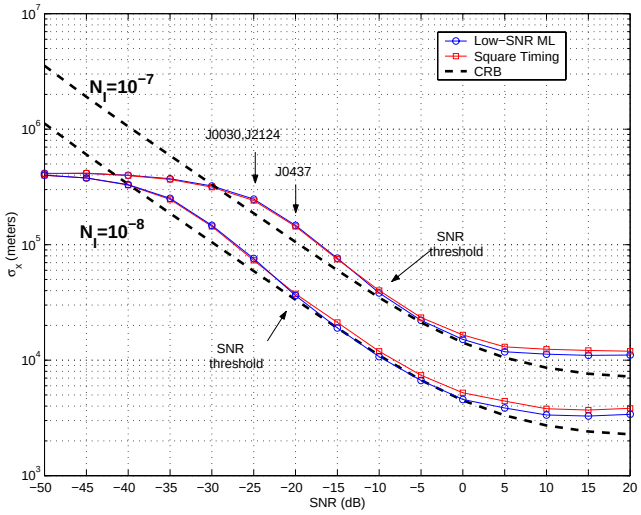

Figure 6.1: Positioning error standard deviation for the studied X-ray pulsars. The integration time is set to $N_I = 10^7,\ 10^8$ and the pulsar profile is triangular, i.e., T_{50}=2.5ms and T_{10}=4.5ms. Plots are obtained running 1000 independent realizations. The actual SNR for the X-ray pulsars listed in Table 2.4 as well as the approximated low-SNR threshold are indicated in the figure assuming that the detector field of view is equal to 2 degrees. The square timing estimates are computed from $N_s = 10$ samples of the log-likelihood function.

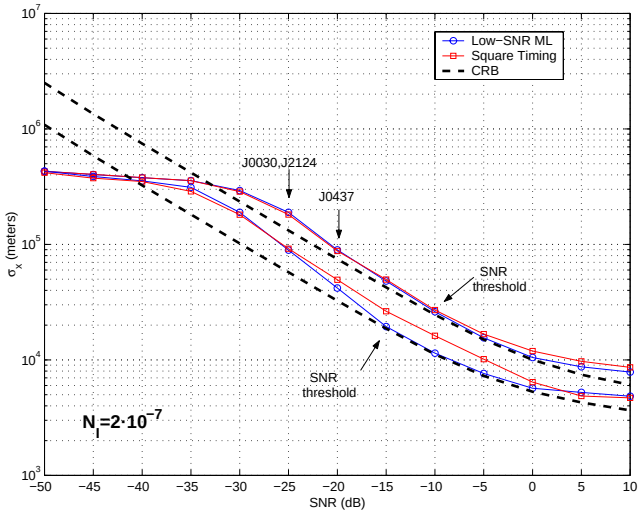

Figure 6.2: Positioning error standard deviation for the studied X-ray pulsars. The integration time is set to $N_I = 2 \times 10^7$ and two pulsars profiles are compared; the triangular pulsar profile in Fig. 6.1 (upper curves) and a narrower pulsar profile with T_{50}=1ms and T_{10}=3ms (lower curves). Plots are obtained running 500 independent realizations. The actual SNR for the X-ray pulsars listed in Table 2.4 as well as the approximated low-SNR threshold are indicated in the figure assuming that the detector field of view is equal to 2 degrees. The square timing estimates are computed from $N_s = 10$ samples of the log-likelihood function.

Chapter 7

Feasibility Results

Results in the geometry chapter were provided in terms of pulsar combinations, assuming a Gaussian profile for each pulsar. In this section we analyze the equivalent position accuracy provided by each single pulsar, σ_x, as $\sigma_x = c\sigma_\tau$, with c the speed of light and σ_τ the timing accuracy. Two models have been proposed to model the pulsar profile from experimental data: the double triangular model and the Gaussian model. Timing accuracy is closely dependent on the pulse shape. Hence, comparing the predicted accuracy from these two models helps to show the sensitivity of timing accuracy on this feature. The required position accuracy is 10^6 m. When translated to equivalent travel time, the required timing accuracy becomes $10^6/c = 3.33$ ms. Except for millisecond pulsars, it is found that this value falls below practically all pulse durations listed in the radio-pulsar database, and below all X-ray pulsars.

7.1 Quality factor analysis

Fast evaluation of feasibility for the wanted positioning accuracy can be obtained from the quality factor plots, $Q(f)$. Results provided for $Q(f)$ in the pulsar database chapter correspond to the double triangular model for the pulse shape. As we proceed to show, this model predicts better timing accuracies than those obtained from the Gaussian pulse model. Thus, both models provide a rough estimate of the range of values that may be expected due to different pulse shapes.

According to the definition of the Quality factor, $Q(f)\big|_{\mathrm{dB}} \geq 0$ dB guarantees (if in the operating region of the CRLB) an equivalent timing error to comply with the positioning accuracy $\sigma_x = 10^6$ m. for $L = 10^9$ samples, which for a bandwidth of 200 Mhz is equivalent to 5 seconds of integration time. If we take the millisecond pulsar B1937+21, which has the highest quality factor at 1 GHz, the quality factor is $Q(1\mathrm{GHz}) = 11.8$ dB for an effective antenna area $A_e = 10\mathrm{m}^2$. Hence, the equivalent positioning accuracy is,

$$\sigma_x \quad = \quad \frac{10^6}{Q} = 10^6 \cdot 10^{-1.18} = 66069 \quad \mathrm{m}. \tag{7.1}$$

We should check now that the integration time of 5 s. is above the threshold for the ML estimation algorithm and that the CRLB applies. The threshold condition (for $\Gamma_L = 15$ dB and $K = 2$ (complex data) is,

$$L \geq \frac{1}{\mathrm{SNR}^2_{1\mathrm{GHz}}}(K-1)\Gamma_{\mathrm{th}}\xi_p$$

which yields a minimum $L = 4.36 \cdot 10^{11}$ samples, clearly the threshold condition is not fulfiled for 10^9 samples, although B1937+21 is asymptotically for large L the best pulsar. For 5 s. of integration, the timing error predicted by the CRLB is still much larger than the pulse duration of B1937+21. The determining factor for the threshold condition is SNR: table (7.1) depicts the minimum integration time required for several pulsars and the equivalent positioning accuracy obtained from the extrapolation equation (7.2). The positioning accuracy obtained from B1937+21 after sufficient integration to reach the operating region of the CRLB is related to the very narrow pulse of this pulsar.

Pulsar	SNR (dB)	Q (dB)	T_o (min.)	σ_x (m.)	T_{50} (ms.)
B1937+21	−55.6	11.8	36.36	3162	0.1
B0736−40	−50.2	−7.5	3.07	926467	29
B1451−68	−50.0	−3.8	2.34	452529	12.5
B0950+08	−48.9	−0.7	1.04	316174	9.5
B0329+54	−45.2	4.5	0.12	290556	6.6

Table 7.1: Minimum Integration times and the corresponding equivalent positioning accuracy for some of the best SNR pulsars, considering the double triangular model for the pulsar profile. Results have been obtained using a (conservative) value $\Gamma_L = 15$ dB and an effective antenna area $A_e = 10$ square m. A more elaborate equation for the threshold incorporating information on the pulse shape might reduce this value, obtained from simulations using a rectangular profile. The accuracy at the threshold T_o is related to the effective duration of the pulse. The last column lists T_{50}, the duration at 50% peak intensity, for comparison. Note that for the last pulsar a low integration time below 100 pulsar periods is predicted: this is to be corrected as SNR conditions are too good in this case for the low-SNR theory we have developed to apply. The necessary correction will be applied in the following table, which assumes a Gaussian model for the average pulsar power profile.

Pulsar	SNR (dB)	Q (dB)	T_o (min.)	σ_x (m.)	T_{50} (ms.)
B1937+21	−55.6	8.90	40.13	5860	0.1
B0736−40	−50.2	−10.72	4.02	1699492	29
B1451−68	−50.0	−5.80	2.25	732540	12.5
B0950+08	−48.9	−3.00	1.07	556730	9.5
B0329+54	−45.2	5.32	1.19	77681	6.6

Table 7.2: Minimum Integration times and the corresponding equivalent positioning accuracy for the same pulsars as in table (7.1), under identical conditions but using the Gaussian pulse shape model. Note that worse results are obtained for the position accuracy, as the double triangular model is optimistic. A minimum of 100 pulsar periods has been considered now in all cases for the integration time. For pulsar B0329+54, the double triangular shape predicts better behaviour (better asymptotic quality factor) than the Gaussian shape: this is due to the much wider 10% to 50% peak intensity duration ratio T_{10}/T_{50} of this particular pulsar over other pulsars. The quality factors listed in this figure have been evaluated for the same antenna area over all pulsars. Therefore, the relationship between different quality factors is maintained for a different (smaller) antenna area.

Pulsar	SNR (dB)	Q (dB)	T_o (min.)	σ_x (m.)	T_{50} (ms.)
B1937+21	−60.6	8.90	401.30	5860	0.1
B0736−40	−55.2	−10.72	40.22	1699492	29
B1451−68	−55.0	−5.80	22.50	732540	12.5
B0950+08	−53.9	−3.00	10.72	556730	9.5
B0329+54	−50.2	5.32	1.19	245651	6.6

Table 7.3: Minimum Integration times and the corresponding equivalent positioning accuracy for the same pulsars as in table (7.2), using the Gaussian pulse shape model but with an antenna area of 5 square meters (3 dB loss in SNR) plus an additional degradation loss of 2 dB (mis-pointing and other effects). Note that now the positioning accuracies are the same as listed in table (7.2), but at the cost of a much longer integration time. For the last pulsar the minimum observation time of 100 periods is still enforced. Now, over 6 hours of integration are required to synchronize to the millisecond pulsar B1937+21.

7.1.1 Extrapolation to other T_oB and A_e

The equivalent positioning accuracy is derived from the equality,

$$Q = \frac{\sigma_x}{c \cdot \sigma_{\tau,L}} = \frac{\sigma_x}{c} 2\pi\sqrt{L}\frac{\sigma_p^2}{\sigma_n^2}\gamma_p \tag{7.2}$$

Therefore, using different values for the effective area, integration times or bandwidth, we should have (above the threshold) that,

$$\sigma_x(T_oB, A_e) = \frac{10^6}{Q}\sqrt{\frac{10^9}{T_oB}} \cdot \frac{10}{A_e} \tag{7.3}$$

for A_e in square meters. This will be valid when the "above- threshold" condition is met,

$$L\left(\frac{\sigma_{p,T}^2}{\sigma_n^2}\right)^2 = \mathrm{SNR}_{1\mathrm{GHz}}^2 \cdot \left(\frac{A_e}{10}\right)^2 \cdot T_oB \geq (K-1)\Gamma_{\mathrm{th}}\xi_p$$

in terms of the average SNR, $\frac{\sigma_{p,T}^2}{\sigma_n^2}$, and $L = T_oB$ with $B = 200$ MHz and T_o the observation time. As the SNR is evaluated for $A_e = 10$ square m., extrapolation from the average SNR at 1 GHz, $\mathrm{SNR}_{1\mathrm{GHz}}$, appearing in the corresponding pulsar tables and figures yields the previous equation, with $K = 2$ (complex data) and $\Gamma_{\mathrm{th}} = 15$ dB (for the double triangular pulse). For the Gaussian pulse, the calibrated equation (5.1.5) has been used to establish the threshold condition.

7.2 Long term stability

Millisecond pulsars are required due to their low timing noise to derive a stable timebase. Pulsars which much higher periods should have their timing models corrected in the long run by millisecond pulsars, as high order derivatives of the timing models are noisier than for millisecond pulsars. Continuous monitoring is thus required, as well as extraction of a sufficiently high number of pulsars. Other millisecond pulsars apart from B1937+21 should be recovered for greater long term stability of the time base. Unfortunately, other millisecond pulsars have very low SNR and much longer integration times are required to beat the threshold effect. It is expected that for longer integration times, the constant speed model we have assumed does not suffice and higher derivatives of the position are required. As pulsars with longer periods usually have better SNR, they can be used to estimate these position derivatives an aid in the extraction of millisecond pulsars from the noise, although the SNR of the remaining millisecond pulsars appears to be extremely low.

Chapter 8

Technological Aspects

This chapter addresses the technological impact of the required navigation system on instrumentation. For radio-pulsars, it has been determined that large antenna effective areas are necessary to avoid extremely long integration. Nevertheless, a technological analysis is included in terms of a reference system.

8.1 Reflector Antennas

Geometrical Dilution of Precision (GDOP) requires that reference sources for positioning be widely distributed in arrival angles. Hence, the use of a single reflector antenna requires mechanical steering and that only a single pulsar or cluster of closely-spaced pulsars can be processed within each observation window. Due to small angular differences within each pulsar cluster, the antenna can only focus on one single pulsar, while others are recovered with some mis-pointing loss. A similar problem appears for the case of electronically steerable micro-strip antennas and is discussed in more detail in the following section. The advantage of reflector antennas over multibeam antenna arrays is found in the complexity of the reception chain: only one is necessary. Nevertheless, spatial processing capabilities are more limited.

8.2 Electronically Steerable Micro-Strip Antennas

Array antennas are the most suitable architecture to provide multibeam capability and adaptive beamforming. The following three issues are considered, taking the MIRAS-SMOS mission of ESA as an example :

- expected performance for the RF subsystems.
- potential technologies and geometries for the antenna system.
- technological implications of the antenna system.

8.2.1 A reference system, MIRAS-SMOS

The MIRAS-SMOS is a radiometer for earth observation operating at 1.4 GHz. The radiometer has 69 independent receivers in a Y shaped geometry, and by properly processing the signal received by each of the 69 independent receivers a radiometric image of the observed scene can be produced.

The MIRAS-SMOS receivers have a noise temperature of the order of 230 K, but they are not cooled, and their application requires the insertion of an isolator between the antenna and the receiver that introduces additional losses. The proposed Spacecraft Navigation System probably would not require the insertion of an isolator, and in the case that the receivers are cooled the assumption of noise temperature of 30 K seems reasonable.

For the Spacecraft Navigation System it is necessary to synthesize beams pointing at different directions and to place nulls on the radiation pattern to cancel noise sources such as the sun. This requires

Table 8.1: Cluster coordinates

Cluster	Ecliptic latitude	Ecliptic Longitude
1	15,45	300,240
2	−30,0	270,240
3	−60,−30	240,180
4	−60,−30	180,150
5	−15,15	180,120
6	30,60	90,60

Table 8.2: Pointing losses

Cluster	Pointing lat.	Pointing long.	Lat. scan	Long. scan	Loss (dB)
1	30	270	± 15	± 30	2
2	-15	255	± 15	± 15	0.5
3	-45	210	± 15	± 30	2
4	-45	165	± 15	± 15	0.5
5	0	150	± 15	± 30	2
6	45	75	± 15	± 15	0.5

an antenna geometry based on single non-directive antennas, each one with its own receiver, and pattern synthesis done by processing the received signal. Once again the MIRAS-SMOS antenna gives us some real data on the performance of this type of antennas. The MIRAS-SMOS antennas are dual polarized, circular microstrip patch antennas on a circular cavity. The radiation pattern can be approximated by $t(\theta) = \cos^3\theta$, and the elements only radiate in one half-space. This is an important consideration, because the proposed Spacecraft Navigation System requires the reception of signals coming, in principle, from any direction. It must be stressed, that although beam synthesis can be performed by processing the received signals, there is a loss due to the radiation pattern of the elements. If we consider the $\cos^3\theta$ pattern, it means that for a scan angle of 30 deg there is a loss of 1.9 dB and for a scan angle of 60 deg there is a loss of 9 dB relative to the effective area defined for the broadside direction. Therefore having a single large aperture with the requirement of very large scan angles is probably not the best choice. In fact, with a single antenna it is impossible to steer the beam to all space directions. It must be remembered that the radiation pattern of a single antenna element is never isotropic.

8.2.2 Structure of the antenna array

An observation of figure 4 shows that the 50 best pulsars are not uniformly distributed, but they are clustered in certain directions (at least 6 clusters can be defined as appear in the tables). A possible strategy would be to use as antenna system 5 different arrays, pointing at the center of each of the clusters. Each array would have a limited beam shaping capability in order to scan its cluster and to place nulls in the direction of noise sources. An array of 3×3 elements gives enough degrees of freedom to achieve these goals. If we consider an array of 3×3 elements spaced 0.7λ, this results at 1 GHz in an effective area in the broadside direction of the order of 0.36m^2.

Tables (8.1) and (8.2) summarize for each antenna the pointing direction, the required scan angle and the losses due to the radiation pattern of the element due to beam scanning. It is observed that clusters 1 and 3 require larger angular scanning that results in larger losses. A potential option can be to split each into two clusters. In this case there would be 7 different clusters, each of them having maximum scan of the order of ±15 deg. With 7 clusters and considering a 3×3 antenna, there would be a need for 63 antenna elements and receivers. Considering that the MIRAS-SMOS has 69 elements, the payload specification concerning of mass, and power consumption of this mission can be a good referent for the

requirements of the proposed Spacecraft Navigation System.

For an antenna element, a relative bandwidth of the order of 20% is near the technological limit. In this sense, considering a bandwidth of 200 MHz centered at 1 GHz is a reasonable figure that will be difficult to exceed.

The component technology at the 1 GHz band is well established for space applications. transceiver equipment for deep space probes such as Voyager have been operational in this band for over 30 years.

References

P.Silvestrin, M.Berger, Y.H.Kerr, J.Font, "ESA's Second Earth Explorer Opportunity Mission: The Soil Moisture and Ocean Salinity Mission - SMOS", IEEE Geoscience and Remote Sensing Society Newsletter, March 2001, pp. 11-14.

Chapter 9

Conclusions

As far as signal processing is concerned, the possibility of obtaining position accuracies below 10^6 meters has been validated. The required geometrical framework and the associated position and timing estimation algorithms have been presented in the previous chapters. The derived theoretical results apply in the low-SNR (small antenna) regime, where additive Gaussian noise affecting pulsar reception is the dominant degradation factor. This region of operation is understood as that requiring the integration of many pulse periods before reliable timing estimates well below the pulse duration can be obtained.

Nevertheless, the true limitation of a pulsar-based location system has been found to be the required instrumentation. Very few radio pulsars have a sufficiently high signal-to-noise ratio so that a small antenna can provide reasonable integration times (few minutes) under the best possible conditions, although they suffice to provide position estimates. Our results have been obtained for a 10 square meter antenna (brief summary in tables (7.1) to (7.3), and more complete results in the Geometry chapter), assuming perfect cancellation of radio-frequency noise from the Sun and/or nearby planets, a constant speed model during the integration time, perfect antenna pointing (attitude control) and simultaneous observation of the processed pulsars. The technological effort does not only apply to the antenna but also to the signal bandwidth. It has been shown that increasing the bandwidth of the receiver allows to obtain better positioning accuracies. Hence, results have considered the optimistic technological limit of 200 MHz bandwidth at a central frequency of 1 GHz. Thus, front-end digital signal processing is also performing at high speed, with power consumption being also a critical factor.

A relaxation of the technological constraints considered in this study (smaller antennas, sequential rather than simultaneous observation of different pulsars, smaller receiver bandwidths, consideration of implementation loss and safety margins) is possible at the expense of much longer integration times, as resulting from very faint pulsar signals. A reduction in the antenna area by a factor r must be compensated for with an increase in the integration time-bandwidth product of $1/r^2$. It is believed that for reduced-size antennas, the constant speed model may fail due to the necessity of estimating higher order derivatives of position (as integration times are longer). In all likelihood, an integration time of many hours would be required to extract the faintest millisecond pulsars from noise, maybe imposing limitations on the smoothness of the trajectory (number of significative position derivatives). In particular, the highest technological impact is the issue between simultaneous or sequential observation of pulsars. The former requires as many antennas as observed pulsars but provides the fastest evolution of positioning accuracy versus time. The latter would further increase latency, the minimum time before a position estimate is produced (probably by a factor equal to the minimum number of required pulsars), as well as the ambiguity resolution algorithm. The smoothness of the spacecraft trajectory is believed to be more critical in the case of sequential observation.

The study of X-ray pulsars predicts longer integration times as arrival rates in the order of only 90 photons per hour have been reported for the usable X-ray pulsars, thus yielding over one day of integration (taking the ROSAT detector as a baseline). The number of available X-ray pulsars has been found to be much lower than for radio pulsars.

Summary: the authors of this study believe that the complexity involved for autonomous positioning at the spacecraft is rather involved. Although pulsar positioning has been shown to be theoretically possible, issues of complexity and latency in obtaining position estimates cannot be met for *small* spacecraft capable of *fast* autonomous positioning. Rather, such a positioning system appears more suitable for large spacecraft or for hub stations providing telecommunication and location services to smaller spacecraft.

Some additional comments on pulsar-based positioning are provided:

- Hardware calibration is necessary, specially electronic delays of the receiver which contribute a bias to the timing estimates. Note that the location algorithms we have devised operate on the assumption of unbiased timing estimates.
- Kalman based approaches (optimum post-filtering schemes) can provided effective integration times of many days to increase positioning accuracy.
- For long term stability, the recovery of millisecond pulsars is crutial due to their low level of timing noise. Apart from B1937+21, millisecond pulsars have very low SNR and long integration times are required to extract timing information. Theoretically, stronger pulsars could be used to estimate a sufficient number of position derivatives to guarantee synchronous averaging of millisecond pulsars over longer periods of time. Nevertheless, the involved SNR are so low that unforeseen irregularities might hinder their reception.
- As concerns interference from SSO, navigation would be seriously hampered in the inner solar system or in the vicinity of Jupiter. The impact of these interfering sources can be diminished at the cost of increased system complexity (adaptive antenna arrays for interference cancellation). Such a navigation system is intended for *cold* regions in space.
- the definition of a universal pulsar time standard seems unavoidable for deep space navigation over long periods of time. This would also be advantageous for Earth-based systems requiring long term stability.
- speed estimation does not require ambiguity resolution. Hence, as long as this assumption is approximately correct, the integration window for speed estimation can be much longer than for phase estimation. Otherwise, speed CRLBs should also be checked to be above the corresponding estimation threshold. The constant speed assumption fails in the vicinity of planets due to acceleration and higher order derivatives.
- this study has considered that all pulsars are observed simultaneously. This allows for the computation of the best positioning accuracy per observation time, using any number of pulsars. If sequential observation is performed instead, the complexity of instrumentation is greatly reduced at the cost of slower evolution of the positioning accuracy. At the instrument level, this requires a mechanical pointing system. At the geometric level, the associated signal processing should be revisited. It is expected, though, that sequential observation may limit the maximum position derivatives of the spacecraft that the algorithms can successfully deal with.
- results for X-ray pulsars are constrained to the found solitary rotation-powered pulsars listed in the database. These are few and their reduced photon arrival rate leads to very long integration times taking the ROSAT detector as the baseline. More reasonable integration times would require larger detectors with better focusing capability.

Other aspects not considered in this study are:

- interstellar scintillation: pulsar signals are subject to slow frequency selective fading, which should be monitored for the derivation of timing and position estimates. Some pulsars may go below a detection threshold, becoming unavailable for positioning. This study has not considered SNR estimation. Statistics of interstellar scintillation could help establish probabilities of pulsar availability.

- adaptive de-dispersion: the dispersion coefficient is also slowly changing in time. Adaptive corrections could be used to refine de-dispersion.
- long-term corrections to the pulsar timing database: (a) procedures for compensating long-term timing noise of second pulsars via the more stable millisecond pulsars. This would require the definition of a universal pulsar time standard. (b) compilation of all physical effects determining the pulse arrival time model.
- relativistic corrections: this study has only considered aspects related with signal processing. The full definition of a pulsar navigation system is to be formulated in the geometrical framework of general relativity.